Fall 2020

Additive manufacturing of customized lithium-ion batteries: Process fundamentals and applications

Xiaowei Yu

Department: Mechanical and Aerospace Engineering

ADDITIVE MANUFACTURING OF CUSTOMIZED LITHIUM-ION BATTERIES: PROCESS FUNDAMENTALS AND APPLICATIONS

by

XIAOWEI YU

A DISSERTATION

Presented to the Graduate Faculty of the

MISSOURI UNIVERSITY OF SCIENCE AND TECHNOLOGY

In Partial Fulfillment of the Requirements for the Degree

DOCTOR OF PHILOSOPHY

in

MECHANICAL ENGINEERING

2020

Approved by:

Dr. Heng Pan, Advisor
Dr. Jonghyun Park
Dr. Frank Liou
Dr. K. Chandrashekhara
Dr. Chang-Soo Kim

PUBLICATION DISSERTATION OPTION

This dissertation consists of the following four articles, formatted in the style used by the Missouri University of Science and Technology:

Paper I, "Direct Aerosol Printing of Lithium-Ion Batteries", found on pages 10–26, has been published in International Symposium on Microelectronics.

Paper II, "Aerosol Jet Printing of Electrodes for Lithium-Ion Batteries", found on pages 27–39, has been accepted by ASME 2019 14th International Manufacturing Science and Engineering Conference (MSEC 2019), June 10-14, 2019, Erie, PA.

Paper III, "Customizable Nonplanar Printing of Lithium-Ion Batteries", found on pages 40–77, has been published in Advanced Materials Technologies.

Paper IV, "Solvent-Free Additive Manufacturing of Electrodes for Lithium-Ion Batteries with Tunable Porosity", found on pages 78–102, is intended for journal submission.

ABSTRACT

In the pasting decades, considerable efforts have been spent in developing the next-generation lithium-ion batteries (LIBs), from advanced active materials to new manufacturing methods. The development of additive manufacturing (AM) has brought new opportunities to LIBs. In this work, two AM methods are introduced for fabricating electrodes of LIBs. The first method is aerosol printing, which is a solvent-based wet additive method. Whereas the second method is a solvent-free, dry printing method. The commonly used materials for current collectors and active materials (including cathodes and anodes) of LIBs are aerosol printed and the electrochemical functionalities of the printed materials are found to be comparable to those by conventional slurry casting method. Thick electrodes by aerosol printing can deliver an areal capacity which is at least twice of those conventional slurry-casted electrodes. Furthermore, aerosol printing is utilized for the fabrication of customizable LIBs with arbitrary geometry on 3D structures due to its non-planar printing capability. The second AM method, solvent-free dry printing method eliminates the usage of organic solvents and significantly reduces the manufacturing costs. Another advantage of this method is the processability of thick electrodes with tunable porosity. The dry-printed electrodes exhibit much better high-rate performance than conventional slurry-casted electrodes. The dry-printed electrodes with varied porosity are also evaluated in terms of their high-rate performance. Granular models are developed to simulate the interfacial-energy-driven dry powder mixing process. The percolating behavior of the conductive additives during the calendaring process is also studied with the granular models.

ACKNOWLEDGMENTS

Firstly, I would like to sincerely thank my advisor, Dr. Heng Pan, for his conscientious support and guidance throughout my five years of Ph.D. study. His diligence, enthusiasm and rigorous attitude towards research are always encouraging me to be a researcher like him. I would also like to thank Dr. Xian Huang for recruiting me to Missouri S&T and developing my interests in the field of electronics manufacturing.

I would like to extend my gratitude to the professors on my committee, Dr. Jonghyun Park, Dr. Frank Liou, Dr. K. Chandrashekhara and Dr. Chang-Soo Kim for their incredible suggestions and guidance on my work.

I would also like to thank our collaborators, Dr. Yan Wang, Yangtao Liu and Dr. Ruihan Zhang at Worcester Polytechnic Institute, and Dr. Jonghyun Park, Susmita Sarkar and Hiep Pham at Missouri S&T. Without their professional and invaluable inputs, it would be impossible for me to complete my work.

I would like to acknowledge the research funding support from Honeywell Federal Manufacturing & Technologies with the U.S. Department of Energy, and the United States Advanced Battery Consortium LLC (USABC).

I really appreciate the help and support from my labmates, Dr. Brandon Ludwig, Dr. Wan Shou, Chinmoy Podder, I-Meng Chen, Xiangtao Gong, Joshua Staggs, Bikram Mahajan and Avinash Kankipati on my research and life.

Lastly, I would like to express my special thanks to my family, Haiping Yu, Rongdi Xu and Shuo Yang for their unconditional support and love.

TABLE OF CONTENTS

LIST OF ILLUSTRATIONS

SECTION Page

PAPER II

PAPER III

LIST OF TABLES

NOMENCLATURE

Symbol	Description
ϕ	Porosity of Electrode
L	Areal Loading of Electrode
T	Thickness of Electrode
σ	Electronic Conductivity of Electrode
R	Radius of Dry Powder Particle
E	Young's Modulus of Dry Powder Particle
ν	Poisson's Ratio of Dry Powder Particle
γ	Surface Energy of Dry Powder Particle
γ^d	Dispersive Surface Energy of Dry Powder Particle
γ^p	Polar Surface Energy of Dry Powder Particle
δ	Overlap between Two Dry Powder Particles
a	Radius of Contact Zone between Two Dry Powder Particles

1. INTRODUCTION

1.1. BACKGROUND AND RESEARCH OBJECTIVES

In the past decades, global communities have spent great efforts in exploiting renewable and sustainable energy resources. As a result, novel energy harvesting and storage devices with advanced materials and architectures have been continuously investigated [1-3]. Lithium-ion batteries (LIBs), one of the most popular energy storage devices, have shown great promise in sustainable energy strategy due to the long cycle life and high energy density compared to other secondary battery systems [4-6]. LIBs have attracted numerous applications such as portable electronic devices [7] and electric vehicles (EVs) [8].

In current LIBs industry, the electrodes are usually fabricated by conventional slurry casting method [9,10]. In this method, the solvent-based slurry is prepared by wet mixing of active materials, conductive additives, and binder additives in solvent. Then, the slurry is casted onto the current collector by doctor blade, slot-die coater, or roll-to-roll coating system. Figure 1.1 shows the schematic of slurry casting of electrode by a doctor blade. The slurry casting method has been widely applied to various type of electrodes for LIBs and is the major electrode manufacturing method in the current LIBs industry. Nevertheless, the conventional slurry casting method requires large amount usage of organic solvent (most commonly N-Methyl-2-pyrrolidone, NMP), which is expensive and non-ecofriendly [11]. In the industry-level manufacturing, a drying line and a solvent recovery system are needed which significantly increase the manufacturing cost [6]. Also, slurry casting method has limited processability in thick electrodes [12-14]

with high areal loading. Delamination (poor bonding between electrode and current collector) and surface cracking are common issues for slurry-casted thick electrodes. Such limitation in manufacturing method has posted challenge to meet the ever-increasing demands of high energy density of LIBs [15].

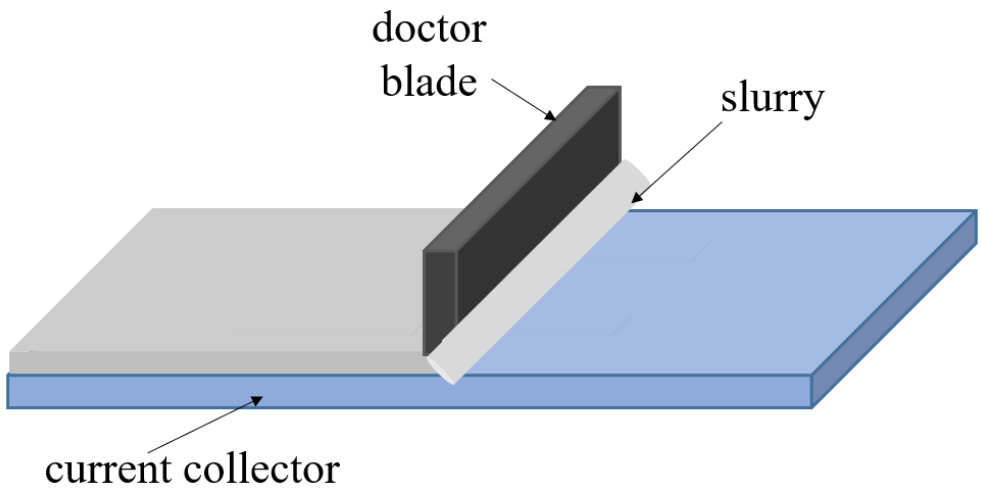

Figure 1.1. Schematic of slurry casting method.

The development of additive manufacturing (AM) has brought new opportunities in lowering manufacturing cost as well as facilitating new electrode designs of LIBs. The main objective of research presented in this dissertation is to investigate two AM methods for fabricating the electrodes of LIBs. The two AM methods are aerosol printing and solvent-free dry printing. The manufacturing process strongly affects the microstructure of electrodes, which further determines the distribution of binder materials, conductive additives, active materials and filled electrolyte. Binder materials help hold all the rest of materials in place, attaching to the current collector. A poor

bonding of the materials in the electrode might cause extra contact resistance, and a poor bonding between electrode and current collector would result in a high interfacial resistance. The distribution of conductive additives and electrolyte determines how electrons and ions are transported during the electrochemical reactions. The distribution of active materials directly influences how they participate in the electrochemical reactions. All the mentioned factors are synergistically affecting the electrochemical performance of the electrodes. In this work, the fabrication process of the electrodes for LIBs by the two AM methods are developed. After developing the fabrication process, those electrodes by the two AM methods are compared to the conventional slurry-casted electrodes in terms of structures and electrochemical performances. The performance of the electrodes by AM methods is found to be comparable to or better than that of conventional slurry-casted electrodes. Furthermore, the AM methods enabled novel electrode designs (which cannot be fabricated by the conventional slurry casting method) are exploited to further improve the specific performance and extend the application of LIBs. The objective of developing aerosol printing of electrodes for LIBs is to fabricate customizable LIBs with arbitrary geometry on both planar and 3D non-planar structures. The flexibility and non-planar printing capability in multi-scale have enabled electrodes in different geometry, thickness, and 3D architectures. One of the objectives of developing solvent-free dry printing of electrodes for LIBs is to reduce the manufacturing cost by eliminating the usage of solvent and reducing material waste by additively spraying into desired geometry. Another objective of developing this method is to optimize the high-rate performance by tuning the porosity of electrodes.

1.2. ADDITIVE MANUFACTURING OF CUSTOMIZED BATTERIES

For commercial LIBs, after slurry casting of electrodes, they need to be assembled with electrolyte and other inactive components for packaging. Commercial LIBs are usually packaged in fixed geometry such as cylinder, coin, and pouch with scrolled or layered planar sheets for each component [16]. Nevertheless, LIBs with customizable geometry are desired for specialized applications such as wearable electronics [7,17] and on-device power systems [18,19] for automobile and aerospace vehicles, For example, LIBs can be made into a watchband to power an electronic watch [20] which eliminates the installation and replacement of coin cell. To meet such demands, irregular, customizable LIBs in arbitrary geometry on 3D structures along with the packaging, integrating, and manufacturing approaches need to be developed. So far, the most effective solution to fabricate freeform LIBs is additive manufacturing (AM, popularly known as 3D printing) [21–24] The on-demand and layer-by-layer manufacturing method has provided the flexibility to accommodate customizable designs of 3D LIBs.

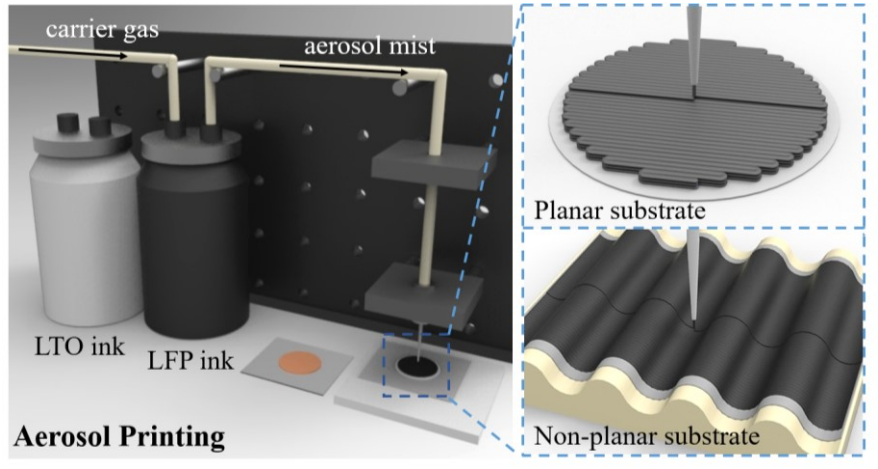

Figure 1.2. Schematic of aerosol printing.

In this work, aerosol printing is chosen for the purpose of freeform printing due to its unique advantages of non-planar printing capability in multi-scale. Aerosol printing is a recently developed AM technology that utilizes moderately pressurized air to nebulize the active materials into aerosol mist and drive the precise material deposition with smallest feature size down to 10 μm [25]. Schematic of aerosol printing can be found in Figure 1.2.

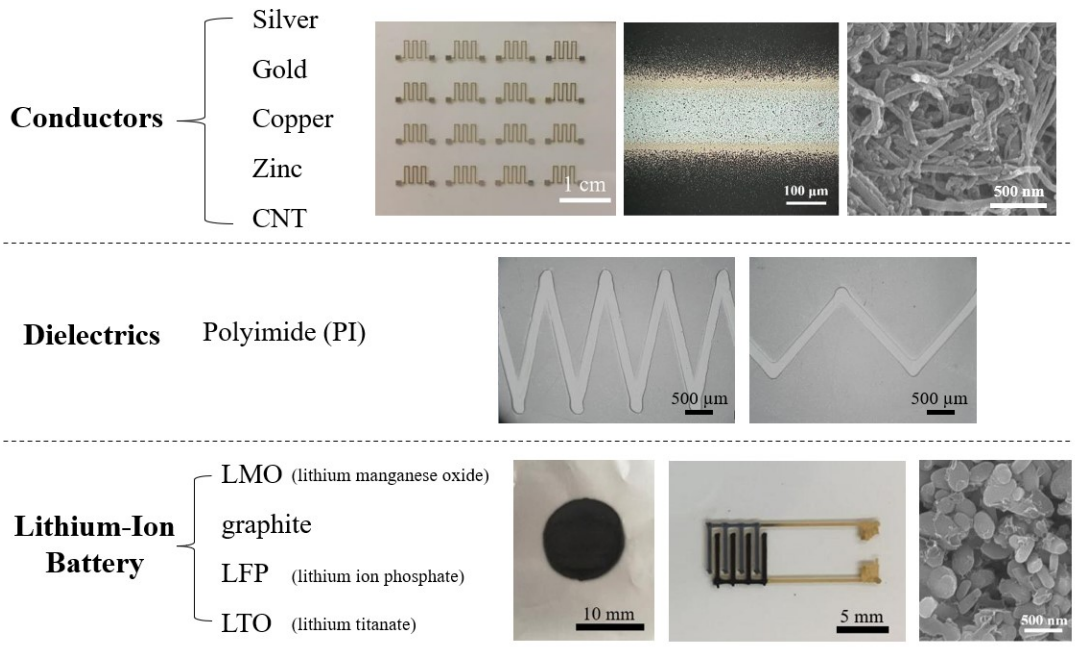

Figure 1.3. Summary of aerosol printable materials.

Aerosol printing processes a wide variety of materials, including polymers [26,27], metallic conductors [28–30], semiconductors [31,32], carbon-based nanomaterials [33,34] and energy materials [3] in laden inks with a wider range of viscosity from 1 cP to 1,000 cP [35,36]. Figure 1.3 summarizes the aerosol printable

materials developed in our lab. A unique advantage of aerosol printing for the purpose of freeform fabrication is the capability of deposition on non-planar substrates with complex surface topologies such as trenches and wavy structures (tens of micron to millimeter size) due to the flexible working distance of 1-5 mm from the deposition nozzle to the substrate [37,38]. The non-planar printing can be further extended to large objects (centimeter size) with 5-axis stage equipped. Such hierarchical non-planar capabilities potentially give rise to building LIBs on complex, multi-scale 3D architectures.

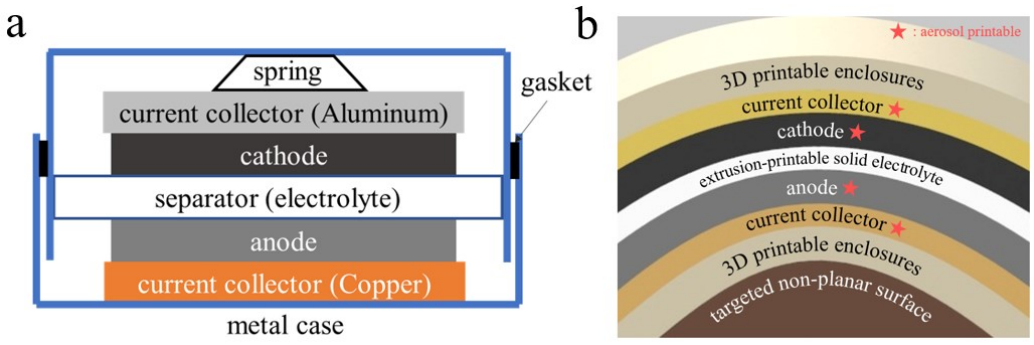

Figure 1.4. Components of LIBs in (a) a conventional coin cell and (b) customizable non-planar cell.

Figure 1.4 compares the components of a conventional coin cell to those of a customizable non-planar LIB. In these components, current collectors and active materials for cathodes and anodes are aerosol printable as investigated in the first two publications presented in this dissertation. The packaging enclosures are printable by various AM methods. In this work, we use fused deposition modeling to 3D print the electrochemically stable enclosures for packaging the aerosol printed 3D non-planar

electrodes. We are also developing the extrusion printing of solid electrolyte [39,40]. This work primarily demonstrates the feasibility of customizable non-planar LIBs and we foresee the great opportunities in the highly customizable energy storage systems brought by the ever-developing AM techniques.

1.3. SOLVENT-FREE ADDITIVE MANUFACTURING

As discussed in Section 1.1, currently, the slurry casting method is still playing a dominant role in LIB industry. In this method, NMP is often used as the organic solvent to disperse the active materials, conductive additives, and binder additives. However, due to the flammability and toxicity of NMP, an expensive solvent recovery system is necessary to reduce the environmental hazards, which significantly increases the manufacturing cost [41-43]. To address this issue, a water-based slurry system using water instead of NMP as solvent and replacing polyvinylidene fluoride (PVDF) with cellulose-based binders was brought up as an eco-friendly and less expensive option for electrode manufacturing [44-45]. However, the dispersing of materials becomes more difficult in the water-based system due to the strong hydrogen bonding [46]. For both organic solvent-based and water-based slurries, a high temperature drying process is always necessary to ensure the removal of solvents. The drying process requires additional time and energy which further increase the manufacturing cost.

Another alternative route towards low-cost manufacturing of electrodes for LIBs is to fully remove the solvents during the manufacturing process, so drying process with high energy input and the expensive solvent recovery equipment are no longer required. Here, a solvent-free additive manufacturing method by electrostatic spraying.

Manufacturing of dry electrodes starts from the mixing of dry powders of the active materials, conductive additives, and binder materials. After mixing, the particles of conductive additives and binder additives get coated on the surface of active material particles. The mixed powders are then loaded into a powder feeder, and then fluidized by the carrier gas. A spraying gun is used to charge the fluidized dry powders. After being charged, the dry powders are drawn to the grounded current collector and printed. A mask is used to pattern the sprayed materials into dish-shape for coin cell electrodes. Dry powders sprayed on the mask is recyclable. After the dry printing process, a hydraulic press is used for calendaring the dry sprayed electrodes into desired thickness with targeted porosity.

Besides the lower cost compared to conventional slurry casting method, another major advantage of this method is the tailorable porosity of electrodes from 26% to 59%, which is much wider than the porosity range processable by conventional slurry casting method. Porosity represents one of the main characteristics of the microstructures of the electrodes. The porosity of the dry-printed electrodes can be easily controlled by the pressure applied in the calendaring process. It is known that electrodes with higher porosity would have better Li-ion diffusivity in the electrolyte, which benefits the high-rate performance. With the solvent-free method, the porosity of electrodes can be made very high. It is necessary to find out whether there are other limiting factors for dry-printed electrodes with high porosity in the high-rate performance.

In this work, the high-rate performance of dry-printed electrodes with varied porosity is investigated and compared to the conventional slurry-casted electrodes. The electronic conductivity of these dry-printed electrodes is also evaluated to find out the

possible limiting factor for high-rate performance. Granular models are integrated in this work to simulate the interfacial-energy-driven dry powder mixing process. The percolating behavior of the conductive additives during the calendaring process is also studied with the granular models, which helps explain the change in electronic conductivity of electrodes with different porosity.

1.4. ORGANIZATION OF DISSERTATION

This dissertation is organized based on four publications. The first two publications mainly present the development of aerosol printing of current collectors and active materials of electrodes for LIBs. Whereas in the third publication, the as-developed techniques are utilized for the fabrication of customizable non-planar LIBs. In the fourth publication, the solvent-free additive manufacturing of electrodes for LIBs is researched focusing on the effect of the porosity of dry-printed electrodes.

PAPER

I. DIRECT AEROSOL PRINTING OF LITHIUM-ION BATTERIES

Xiaowei Yu[1], I-Meng Chen[1], Susmita Sarkar[1], Jonghyun Park[1], Heng Pan[1], Yangtao Liu[2], Yan Wang[2] and Wesley Everhart[3]

[1]Department of Mechanical and Aerospace Engineering,
Missouri University of Science and Technology, Rolla, MO 65409

[2]Department of Mechanical Engineering,
Worcester Polytechnic Institute, Worcester, MA 01609

[3]Honeywell Federal Manufacturing & Technologies LLC,
Kansas City National Security Campus, Kansas City, MO 64147

ABSTRACT

Recently, additive manufacturing (AM) has brought new opportunities to the manufacturing of lithium-ion batteries (LIBs). Aerosol jet printing, as a branch of AM technologies was firstly demonstrated to fabricate lithium-ion batteries. Printable inks of two pairs of active materials for cathode and anode were developed. The effect of ink composition on the printing characteristics was studied. The as developed inks were printed into Li-ion battery electrodes with good specific capacity compared to conventional slurry-casted electrodes. To further fabricate the fully-printed electrode, gold and copper were printed on top of glass/polymeric substrate and thermal/flash sintered as the current collector for cathode and anode. The fully-printed cell showed high capacity and good rate performance.

Key words: aerosol jet printing, additive manufacturing, printing, sintering, lithium-ion batteries

1. INTRODUCTION

Lithium-ion batteries (LIBs) have shown growing promise in home electronics, portable electronics and electric vehicles (EVs) due to the advantages of high energy density and long cycle life [1-5]. Commercial LIB electrodes are manufactured by casting a slurry onto a metallic current collector [6]. Alternatively, recent progress in additive manufacturing (AM) offers new opportunities for the manufacturing of batteries [7,8]. Battery cells or packs can potentially be manufactured additively to accommodate more flexibility in geometric designs, material and system integration [9-11]. In doing so, printable battery materials have to be developed for the additive manufacturing processes and electrode structure differences resulting from AM as compared to conventional processes need to be understood. Furthermore, AM battery packaging and system integration pose new challenges and opportunities for research.

Currently, the two main AM processes for fabricating batteries are extrusion-based 3D printing and ink jet printing. In extrusion-based 3D printing, ink containing electrode materials is ejected out of a nozzle by air pressure, and solidified into filaments [12-17]. Sun et. al fabricated an interdigitated 3D printed microbattery [12]. Fu et. al further worked on enhancing the conductivity of the 3D printed electrode by incorporating graphene oxide (GO) [13]. Hu et. al demonstrated a 3D printed cathode based on $LiMn_{0.21}Fe_{0.79}PO_4$@C (LMFP) [14]. Kohlmeyer et. al reported 3D printed Li-

ion battery electrodes utilizing 3D network of carbon nanofibers (CNFs) for applications of flexible batteries [15]. In inkjet printing, ink drop is driven by thermal, piezoelectric, or electrostatic actuation and delivered through a printing orifice [18]. There are several literatures reporting the use of inkjet printing for battery materials, but only very few cases discuss the use of ink-jet printing for LIB electrodes [19-22]. Zhao et. al reported the inkjet printing of $Li_4Ti_5O_{12}$ (LTO) electrodes [19]. Zhao et. al prepared SnO_2 ink by wet ball-milling and ink jet printed the ink into Li-ion cathode [20].

Aerosol jet printing is a new branch of AM technologies in which an aerosol mist, as opposed to the ink drops in ink jet printing, is used for printing [23,24]. It is compatible with various materials, including polymers, adhesives and functional nanoparticle (e.g. metallic, semiconductor, dielectric, and others) laden inks. The versatility of aerosol jet printing for a wide range of printable materials and substrates provides great potential for exploring the feasibility of fully-printed LIBs. Aerosol jet processes with an ultrasonic nebulizer have been reported to fabricate the crumpled graphene encapsulated Si nanoparticles for anode material [25-27]. However, to the best of our knowledge, aerosol jet printing to directly fabricate LIBs, has not been reported. This study aims at demonstrating the feasibility of using the aerosol jet process for fully-printed LIBs with focus on evaluating printability, functionality and compatibility of aerosol printable materials. Printable inks for anode, cathode and current collectors are developed, and then are directly aerosol jet printed into LIB electrodes assisted by flash annealing. The electrochemical properties are studied and compared to conventional slurry cast electrodes.

2. EXPERIMENTAL DETAILS

2.1. AEROSOL JET PRINTING METHOD

The aerosol mist is generated by an ultrasonic (Figure 1a) or pneumatic (Figure 1b) nebulizer and driven to a printing orifice by the gas flow. The aerosol jet printing system is capable of printing on planar and non-planar substrates with a minimum printed linewidth on the order of several microns. Particle-laden inks require particle size < 1 micron and viscosity in a specified range to allow printability. Glass, Polyimide (PI), modified Polyethylene terephthalate (PET) film and Polyethylene naphthalate (PEN) were selected for LIB substrates to evaluate their compatibility with the metallic nanoparticle (NP) sintering processes as well as the electrolyte.

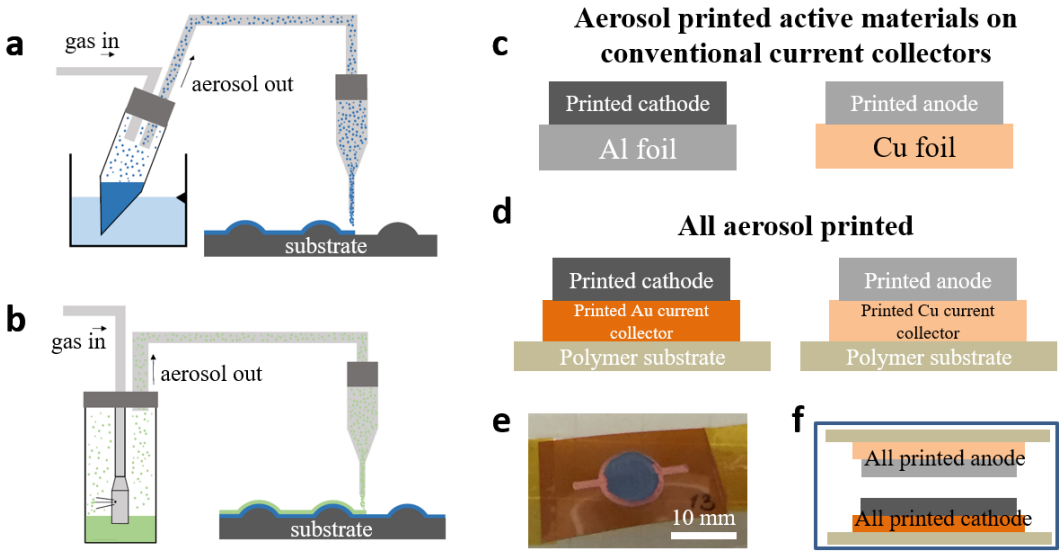

Figure 1. (a) Schematic of aerosol printing with ultrasonic nebulizer. (b) Schematic of aerosol printing with Collison nebulizer. (c) Schematic of the fabrication of cathode and anode for half-cell. (d) Schematic of the fabrication of cathode and anode for full-cell. (e) Photograph of an all-printed Cu/LTO anode on Polyimide substrate. (f) Schematic of the full-cell assembly.

2.2. PRINTING OF CURRENT COLLECTORS

Due to the high electrical conductivity and the compatibility with the LIB charging and discharging processes, gold (Au) and copper (Cu) were used as the current collectors for the cathode and anode, respectively. The Au ink (UT Dots, Inc) was printed using the ultrasonic nebulizer and printed through a 25-gauge (D=0.26 mm) nozzle with gas flow rate of 30 sccm. The printed Au pattern was first heated at 100 °C for 10 min to slowly evaporate the solvent in order to prevent the formation of a thin film on top of the material. The printed pattern was further heated to 250 - 300 °C for 1 h to sinter the Au NPs. Cu ink was prepared by dispensing Cu NPs (US Research Nanomaterials Inc.) in polyvinylpyrrolidone (PVP, Sigma-Aldrich)/N-Methyl-2-pyrrolidone (NMP, Sigma-Aldrich) solution. The ratio of Cu/PVP/NMP was 10/1/16.5. The ink was obtained by mixing (FlackTek Inc.) at 2000 rpm for 2 h and then ultrasonicating for 1 h. The as prepared ink was printed by Collison nebulizer with a 21-gauge (D=0.514 mm) nozzle with gas flow rate of 0.5 LPM. The printed Cu pattern was sintered with a photonic sintering system (Sinteron 2000-L, Xenon Corporation, 2.5 kV, single pulse).

2.3. PRINTING OF ACTIVE MATERIALS

Two pairs of cathode/anode active materials were used to demonstrate the versatility of aerosol jet printed LIBs: lithium manganese oxide (LMO)/graphite and lithium ion phosphate (LFP)/lithium titanate (LTO). All the aerosol printable inks were prepared by mixing dry nanopowders with polyvinylidene fluoride (PVDF, Sigma-Aldrich) and carbon black (CB, Super C65, Timcal) in NMP. PVDF was first dissolved in NMP for at least 8 h and then the solution was mixed with dry powders of active

material and CB for 40 min at 2000 rpm. The optimal ink compositions and printing parameters that were obtained are summarized in Table 1. After printing, the active materials were baked in a vacuum oven at 120 °C for at least 8 h before testing battery performance.

Table 1. Optimal ink composition and printing parameters used for aerosol printing.

Active Material (AM)	NP size	Ink Composition (wt%, AM/PVDF/CB/NMP)	Printing Parameters (flow rate, nozzle size)
LMO	<500nm	21.23/0.22/0.55/78	0.4 LPM, 21 gauge
Graphite	<1.2μm	16.67/0.75/0.75/85	0.7 LPM, 20 gauge
LFP	<400nm	20.68/0.66/0.66/78	0.4 LPM, 21 gauge
LTO	<200nm	16.67/0.75/0.75/85	0.5 LPM, 21 gauge

2.4. BATTERY ASSEMBLY AND CHARACTERIZATION

To quantitatively compare the properties of printed electrodes with conventionally cast electrodes, printed electrodes were characterized using a half-cell configuration with conventional sandwich architecture using Al and Cu foils as current collectors (Figure 1c). Then, active materials were printed on top of Au and Cu current collectors fabricated by aerosol printing and thermal/flash sintering (Figure 1d and 1e). Finally, all printed cathode and anode materials were assembled in a full cell (CR2032 coin cell, Welkos Corp.) as shown in Figure 1f. The rate performance was characterized with charging and discharging rate ranging from 0.1 C to 3 C.

3. RESULTS AND DISCUSSION

3.1. PRINTING CHARACTERISTICS AND PRINTED ELECTRODE COMPOSITION

Active materials were firstly printed on top of conventional current collectors (Al and Cu foils) for half-cell testing. The composite ink of active materials contains four components: active material as the functional element of battery electrode, CB as the conductive additive, PVDF as the binder, and NMP as the solvent. To ensure good performance of the printed battery, it is essential to ensure sufficient mixing and distribution of the CB, PVDF and active material in the printed electrode.

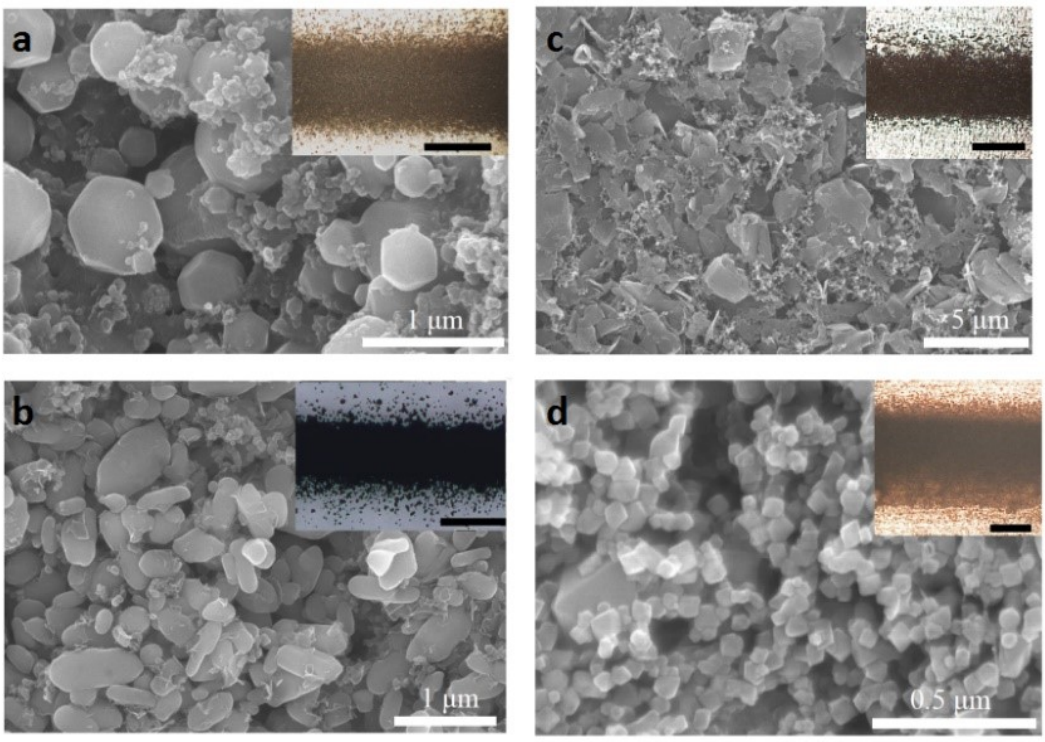

Figure 2. SEM images of printed active materials: (a) LMO, (b) LFP, (c) graphite and (d) LTO. Insets are the microscopic images of printed lines (scale bar = 200 μm).

Figure 2a-d are SEM images of the printed active materials with optimal ink composition as listed in Table 1. As seen from the SEM images, PVDF was completely dissolved and attached to the active material particles and CB with a particle size of around 50 nm was well-distributed among the active materials.

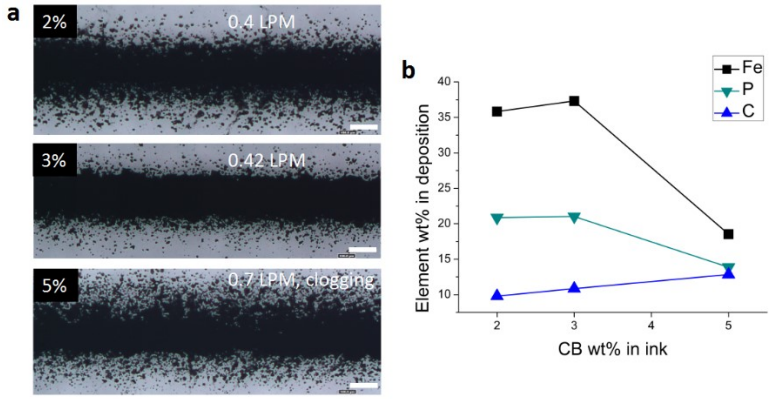

Figure 3. (a) Microscopic images of printed lines of LFP with 2, 3 and 5 wt% CB in ink (scale bar = 100 μm). (b) Effect of CB content in ink on various elements in the printed electrodes.

As the CB content is critical for electrode conductivity, CB content was varied to understand its impact on printability and electrode composition. LFP inks with CB concentrations of 2, 3 and 5 wt% were printed. The morphology of printed lines is shown in Figure 3a. With the concentration of CB increased from 2 to 5 wt%, the gas flow rate required to nebulize the materials increased from 0.4 to 0.7 LPM. The printed line of 3 wt% ink was more concentrated with less stray particles compared to 2 wt%. The 5 wt% ink experienced clogging of the nozzle and its printed line has significantly less material. Energy Dispersive Spectroscopy (EDS) was used to quantify the composition of the

printed electrodes. It was found the CB content in the printed electrodes increased monotonically with the increasing CB loading in the ink, while active materials (as indicated by Fe and P) started to drop as CB increased above 3 wt% (Figure 3b). Therefore, to avoid nozzle clogging and depletion of active materials, the CB content in the LFP ink should be limited below 5 wt%.

3.2. ELECTROCHEMICAL PROPERTY OF PRINTED ACTIVE MATERIALS ON METAL FOILS AS CURRENT COLLECTORS

The electrochemical properties of the four printed electrodes on metal foils were characterized and compared to the conventional slurry cast electrodes. The electrodes were tested with constant current at C-rate of 0.1 and the specific capacity was calculated accordingly. The capacity of printed electrodes, the conventional slurry cast electrodes and the theoretical capacity of the corresponding active materials are summarized in Table 2. For all of the four printed electrodes, the capacity was comparable to the slurry cast electrodes and slightly lower than the theoretical values.

Table 2. Specific capacity of printed electrodes and slurry cast electrodes.

Active material	Capacity (mAh/g)		
	Aerosol printed electrode	Slurry cast electrode	Theoretical value
LMO	80	100	148
LFP	160	150	170
Graphite	350	350	372
LTO	160	175 [28]	175

Rate performance testing results were compared between printed and slurry cast LFP electrodes, as in Figure 4a (printed) and b (slurry cast). The slurry cast electrodes showed better performance at high rates (>1 C). It is known that LFP has low conductivity, thus the amount and distribution of conductive carbon are important in determining the rate performance. It is possible that the aerosol printed electrode has less carbon (or different carbon distribution) compared with slurry cast electrode, which could explain the reduced performance at high rates.

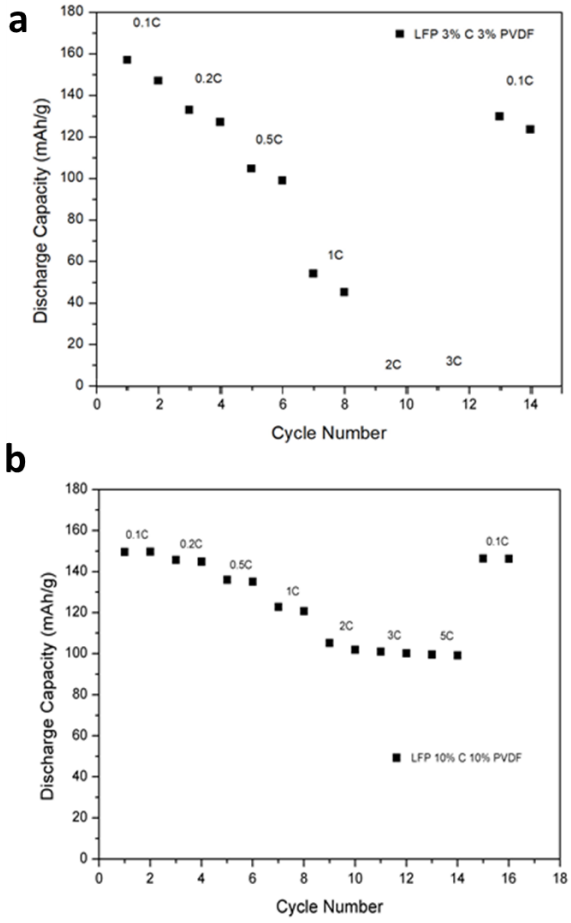

Figure 4. (a) C-rate performance of printed LFP electrode. (b) C-rate performance of slurry cast LFP electrode.

3.3. ELECTROCHEMICAL PROPERTY OF FULLY-PRINTED ELECTRODES (PRINTED ACTIVE MATERIALS ON PRINTED CURRENT COLLECTORS)

After demonstrating the feasibility of aerosol jet printing of active materials on conventional current collectors, active materials were printed on current collectors fabricated by aerosol printing and flash/thermal annealing of metal NP. Figure 5a shows a SEM image of the printed and thermal sintered Au on glass. The particle size before sintering is 3-5 nm. Significant grain growth with grain size up to 100 nm was observed after sintering.

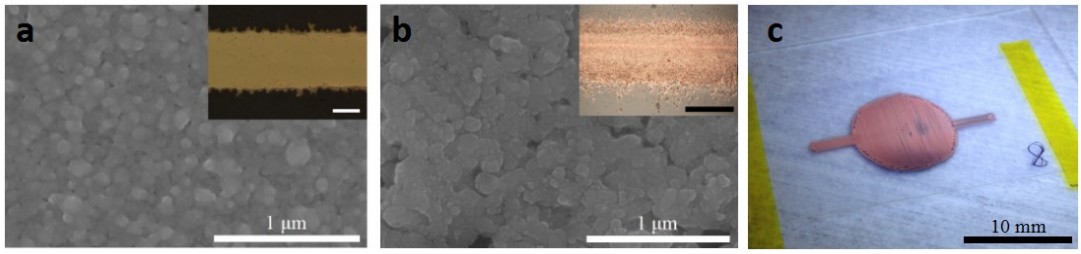

Figure 5. SEM images of printed current collectors: (a) Au and (b) Cu. Insets are the microscopic images of printed lines (scale bar = 200 µm). (c) Photograph of Cu current collector on flexible plastic substrate (PET).

Compact contact and coalescence of grains ensured good conductivity of the printed Au film. The sintered Au film with sheet resistance under 10Ω/sq was obtained. Gold NP were also printed on PET, PEN and PI substrates. After thermal sintering at 300 °C, a highly conductive film could be obtained on the PI substrate. Flash sintering was performed to obtain Au electrode with sheet resistance under 10Ω/sq on PEN and PET. LFP electrode was then printed on the Au current collectors for electrochemical testing.

Figure 6 shows performance of LFP electrode on printed Au current collector with PI substrate. The charge and discharge capacity are 136.19 mAh/g and 125.22 mAh/g respectively. This result showed that printed/sintered Au NP film on PI polymer substrate is eligible as a cathode current collector for Li-ion batteries.

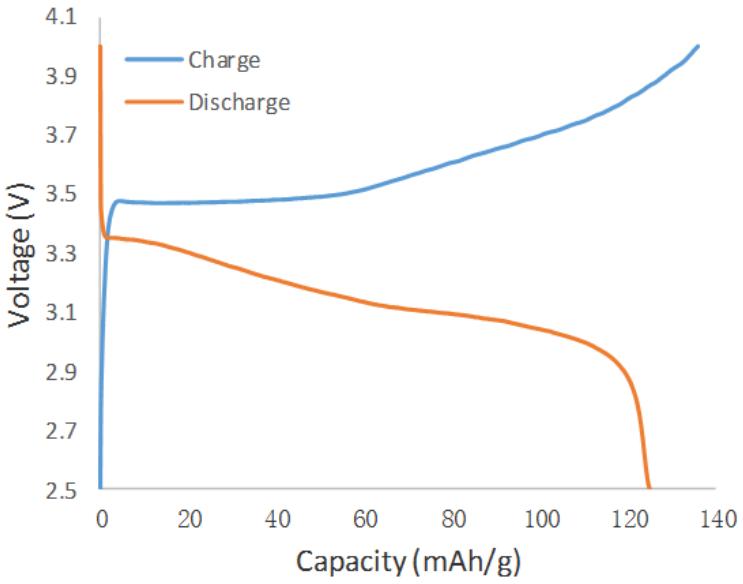

Figure 6. Charge and discharge performance of LFP/Au on PI substrate under 0.1 C.

Compared to Au, Cu is prone to oxidation in ambient atmosphere at elevated temperature. To avoid that, flash sintering [29,30] was used in this study for the printed Cu patterns. Similar grain growth and coalescence was observed in Figure 5b. Cu NP were printed on PET, PEN and PI substrates. After flash annealing, the current collector was fabricated on the flexible plastic substrate (in Figure 5c) with sheet resistance under 10 Ω/sq. The LTO electrode was then printed on the Cu current collector for electrochemical testing.

Figure 7 shows the rate performance of LTO/Cu on PET and LTO/Cu on PI between 1V-2.4V. The specific capacity for LTO/Cu on PET and PI were 82.3 mAh/g and 105.2 mAh/g respectively. The two electrodes still had capacity of 60 mAh/g and 70 mAh/g capacity with current at 3C, which indicated the excellent rate capability of LTO on printed current collectors. This result showed flash sintered Cu NP on polymer substrates could function as the current collector for anode. PI and PET exhibit acceptable chemical compatibility with the electrolyte during charging and discharging cycles.

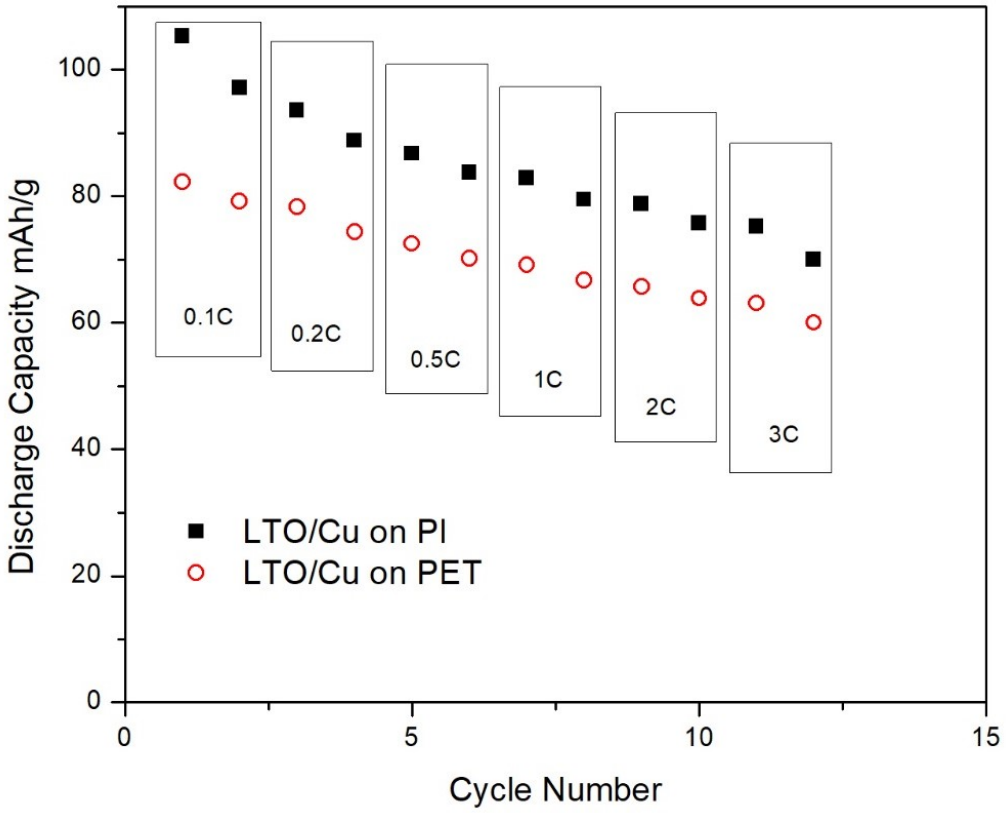

Figure 7. Rate performance from 0.1C to 3C of printed LTO/Cu electrodes on PI and PET substrates.

4. CONCLUSIONS

In this paper, we reported the feasibility of aerosol jet printing for fabricating fully-printed Li-ion batteries. Aerosol printable inks containing active materials were developed and electrochemical performance of printed electrodes was characterized. The printed electrodes showed good capacity, but less satisfactory high-rate performance compared to conventional slurry cast electrodes. Current collectors were printed, and thermal/flash sintered on top of glass/polymeric substrate for the fabrication of fully-printed cell. The fully-printed cell showed high capacity and good rate performance.

ACKNOWLEDGEMENT

All data prepared, analyzed and presented has been developed in a specific context of work and was prepared for internal evaluation and use pursuant to that work authorized under the referenced contract. Reference herein to any specific commercial product, process or service by trade name, trademark, manufacturer, or otherwise, does not necessarily constitute or imply its endorsement, recommendation, or favoring by the United States Government, any agency thereof or Honeywell Federal Manufacturing & Technologies, LLC. This presentation has been authored by Honeywell Federal Manufacturing & Technologies under Contract No. DE-NA0002839 with the U.S. Department of Energy. The United States Government retains and the publisher, by accepting the article for publication, acknowledges that the United States Government retains a nonexclusive, paid up, irrevocable, world-wide license to publish or reproduce

the published form of this manuscript, or allow others to do so, for the United States Government purposes.

REFERENCES

[1] Etacheri, V., et al., "Challenges in the development of advanced Li-ion batteries: a review", Energy & Environmental Science, Vol. 4, pp. 3243-3262, July, 2011.

[2] Li, W., X. Sun, and Y. Yu, Si-, Ge-, "Sn-Based Anode Materials for Lithium-Ion Batteries: From Structure Design to Electrochemical Performance", Small Methods, Vol. 1, No. 1600037, March, 2017.

[3] Xie, K. and B. Wei, "Materials and Structures for Stretchable Energy Storage and Conversion Devices", Advanced Materials, Vol. 26, pp. 3592-3617, June, 2014.

[4] Tarascon, J.M. and M. Armand, "Issues and challenges facing rechargeable lithium batteries", Nature, Vol. 414, pp. 359-367, November, 2001.

[5] Gwon, H., et al., "Recent progress on flexible lithium rechargeable batteries", Energy & Environmental Science, Vol. 7, pp. 538-551, December, 2013.

[6] Ludwig, B., et al., "Solvent-Free Manufacturing of Electrodes for Lithium-ion Batteries", Scientific Reports, Vol. 6, No. 23150, March, 2016.

[7] Cobb, C.L. and C.C. Ho, "Additive Manufacturing: Rethinking Battery Design", The Electrochemical Society Interface, Vol 25, pp. 75-78, 2016.

[8] Fu, K., et al., "Progress in 3D Printing of Carbon Materials for Energy-Related Applications", Advanced Materials, Vol. 29, No. 1603486, March, 2017.

[9] Hu, Y. and X. Sun, "Flexible Rechargeable Lithium Ion Batteries: Advances and Challenges in Materials and Process Technologies", Journal of Materials Chemistry A, Vol. 228, pp. 10712-10738, April, 2014.

[10] Gaikwad, A.M., A.C. Arias, and D.A. Steingart, "Recent Progress on Printed Flexible Batteries: Mechanical Challenges, Printing Technologies, and Future Prospects", Energy Technology, Vol. 3, pp. 305-328, April, 2015.

[11] Sousa, R.E., C.M. Costa, and S. Lanceros-Méndez, "Advances and Future Challenges in Printed Batteries", ChemSusChem, Vol. 8, pp. 3539-3555, November, 2015.

[12] Sun, K., et al., "3D Printing of Interdigitated Li-ion Microbattery Architectures", Advanced Materials, Vol. 25, pp. 4539-4543, September, 2013.

[13] Fu, K., et al., "Graphene Oxide-Based Electrode Inks for 3D-Printed Lithium-Ion Batteries", Advanced Materials, Vol. 28, pp. 2587-2594, April, 2016.

[14] Hu, J., et al., "3D-Printed Cathodes of LiMn1−xFexPO4 Nanocrystals Achieve Both Ultrahigh Rate and High Capacity for Advanced Lithium-Ion Battery", Advanced Energy Materials, Vol. 6, No. 1600856, September, 2016.

[15] Kohlmeyer, R.R., et al., "Composite batteries: a simple yet universal approach to 3D printable lithium-ion battery electrodes", Journal of Materials Chemistry A, Vol. 4, pp. 16856-16864, October, 2016.

[16] Li, J., et al., "A Hybrid Three-dimensionally Structured Electrode for Lithium-ion Batteries via 3D Printing", Materials & Design, Vol. 119, pp. 417-424, April, 2017.

[17] Ho, C.C., J.W. Evans, and P.K. Wright, "Direct write dispenser printing of a zinc microbattery with an ionic liquid gel electrolyte", Journal of Micromechanics and Microengineering, Vol. 20, No. 10, September, 2014.

[18] Saunders, R.E. and B. Derby, "Inkjet Printing Biomaterials for Tissue Engineering: Bioprinting", International Materials Reviews, Vol. 59, pp. 430-448, July, 2014.

[19] Zhao, Y., et al., "High-performance Thin-film Li4Ti5O12 Electrodes Fabricated by Using Ink-jet Printing Technique and Their Electrochemical Properties", Journal of Solid State Electrochemistry, Vol. 13, pp. 705-711, June, 2008.

[20] Zhao, Y., et al., "A Novel and Facile Route of Ink-jet Printing to Thin Film SnO2 Anode for Rechargeable Lithium Ion Batteries", Electrochimica Acta, Vol. 51, pp. 2639-2645, March, 2006.

[21] Ho, C.C., et al., "A Super Ink Jet Printed Zinc–Silver 3D Microbattery", Journal of Micromechanics and Microengineering, Vol. 19, No. 9, August, 2009.

[22] Janoschka, T., et al., "Reactive Inkjet Printing of Cathodes for Organic Radical Batteries", Advanced Energy Materials, Vol. 3, pp. 1025-1028, August, 2013.

[23] Seifert, T., et al., "Additive Manufacturing Technologies Compared: Morphology of Deposits of Silver Ink Using Inkjet and Aerosol Jet Printing", Industrial and Engineering Chemistry Research, Vol. 54, pp. 769-779, January, 2015.

[24] Zhao, D., et al., "Conductivity Enhancement of Aerosol-jet Printed Electronics by Using Silver Nanoparticles Ink with Carbon Nanotubes", Microelectronic Engineering, Vol. 96, pp. 71-75, August, 2012.

[25] Kim, S.K., et al., "One-Step Formation of Silicon-Graphene Composites from Silicon Sludge Waste and Graphene Oxide via Aerosol Process for Lithium Ion Batteries", Scientific Reports, Vol. 6, No. 33688, September, 2016.

[26] Luo, J., et al., "Crumpled Graphene-Encapsulated Si Nanoparticles for Lithium Ion Battery Anodes", Journal of Physical Chemistry Letter, Vol. 3, pp. 1824-1829, June, 2012.

[27] Wen, Y., et al., "Graphene-Bonded and -Encapsulated Si Nanoparticles for Lithium Ion Battery Anodes", Small, Vol. 6, pp. 2810-2816, August, 2013.

[28] Yu, S.-H., et al., "Surfactant-Free Nonaqueous Synthesis of Lithium Titanium Oxide (LTO) Nanostructures for Lithium Ion Battery Applications", Journal of Materials Chemistry, Vol. 21, pp. 806-810, November, 2010.

[29] Norita, S., et al., "Inkjet-printed Copper Electrodes Using Photonic Sintering and Their Application to Organic Thin-film Transistors", Organic Electronics, Vol. 25, pp. 131-134, October, 2015.

[30] Kang, H., E. Sowade, and R.R. Baumann, "Direct Intense Pulsed Light Sintering of Inkjet-Printed Copper Oxide Layers within Six Milliseconds", ACS Applied Materials & Interfaces, Vol. 6, pp. 1682-1687, January, 2014.

II. AEROSOL JET PRINTING OF ELECTRODES FOR LITHIUM-ION BATTERIES

Xiaowei Yu[1], Yangtao Liu[2], Susmita Sarkar[1], I-Meng Chen[1], Wesley Everhart[3], Jonghyun Park[1], Yan Wang[2] and Heng Pan[1]

[1]Department of Mechanical and Aerospace Engineering,
Missouri University of Science and Technology, Rolla, MO 65409

[2]Department of Mechanical Engineering,
Worcester Polytechnic Institute, Worcester, MA 01609

[3]Honeywell Federal Manufacturing & Technologies LLC,
Kansas City National Security Campus, Kansas City, MO 64147

ABSTRACT

Lithium-ion batteries (LIBs), one of the most popular energy storage devices, have shown great promise in sustainable energy strategy due to the rechargeability and high energy density. The development of additive manufacturing (AM) has brought new opportunities to the design and fabrication of LIBs. In this study, aerosol jet printing (AJP), as a novel AM process is demonstrated for the fabrication of electrodes for LIBs. This study is aimed at demonstrating basic principles of this aerosol-based process for additively manufactured LIB electrodes with focus on printability and electrochemical functionality. Inks for AJP of the current collectors and four common active materials for LIBs are developed. The printed current collectors show excellent electrical conductivity. The printed electrodes with the four active materials all show satisfactory capacity and cyclic performance.

Key words: aerosol jet printing, additive manufacturing, printing, lithium-ion batteries, electrodes

1. INTRODUCTION

In the past decades, novel energy harvesting and storage devices have been continuously investigated in the pursuit of renewable and sustainable energy resources. Lithium-ion batteries (LIBs), as the most developed type of electrochemical energy storage devices, have shown growing promise in home electronics, portable electronics and electric vehicles (EVs) due to the advantages of rechargeability and high energy density [1,2]. Commercial LIB electrodes are manufactured by casting a slurry onto a metallic current collector [3]. Recently, the development of additive manufacturing (AM) has brought new opportunities to the design and fabrication of LIBs with the on-demand and layer-by-layer manufacturing schemes [4,5].

Currently reported AM processes for fabricating LIBs are mostly based on extrusion-printing [6-9]. In this method, active materials are directly deposited powered by ultra-high air pressure and solidified into filaments. Despite the advantages of high printing speed and yield, extrusion-printing requires the inks to be solidified right after extrusion. The processable inks are usually paste-like with high viscosity and shear-thinning characteristics, which has strict requirements on the equipment capabilities and maintenance efforts (such as clogging prevention). As an alternative, aerosol jet printing (AJP) utilizes moderate pressurized air to nebulize the active materials in the ink into aerosol mist and to drive the precise material deposition [10,11]. AJP processes a wide

variety of materials, including polymers, metals, semiconductors, carbon-based materials and energy materials in laden inks with viscosity ranging from 1 cP to 1,000 cP [12-14]. Due to flexible working distance from the deposition nozzle to the substrate, AJP is also capable of deposition on non-planar structures as trenches and periodic wavy structures [15].

This study is aimed at demonstrating basic principles of using AJP for additively manufactured LIB electrodes with focus on material printability and electrochemical functionality. Printable inks for anodes, cathodes and current collectors are developed. The printed current collectors are either thermally annealed or annealed with the assist of pulsed flash light. After annealing the printed current collectors show excellent electrical conductivity. The printed cathode and anode materials are examined in terms of the line morphology and microstructures. To study the electrochemical performances of the LIB electrodes by AJP, they are characterized using a sandwich architectured half-cell configuration. In galvanostatic cycling test, all printed electrodes show satisfactory capacity and cyclic performance.

2. EXPERIMENTAL DETAILS

AJP of current collectors: Due to the high electrical conductivity and the compatibility with the LIB charging and discharging processes, gold (Au) and copper (Cu) were chosen as the current collectors for the cathode and anode. The Au ink (UT Dots, Inc) was printed using an ultrasonic nebulizer with gas flow rate of 30 sccm. The printed Au was first heated at 100 °C for 10 min to slowly evaporate the solvent then

annealed at 300 °C for 1 h. Cu ink was prepared by dispensing Cu NPs (US Research Nanomaterials Inc.) in polyvinylpyrrolidone (PVP)/N-Methyl-2-pyrrolidone (NMP) solution in the weight ratio of 10/1/16.5. The ink was homogenized by high-speed mixing (FlackTek Inc.) and ultrasonicating. The as prepared ink was printed by a Collison nebulizer with gas flow rate of 0.5 LPM. The printed Cu pattern was sintered with a photonic sintering system (Sinteron 2000-L, Xenon Corporation, 2.5 kV, single pulse).

AJP of active materials: Two active materials for cathode and two active materials for anode were studied to demonstrate the versatility of LIB electrodes by AJP: lithium manganese oxide (LMO), lithium ion phosphate (LFP) for cathode and graphite, lithium titanate (LTO) for anode. The reason for choosing these four active materials are that LMO/graphite and LFP/LTO are the two most popular electrode pairs for LIBs. All the active material inks were prepared by mixing dry nanopowders with polyvinylidene fluoride (PVDF, Sigma-Aldrich) and carbon black (CB, Super C65, Timcal) in NMP. The weight ratios of additives in all solid materials were <10%. PVDF was first dissolved in NMP for at least 8 h and then the solution was mixed with dry powders of active material and CB for 40 min at 2000 rpm. The inks of active materials were printed by Collison nebulizer with gas flow rate ranging from 0.4-0.7 LPM. The amount of materials deposited can be tailored by adjusting the gas flow rate, stage speed and size of printing orifice. After printing, the active materials were baked in a vacuum oven at 120 °C for 8 h to fully remove the solvent.

Assembly of LIBs: The printed electrodes were assembled in CR2032 coin cell with Celgard separator and liquid electrolyte 1 M $LiFP_6$ in EC:DMC 1:1 (Sigma-Aldrich). Li foil was used as the counter electrode for electrochemical testing of half-

cells. All the assembly processes were conducted in an argon-filled glove box (Mbraun) with oxygen and moisture content <0.5 ppm.

Characterizations: Morphology of the printed materials was examined by an optical digital microscope (Hirox KH-8700). Microstructures and cross-sections of the printed materials were observed by scanning electron microscopy (SEM, Hitachi S-4700). Energy-dispersive X-ray spectroscopy (EDS) in the above SEM system was used to analyze the element content in the printed samples. The galvanostatic cycling test was performed at charging/discharging rate of 0.1 C.

3. RESULTS AND DISCUSSION

The setup of AJP is shown in Figure 1a. In AJP process, carrier gas is sent to either ultrasonic nebulizer or Collison nebulizer. In ultrasonic nebulizer, the liquid in the ink is broken down by the ultrasonic waves into micron-size particles in vapor phase. Whereas in Collison nebulizer, the ink is refined and aspirated into the gas jet and sheared into micron-size droplets in aerosol mists. The generated aerosol mists are driven to the printing orifice by the same carrier gas. An XY-stage is used to mount the substrate and realize the patterning for the additive purpose. In this study, the current collectors, cathodes, and anodes are all fabricated by AJP. To demonstrate the capability of AJP for the fabrication LIB electrodes, the electrodes for conventional sandwich structure of LIBs are printed and tested. Photographs of the printed cathode on printed Au current collector and printed anode on printed Cu current collector are respectively shown in Figure 1b and 1c. The sandwich architecture of the LIBs (full-cells) is illustrated in Figure 1d. For the

half-cells, Li metal is used as the counter electrode (replacing the electrode and current collector at one side).

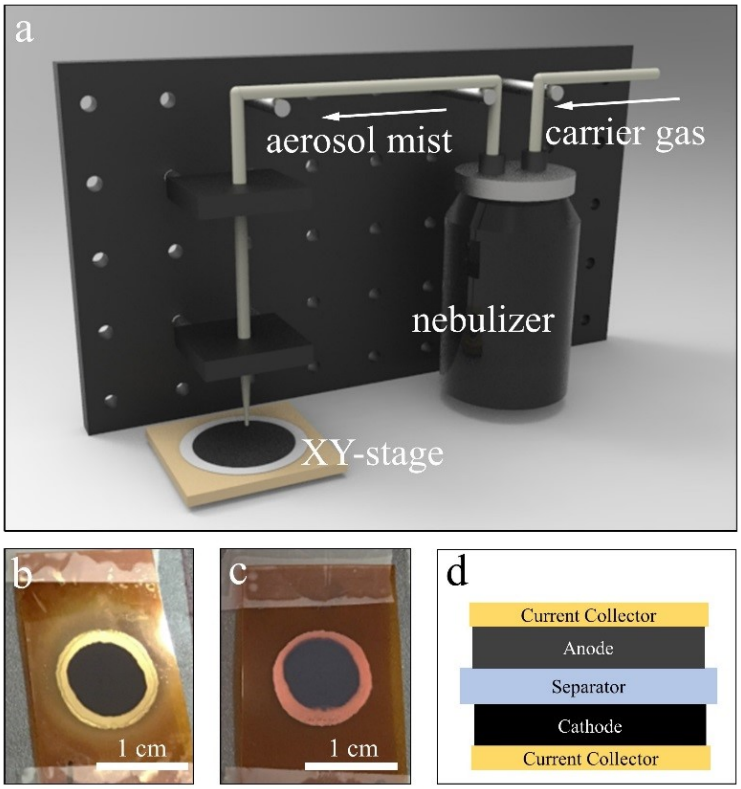

Figure 1. (a) Setup of AJP. (b) Photograph of printed cathode on printed Au current collector. (c) Photograph of printed anode on printed Cu current collector. (d) Schematic showing the sandwich structure of LIBs.

The fabrication of current collectors by AJP starts from the printing of metallic nanoparticles (NPs). The printed patterns are barely conductive because the NPs remain electrically separate after deposition onto the substrate and the contact between the neighboring NPs is hindered by the coated polymers. Annealing is necessary as the post-process to coalesce the printed NPs for electrical continuity. Figure 2a shows an SEM

image of the printed and annealed Au current collector. After thermal annealing at 300 °C, highly electrically conductive films are obtained. The particle size before annealing is 3-5 nm. Significant grain growth with grain size up to 100 nm can be observed after annealing.

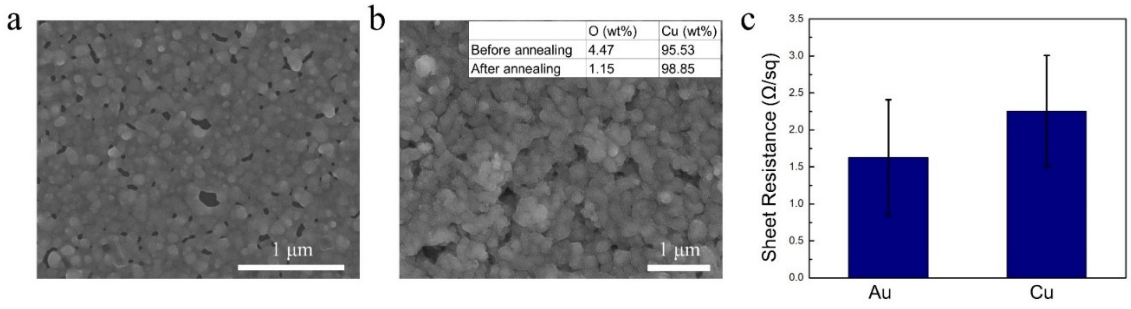

Figure 2. (a) SEM image of the printed and thermally annealed Au current collector. (b) SEM image of the printed and flash light annealed Cu current collector. (c) Sheet resistance of the Au and Cu current collectors.

Compared to Au, Cu is prone to oxidation in ambient atmosphere at elevated temperature which adversely affects the electrical conductivity. Here, the printed Cu current collector is annealed by pulsed flashlight. During annealing process, the pulsed xenon lamp emits a light pulse with a duration of 2 milliseconds. The ultra-rapid annealing process helps the coalesce of NPs and prevents the formation of oxides as well. Similar grain growth and coalescence of Cu NPs can be observed in the SEM images in Figure 2b. In the inset of Figure 2b, the EDS results of the printed Cu before and after annealing are given. As seen from the data, the oxygen content is significantly decreased after flash light annealing. The sheet resistances of the printed Au and Cu current collectors are given in Figure 3c. Sheet resistances of printed Au and Cu are 1.63±0.77

Ω/sq and 2.25±0.75 Ω/sq respectively. The reason that the resistance of Cu is a bit higher than Au is still attributed to the oxidation problem. The electrical conductivity of Cu might be improved by annealing it in argon-filled enclosure to insulate the oxygen.

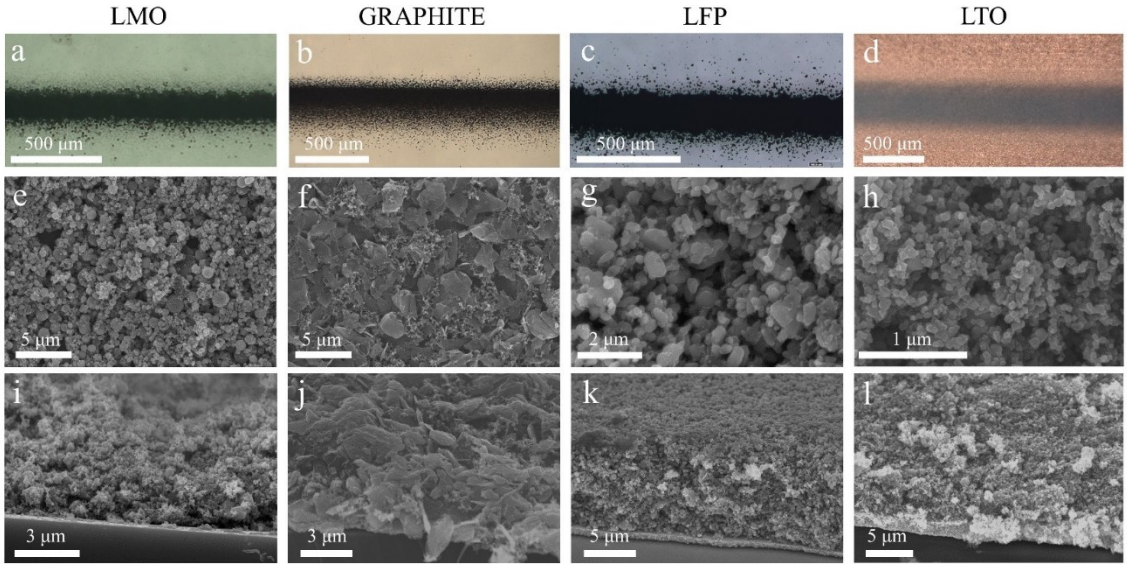

Figure 3. Optical microscopy images of (a) LMO, (b) graphite, (c) LFP and (d) LTO. Top-view SEM images of (e) LMO, (f) graphite, (g) LFP and (h) LTO. Cross-section SEM images of (i) LMO, (j) graphite, (k) LFP and (l) LTO.

Active materials are firstly printed in lines to evaluate the morphology of the printed features and the microstructures of the printed materials. The optical microscopy images of the printed lines of LMO, graphite, LFP and LTO are shown in Figure 3a-d. As seen from the images, LFP and LTO have higher linewidth compared to LMO and graphite. The particle sizes of LMO, graphite, LFP and LTO are 500 nm, 1.2 µm, 400 nm and 50-100 nm respectively. Among these materials, graphite has the largest particle size, so the gas flow rate used to print graphite is the highest (0.7 LPM). As the result of high

gas flow rate, there are more splattered droplets near the edge of the printed line of graphite. The inks of active materials are composite inks containing four components: active materials as the functional element of LIB electrodes, CB as the conductive additive, PVDF as the binder, and NMP as the solvent. Different from the extrusion-printing where the compositions remain the same before and after extrusion, the materials compositions of ink and deposition of AJP are different and more complicated. During the AJP process, the solvent partially evaporates because of the accelerated gas flow. As a result, the materials reaching the substrates are already partially dried, which helps maintain the designed geometry of the printed structures.

To ensure good performance of the printed battery, it is essential to ensure uniform distribution of the active materials and the additives in the printed electrodes. Especially the CB as conductive additives are of great importance for the electron transportation throughout the electrodes. Figure 3e-h are the SEM images of the printed active materials. As seen from the SEM images, PVDF is completely dissolved and coated on particles of active materials and CB. This ensures the good bonding among the neighboring materials and between electrode and current collector. The CB with a particle size of ~50 nm are clustered around the active materials, forming the electrical conductive paths. The cross-section SEM images of the printed active materials are presented in Figure 3i-l. As seen from the cross-section images, the thickness of the printed active materials is in the range of 3-10 μm, which is lower than most of conventional slurry-casted electrodes. It is worth-noticing that the results here are all obtained by single-layer printing. The thickness and areal mass loading of the printed active materials and then could be further increased by multi-layer printing.

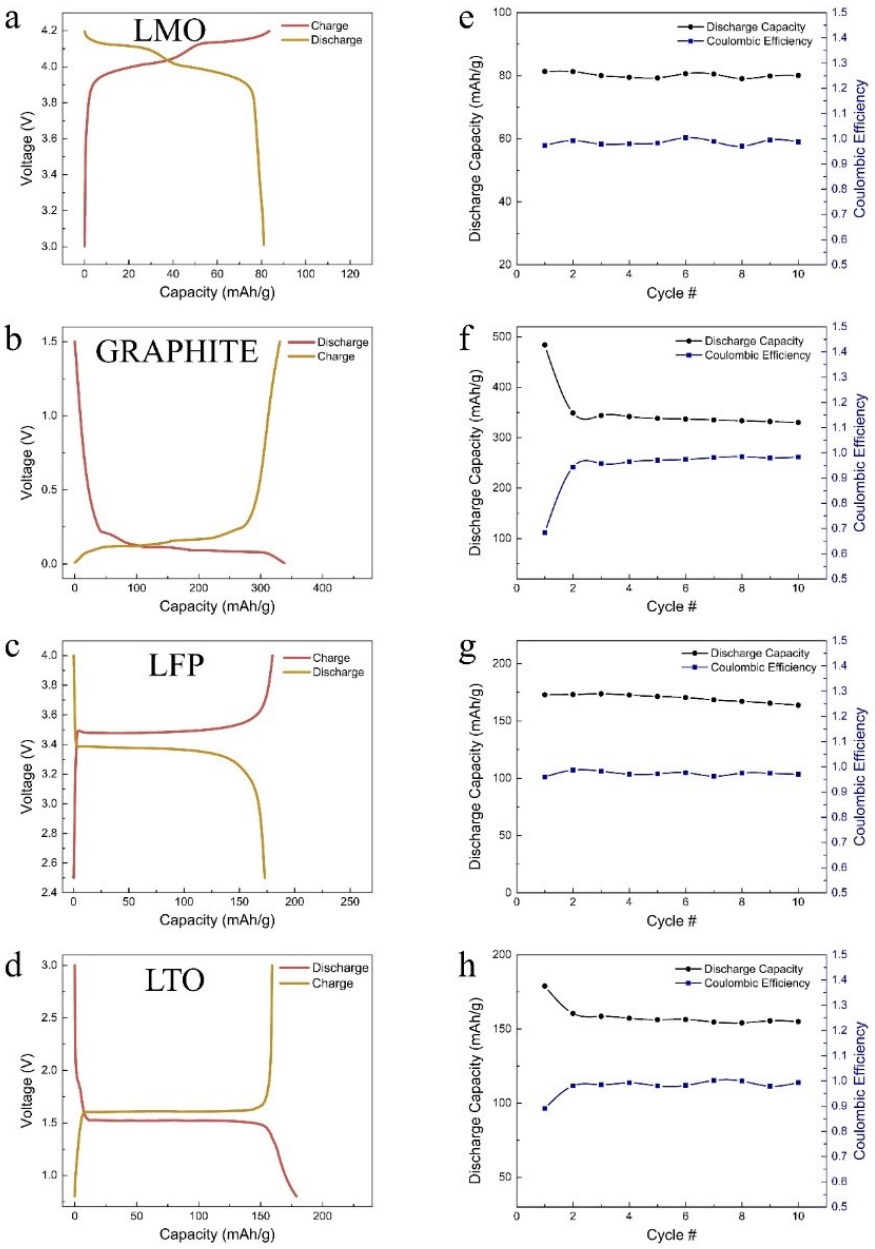

Figure 4. Charging and discharging profiles of (a) LMO, (b) graphite, (c) LFP and (d) LTO. Specific capacity and Coulombic efficiency versus cycle of (e) LMO, (f) graphite, (g) LFP and (h) LTO.

Next, the active materials are printed into planar circular shape on current collectors as the LIB electrodes. The printed electrodes are assembled in commercial coin

cells and their electrochemical performances are tested by galvanostatic cycling method. The charging and discharging profiles of the printed LIB electrodes are shown in Figure 4a-d. For these four materials, charging and discharging profiles match the corresponding conventionally processed electrodes with obvious plateaus in both charging and discharging process. For the two anode materials (graphite and LTO), the first discharging cycle has longer duration due to the formation of SEI layers, so the profiles are plotted starting from the second cycle. The specific capacity and Coulombic efficiency with cycles of the printed LIB electrodes are plotted in Figure 4e-h. As seen from the results, all the four printed electrodes showed acceptable cycling performance without capacity fade after 10 cycles. Except for the first cycle of anode materials, Coulombic efficiency of these four active materials are all highly approaching 100%. The specific capacities of the printed LMO, graphite, LFP and LTO are around 82, 345, 173 and 161 mAh/g, which are very near to the theoretical capacities and are all in the acceptable range to demonstrate a working LIB electrode.

4. CONCLUSIONS

In this study, we report the feasibility of AJP as one of the AM process for the fabrication of electrodes for LIBs. The printed and annealed Au and Cu are of high conductivity and are qualified for the current collectors of LIBs. AJP of composite inks of active materials are successfully carried out with uniform distribution of active materials and additives. The galvanostatic cycling test results show that the four active materials by AJP all exhibit satisfactory capacity and cyclic performance.

ACKNOWLEDGEMENT

All data prepared, analyzed and presented has been developed in a specific context of work and was prepared for internal evaluation and use pursuant to that work authorized under the referenced contract. Reference herein to any specific commercial product, process or service by trade name, trademark, manufacturer, or otherwise, does not necessarily constitute or imply its endorsement, recommendation, or favoring by the United States Government, any agency thereof or Honeywell Federal Manufacturing & Technologies, LLC. This presentation has been authored by Honeywell Federal Manufacturing & Technologies under Contract No. DE-NA0002839 with the U.S. Department of Energy. The United States Government retains and the publisher, by accepting the article for publication, acknowledges that the United States Government retains a nonexclusive, paid up, irrevocable, world-wide license to publish or reproduce the published form of this manuscript, or allow others to do so, for the United States Government purposes.

REFERENCES

[1] Tarascon, J-M., and Michel Armand. "Issues and challenges facing rechargeable lithium batteries." Materials For Sustainable Energy: A Collection of Peer-Reviewed Research and Review Articles from Nature Publishing Group. 2011. 171-179.

[2] Li, Weihan, Xueliang Sun, and Yan Yu. "Si-, Ge-, Sn-Based Anode Materials for Lithium-Ion Batteries: From Structure Design to Electrochemical Performance." Small Methods 1.3 (2017): 1600037.

[3] Ludwig, Brandon, et al. "Solvent-free manufacturing of electrodes for lithium-ion batteries." Scientific reports 6 (2016): 23150.

[4] Cobb, Corie L., and Christine C. Ho. "Additive Manufacturing: Rethinking Battery Design." The Electrochemical Society Interface 25.1 (2016): 75-78.

[5] Zhang, Feng, et al. "3D printing technologies for electrochemical energy storage." Nano Energy 40 (2017): 418-431.

[6] Sun, Ke, et al. "3D printing of interdigitated Li-Ion microbattery architectures." Advanced Materials 25.33 (2013): 4539-4543.

[7] Wei, Teng-Sing, et al. "3D Printing of Customized Li-Ion Batteries with Thick Electrodes." Advanced Materials 30.16 (2018): 1703027.

[8] Fu, Kun, et al. "Graphene oxide-based electrode inks for 3D-printed lithium-ion batteries." Advanced materials 28.13 (2016): 2587-2594.

[9] Li, Jie, et al. "A hybrid three-dimensionally structured electrode for lithium-ion batteries via 3D printing." Materials & Design119 (2017): 417-424.

[10] Seifert, Tobias, et al. "Additive manufacturing technologies compared: morphology of deposits of silver ink using inkjet and aerosol jet printing." Industrial & Engineering Chemistry Research 54.2 (2015): 769-779.

[11] Hoey, Justin M., et al. "A review on aerosol-based direct-write and its applications for microelectronics." Journal of Nanotechnology 2012 (2012).

[12] Wang, Kan, et al. "Conductive-on-demand: Tailorable polyimide/carbon nanotube nanocomposite thin film by dual-material aerosol jet printing." Carbon 98 (2016): 397-403.

[13] Jabari, Elahe, and Ehsan Toyserkani. "Micro-scale aerosol-jet printing of graphene interconnects." Carbon 91 (2015): 321-329.

[14] Jones, Carissa S., et al. "Aerosol-jet-printed, high-speed, flexible thin-film transistor made using single-walled carbon nanotube solution." Microelectronic Engineering 87.3 (2010): 434-437.

[15] Mahajan, Ankit, C. Daniel Frisbie, and Lorraine F. Francis. "Optimization of aerosol jet printing for high-resolution, high-aspect ratio silver lines." ACS applied materials & interfaces5.11 (2013): 4856-4864.

III. CUSTOMIZABLE NON-PLANAR PRINTING OF LITHIUM-ION BATTERIES

Xiaowei Yu[1], Yangtao Liu[2], Hiep Pham[1], Susmita Sarkar[1], Brandon Ludwig[1], I-Meng Chen[1], Wesley Everhart[3], Jonghyun Park[1], Yan Wang[2] and Heng Pan[1]

[1]Department of Mechanical and Aerospace Engineering,
Missouri University of Science and Technology, Rolla, MO 65409

[2]Department of Mechanical Engineering,
Worcester Polytechnic Institute, Worcester, MA 01609

[3]Honeywell Federal Manufacturing & Technologies LLC,
Kansas City National Security Campus, Kansas City, MO 64147

ABSTRACT

Lithium-ion batteries (LIBs) are widely used in consumer electronics due to the advantages of rechargeability and high energy density. Commercial LIBs are usually fabricated in fixed geometry such as cylinder, coin, and pouch. Nevertheless, with the growing demands on specialized applications such as wearable electronics and on-device power systems, customizable LIBs with an arbitrary geometry on 3D structures need to be developed along with the packaging, integrating, and manufacturing approaches. For such purpose, aerosol printing would be an ideal method due to its unique advantage of flexible working distance, allowing deposition on non-planar substrates with multi-scale surface topologies. This work presents aerosol printing of LiFePO4 (LFP) cathodes and Li4Ti5O12 (LTO) anodes for LIBs. By the printing method, electrodes with an arbitrary geometry, tailorable thickness and on non-planar substrates can be realized. The highest areal capacity achieved by aerosol printed electrodes in this work is ~7.1 mAh/cm2,

which is at least twice of those conventional electrodes. Furthermore, to package the aerosol printed electrodes, 3D printed enclosures are fabricated via fused deposition modeling (FDM) of polyvinylidene fluoride (PVDF). The aerosol printed electrodes packaged in 3D printed enclosures exhibit 78.4% capacity retention after 30 cycles. With the two developed additive manufacturing (AM) processes, customizable LIBs on targeted objects with arbitrary geometry can be realized. As a demonstrating device, non-planar LIB conformably covering the edge of a block with specific capacity of 135 mAh/g is fabricated.

Key words: lithium-ion batteries, additive manufacturing, aerosol printing, non-planar, printed batteries.

1. INTRODUCTION

In the past decades, global communities have spent great efforts in exploiting renewable and sustainable energy resources. As a result, novel energy harvesting and storage devices with advanced materials and architectures have been continuously investigated [1–3]. Lithium-ion batteries (LIBs), as the most developed type of electrochemical energy storage devices, have been widely used in consumer electronics due to the advantages of rechargeability and high energy density [4–6]. Commercial LIBs are usually fabricated in fixed geometry such as cylinder, coin, and pouch with scrolled or layered planar sheets for each component [7].

Nevertheless, LIBs with customizable geometry are desired for specialized applications such as wearable electronics [8,9] and on-device power systems [10,11] for

automobile and aerospace vehicles, For example, LIBs can be made into a watchband to power an electronic watch [12] which eliminates the installation and replacement of coin cell. To meet such demands, irregular, customizable LIBs in arbitrary geometry on 3D structures along with the packaging, integrating and manufacturing approaches need to be developed. So far, the most effective solution to fabricate freeform LIBs is additive manufacturing (AM, popularly known as 3D printing) [13–16]. The on-demand and layer-by-layer manufacturing method has provided the flexibility to accommodate customizable designs of 3D LIBs.

Electrodes are the most essential components of LIBs. Currently reported AM processes for electrodes are mostly based on extrusion printing [17–24], with a few reports on other ink-based printing methods including inkjet printing [25] and aerosol printing [10]. In extrusion printing, active material laden inks are directly deposited and powered by ultra-high air pressure. The materials are extruded into semi-solidified and self-supportive filaments owing to the shear-thinning characteristics of the highly viscous inks. Main advantage of AM processes is the capability of printing electrodes in arbitrary geometry. For example, Lacey et al. and Wang et al. demonstrated 3D printing of mesh and lattice structured electrodes which effectively introduced macro-porosity and facilitated the transportation of lithium ions under high charging/discharging rate [18,23]. The flexibility in printed geometry also enables the fabrication of electrodes with high aspect ratio and high areal capacity, which are usually not processable by conventional slurry-casting method. Sun et al. firstly printed high aspect ratio, multilayer, interdigitated electrodes for micro-LIBs with high energy density and power density [21]. Despite these advantages, in extrusion-printing, composition and rheological behaviors of

inks are demanding due to the requirements in clogging prevention, substrate bonding and shape maintenance [19,20]. Alternatively, aerosol printing processes a wide variety of materials, including polymers [26,27], metallic conductors [28–30], semiconductors [31,32], carbon-based nanomaterials [33,34] and energy materials [3] in laden inks with a wider range of viscosity from 1 cP to 1,000 cP [35,36]. Aerosol printing utilizes moderately pressurized air to nebulize the active materials into aerosol mist and drive the precise material deposition with smallest feature size down to 10 μm [37].

A unique advantage of aerosol printing for the purpose of freeform fabrication is the capability of deposition on non-planar substrates with complex surface topologies such as trenches and wavy structures (tens of micron to millimeter size) due to the flexible working distance of 1-5 mm from the deposition nozzle to the substrate [28,38,39]. The non-planar printing can be further extended to large objects (centimeter size) with 5-axis stage equipped. Such hierarchical non-planar capabilities potentially give rise to building LIBs on complex, multi-scale 3D architectures.

In our previous work, aerosol printing of a collection of materials for cathodes, anodes and current collectors of LIBs were primarily developed [40]. Recently, Deiner et al. fabricated 170 μm thick porous cathode by aerosol printing [10]. Nevertheless, the flexibility in electrode design enabled by aerosol printing with customizable geometry, tailorable thickness and non-planar capability has not yet been demonstrated.

Here we report the fabrication of $LiFePO_4$ (LFP) cathode and $Li_4Ti_5O_{12}$ (LTO) anode for LIBs by aerosol printing. Surface wetting of inks on substrates, size distribution and drying time of the aerosol microdroplets were studied to validate the printing process. The printed cathode and anode both exhibited excellent cycling and rate

performances. By multi-layer printing, thick electrodes with folded, high areal capacity can be realized. The highest areal capacity of 7.1 mAh/cm^2 was achieved by 12-layer electrodes, which is at least twice of those conventional electrodes.

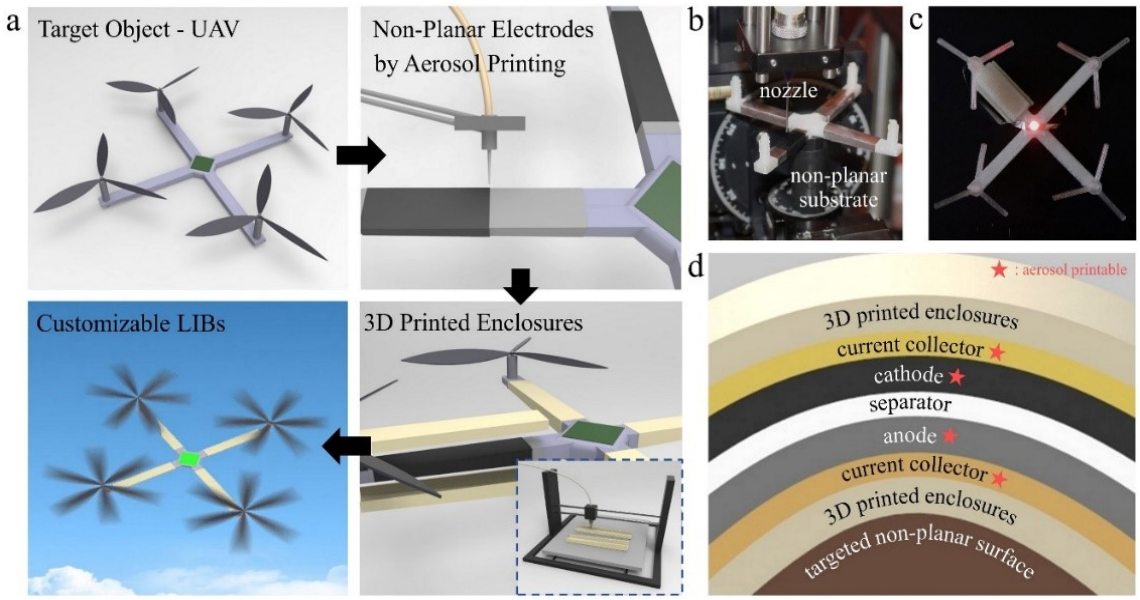

Figure 1. (a) Conceptual illustration of the 3D printing of the customizable non-planar LIBs on the four arms of an unmanned aerial vehicle (UAV). (b) Photograph of aerosol printing of non-planar electrodes on a 5-axis stage. (c) Photograph of customizable non-planar LIB on UVA model lighting up a red LED. (d) Schematic of layered and aerosol printable components in the cross-section of a customizable non-planar LIB.

In spite of the current progresses of electrodes by AM, most of printed electrodes were still tested either in open system [21] or in commercial packages such as coin cells [19,20] and Swagelok cells [41,42]. For the purpose of customizable non-planar LIBs, conformal packaging of the printed electrodes plays an important role in their integration into targeted devices. Developing AM techniques for the packing materials of LIBs is

thus an urgent need [43]. However, challenges exist due to two major concerns: the electrochemical compatibility and air/moisture hermeticity of the printed structures.

In this study, fused deposition modeling (FDM), an easy-accessible, low-cost and high-speed 3D printing technique [44] was utilized to print the packaging enclosures for customizable LIBs. Owing to the known electrochemical stability of polyvinylidene fluoride (PVDF), PVDF filament was chosen as the printable packaging material. PVDF is also lightweight compared to metallic packaging materials which helps reduce the weight ratio of inactive materials in LIBs. The aerosol printed electrodes packaged in the 3D printed enclosures showed 78.4% capacity retention after 30 cycles with nearly full Columbic efficiency.

With the two developed AM processes (aerosol printing of electrodes and FDM of packaging enclosures), customizable LIBs on targeted objects with arbitrary geometry can be realized Figure 1a-c illustrates the concept and fabrication of customizable LIBs with Figure 1d presenting the cross-section of a customizable non-planar LIB with its layered and aerosol printable components. To electrochemically evaluate the customizable LIBs, a non-planar full-cell conformably covering the edge of a block was fabricated with cathode and anode by aerosol printing and 3D printed enclosures. The customizable non-planar full-cell delivered specific capacity of 135 mAh/g, which was only slightly lower than that of the planar one. The proposed manufacturing methods showed the potential for customizable LIBs without geometry-wise limitations to maximize their efficiency for specific devices and applications according to the need of the users.

2. RESULTS AND DISCUSSION

Aerosol printing processes of cathodes and anodes were studied as the first step of the fabrication of LIBs. Taking advantage of the flexible printing process, electrodes in many common forms can be made, such as dish-shaped electrodes for coin cell, square-shaped electrodes for pouch cell and interdigitated electrodes (Figure S1). Schematic illustration of the setup of aerosol printing is shown in Figure 2a. Besides the printing setup, a bottom-view coaxial microscope is equipped to observe the deposited materials on the substrate (Figure 2b). Aerosol printing is capable of processing a variety of materials. For the purpose of printing electrodes for LIBs, the metallic materials for current collectors (gold for cathodes and copper for anodes) as well as four active materials: $LiMn_2O_4$ (LMO) and LFP for cathodes, graphite and LTO for anodes have been developed (Figure 2c).

In this work, LFP and LTO were selected as the active materials for cathode and anode considering their stable electrochemical performances. Pneumatic nebulizers (Figure S3) were used to print the inks of cathode and anode which contained active materials (LFP for cathode and LTO for anode), binder (PVDF), conductive carbon black and N-Methyl-2-Pyrrolidone (NMP) as solvent. In aerosol printing, the inlet gas nebulizes the ink into aerosol mist which contains substantial liquid microdroplets with solvent carrying the particles of loaded materials. The receiving substrates can be either planar or non-planar. When the aerosol microdroplets are being deposited on the substrate, part of the solvent evaporates in the flight. The rest of the solvent gets fully evaporated after the microdroplets reaching the substrate (inset of Figure 2b). After the

deposition of aerosol microdroplets, coalescence of these microdroplets occurs to form the printed feature.

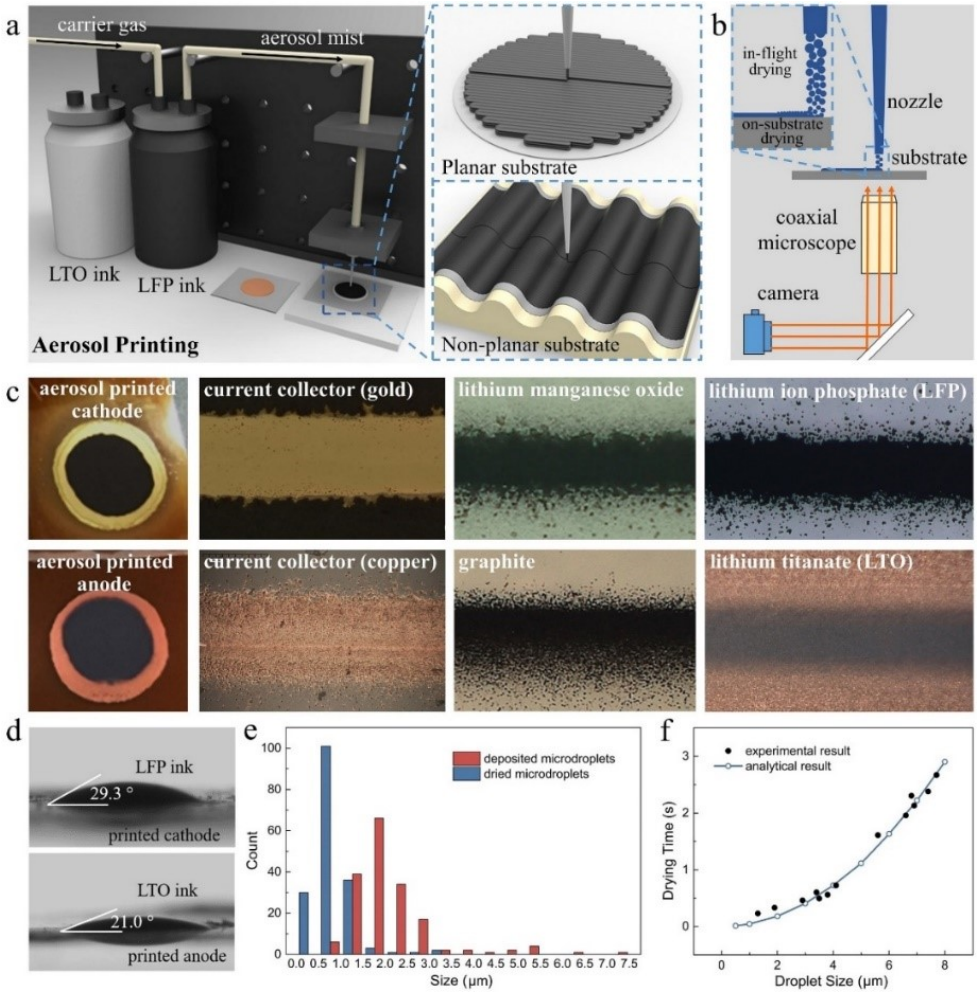

Figure 2. (a) Schematic of aerosol printing process. The zoomed images show deposition on planar and non-planar substrates. (b) Setup of bottom-view coaxial microscope for size distribution and drying time studies. Inset shows the schematic of the in-flight drying and on-substrate drying processes. (c) Photographs of aerosol printed cathode and anode revealing the multi-material processability of aerosol printing in the fabrication of electrodes for LIBs. The microscopic images present the morphology of the aerosol printed lines of current collectors and active materials. (d) Two example images showing the wetting conditions of cathode ink on printed cathode anode ink on printed anode. (e) Size distribution of the deposited and fully dried aerosol microdroplets. (f) Experimental and analytical results of the on-substrate drying time of aerosol microdroplets with varied size.

In multi-layer printing process, besides the initial layer on foil substrate, the ink was also deposited on the previous printed layer. Thus, the wetting behaviors of ink droplet on both foil and electrode were studied by contact angle measurement and compared to that of the pure solvent. Figure 2d shows two examples of the contact angle measurements from cathode ink on printed cathode and anode ink on printed anode. The complete results of contact angle measurement and detailed analysis can be found in Figure S2. Overall, both cathode and anode inks showed good wetting on foils and printed electrodes. This indicated the microdroplets landed on substrate would stay and coalesce into as-designed feature in the aerosol printing process. Next, the size distribution of the microdroplets from the aerosol mist was investigated with the cathode ink. From the bottom-view coaxial microscope, the aerosol microdroplets can be observed from the moment when they landed on the substrate. The size of the microdroplets right after deposition was measured and compared to that of the fully dried microdroplets. The results were summarized in the distribution plot in Figure 2e. Aerosol printing seemed to deliver a wide size range of the microdroplets [39]. The size of deposited microdroplets was ranging from 0.8 μm to 7.4 μm and that of the fully dried microdroplets was at 0.3 μm to 3.4 μm, indicating size reduction of more than 50%. Then, the on-substrate drying time of individual microdroplets with varied size was analyzed through the videos taken by the coaxial microscope. An example of the drying process of an aerosol microdroplet after landing on the substrate is presented in Figure S4. The on-substrate drying time versus the size of microdroplets was plotted in Figure 2f. As seen from the result, microdroplets smaller than 5 μm (which are the majority of the microdroplets as seen from the size distribution plot in Figure 2e) were dried within

one second. The larger microdroplets took significantly longer period to get dried. A kinetic mass transportation model [30,45] was used to analytically study the drying time. The details of the analytical model can be found in Equation S1-S3. The analytical results showed that the drying time increased in a second order polynomial trend with the increased size of microdroplets. The obtained curve (blue line in Figure 2f) fitted the experimental results well.

To verify the electrochemical functionality of the aerosol printed electrodes, they were firstly printed into dish-shaped electrodes and tested in coin cells. LFP cathode and LTO anode were prepared with printing speed of 1 mm/s and line offset of 0.1 mm. By printing 2-4 layers, electrodes with areal loading in the common range (10-20 mg/cm^2) of the conventional electrodes are obtainable. By further increasing the printed layer numbers, aerosol printed thick electrodes can be realized.

Figure 3a displays the top-view scanning electron microscopy (SEM) image of the printed LFP cathode. The 2-layer LFP had thickness of ~43 μm and the porosity was estimated to be ~29%. Details of the porosity calculation of the electrodes can be found in Table S1. The aerosol printed LFP cathode were assembled countering Li foils as half-cells to evaluate their electrochemical performances. Cycling performance and rate performance of LFP cathode are shown in Figure 3b and c. The cycle test showed that the LFP electrodes had capacity of ~140 mAh/g at 0.5 C without visible capacity fade in 30 cycles. The rate test was carried out from low charging/discharging rate to high rate. As seen from the result, at low rate (0.1 C and 0.2 C), capacity of the LFP cathode was near to the theoretical value (~170 mAh/g), indicating the active materials were effectively utilized. With increased rate, capacity was gradually decreased due to the insufficient

transportation of lithium ions. SEM image of printed LTO anode is given in Figure 3d. The 2-layer LTO had thickness of ~60 μm and estimated porosity of ~46%. Cycling performance and rate performance of LTO anode are shown in Figure 3e and f. From the results of cycle test (0.5 C), after stabilization, LTO anode exhibited stable capacity at ~143 mAh/g throughout the 30 cycles. As for the rate performance of LTO anode, the specific capacity degraded less than 50% from 171 mAh/g to 91 mAh/g when the rate increased 50 times from 0.1 C to 5C.

To investigate the capability of aerosol printing in the fabrication of thick electrodes, LFP cathodes with different thickness were prepared by varying the printed layer numbers. To print thick electrodes, an optional in-situ laser as heating source was introduced to facilitate the evaporation of solvent and deposition of printed materials without damaging the material properties of the deposition (as verified by X-ray diffraction analysis in Figure S5). Figure 3g showed a series of cross-section SEM images of the LFP cathodes with 2, 4, 8 and 12 printed layers, demonstrating the vertical building of active materials by multi-layer printing. It should be mentioned that the SEM images were taken from mildly compressed electrodes. The compression was introduced to mimic the compression experienced during final cell assembly and to increase the compactness of printed electrodes. For 8-layer and 12-layer electrodes, compression was also introduced after printing and drying every 4 layers to prevent the delamination of electrode materials. As seen from the SEM images, the aerosol printed thick electrodes was bulky in vertical direction without obvious interfaces between different printed laminations, which was beneficial to the vertical transportation of electrons. The thickness of the printed LFP cathodes was increased linearly as plotted in Figure 3h. The

thickness values of 8-layer and 12-layer electrodes were 167.6±4.7 and 244.9±6.4 μm. Electrodes with such thickness are usually beyond the processability of conventional slurry-casting method. The areal mass loading was also increased in linear trend (Figure 3h) with the highest loading of ~52.5 mg/cm2 by 12-layer printing. The microstructures of the printed materials did not seem to change for the aerosol printed thick electrodes (Figure S6).

The LFP cathodes with varied printed layer numbers were electrochemically tested countering Li foils as half-cells at charging/discharging rate of 0.1 C. The areal capacity of these LFP cathodes plotted in Figure 3i was converted from their specific capacity and areal loading. The specific capacity of LFP cathodes was very constant for 2-layer, 4-layer and 8-layer LFP at near theoretical value (~170 mAh/g), suggesting the nearly full utilization of active materials. As a result, in Figure 3i, their areal capacity was growing in folds. However, areal capacity of 12-layer LFP only showed slight increase as compared to 8-layer electrode because the specific capacity of the 12-layer LFP was dropped to ~136 mAh/g. The drop in capacity presumably resulted from the insufficient transportation of lithium ions along the vertical direction. Here the pristine LFP cathodes by aerosol printing were found to deliver a highest areal capacity of 7.1 mAh/cm^2. In order to realize the full utilization of active materials in the aerosol printed thick electrodes, macro-scale porosity by patterning of structures or micro-scale porosity by assembly/organization of active materials are usually needed to ensure sufficient diffusion of lithium ions. Both methods could be considered to further improve the performance of the aerosol printed thick electrodes.

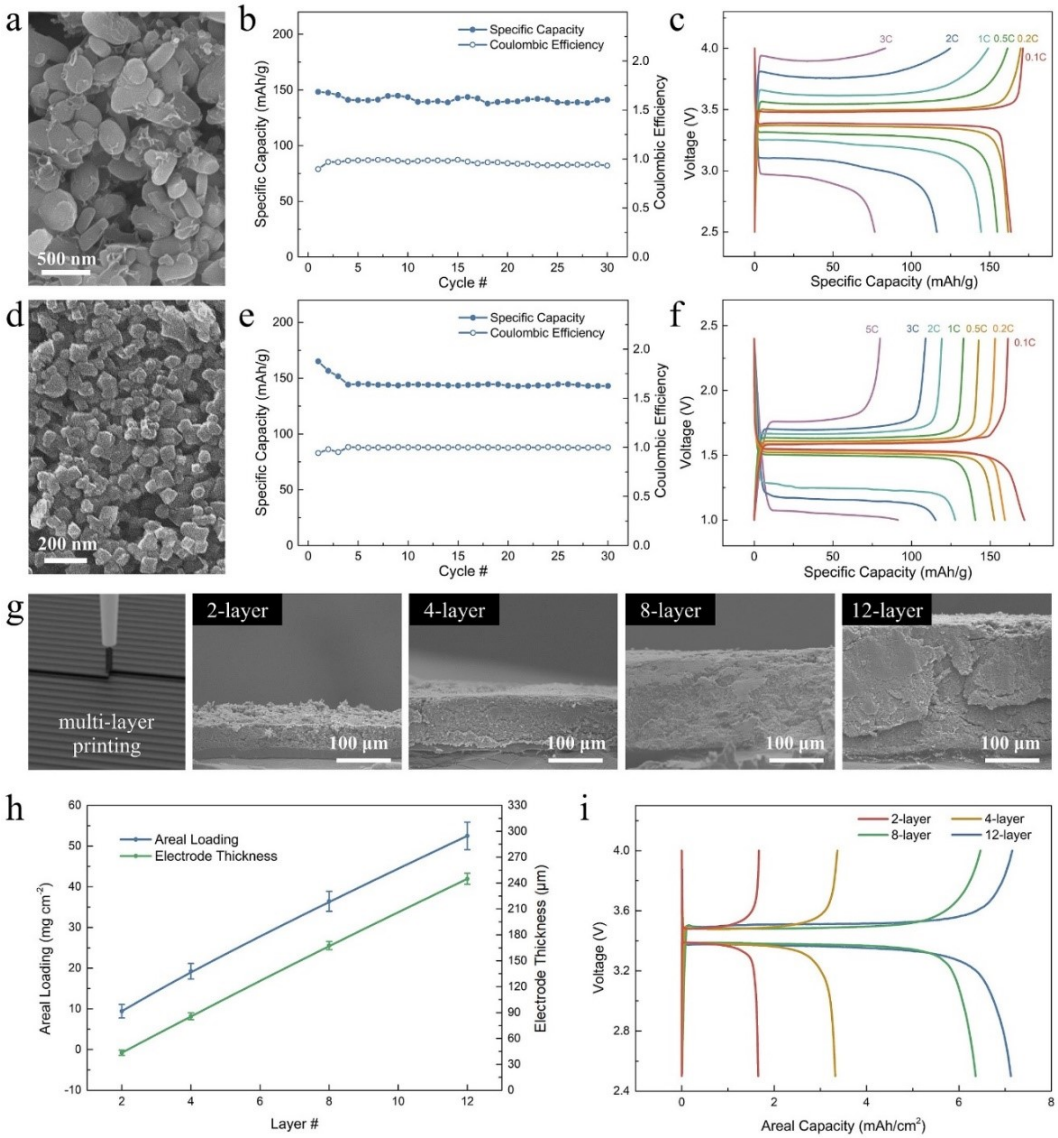

Figure 3. (a) Top-view SEM images of the aerosol printed LFP cathode. (b) Cycling performance at 0.5 C and (c) rate performance of the LFP electrode. (d) Top-view SEM images of the aerosol printed LTO anode. (e) Cycling performance at 0.5 C and (f) rate performance of the LTO anode. (g) Schematic of multi-layer printing and a series of SEM images of the LFP cathode with increased printing layer number. (h) Areal loading and electrode thickness of LFP cathode with various printing layer number. (i) Charging and discharging profiles of LFP cathode with various printing layer number.

To fabricate the packaging for the aerosol printed electrodes, PVDF filaments were printed by FDM into as-designed 3D enclosures. As mentioned above, the two main

requirements for the packaging materials are hermeticity and electrochemical stability. To ensure hermeticity, one of the necessary conditions is that the enclosures must be densely printed. Two key printing parameters, material feed rate and printing speed were evaluated as depicted in Figure S5. As a result, material feed rate of 100% and printing speed of 20 mm/s were found to provide optimized density and processing rate, so they were used in the following FDM process.

To experimentally evaluate the electrochemical compatibility of FDM-PVDF and sealing materials such as polydimethylsiloxane (PDMS), epoxy, and UV-curable epoxy (see supporting information) [44–49], they were assembled into coin cells to evaluate the symmetricity of first charging/discharging cycle (Figure S6). The results in Table S2 indicated that FDM-PVDF, PDMS and UV-curable epoxy were providing good electrochemical inertness and could be potentially used in the packaging of customizable LIBs.

Before the fabrication of customizable LIBs, the functionality of the 3D printed enclosures as packaging for LIBs was evaluated with planar electrodes. Figure 4a showed the design and assembly processes of the 3D printed enclosures for regular dish-shaped electrodes. The two-piece enclosures were printed with a chamber for the assembly of cathode, separator and anode (or Li foil). After the assembly process, the enclosures were mechanically fixed with screws and nuts. They also helped to press the cathode, separator and anode layers so that the transporting length of lithium ion was minimized during the charging/discharging processes. Sealing materials were then injected into the designed groove with needle and syringe. After curing the sealing materials, the enclosure cells

were ready to use. In Figure 4b, the photographs of an enclosure half-cell lighting the green LED demonstrated the electrochemical functionality.

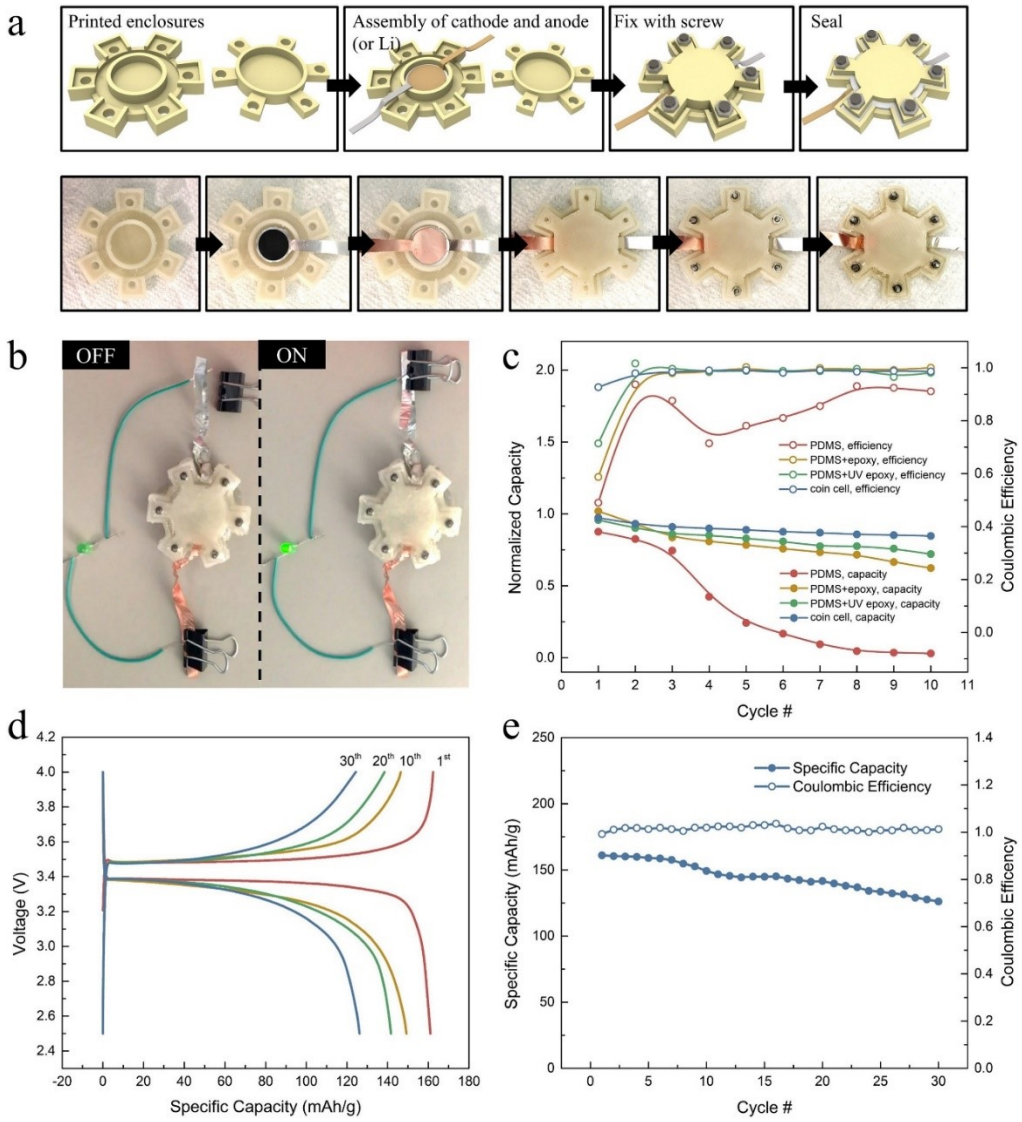

Figure 4. (a) Schematics and photographs of the design and assembly processes of the planar enclosure cell. (b) Photographs of the enclosure half-cell lighting a green LED. (c) Cycling performance and Columbic efficiency of the enclosure cells with different sealing materials (UV-epoxy refers to UV-curable epoxy) in 10 cycles. (d) Charging and discharging profiles of enclosure cell with aerosol printed LFP cathode. (e) Specific capacity and Coulombic efficiency of enclosure cell with aerosol printed LFP cathode in 30 cycles.

Standard LMO cathodes were firstly used for preliminary evaluation of the performance of enclosure cells with different sealing materials. The normalized capacity and Coulombic efficiency in 10 cycles of enclosure cells with different sealing materials (PDMS only, PDMS with epoxy and PDMS with UV-curable epoxy) compared to coin cell were plotted in Figure 4c. The enclosure cell sealed only by PDMS showed severe degradation in capacity after merely 3 cycles. The Coulombic efficiency was also dropped to below 90%, which revealed the energy loss. The degraded capacity could be attributed to the oxidation of Li foil and the damage caused to active materials with the attack of air leakage. With additional sealing with either epoxy or UV-curable epoxy, the cycling performance of the enclosure cells was significantly improved. UV-curable epoxy introduced more improvement to both capacity and Coulombic efficiency with the enclosure cell exhibiting capacity retention of ~75% after 10 cycles. From the investigation of different sealing materials, PDMS and UV-curable epoxy were found to give the result closest to coin cells, so these two sealing materials were chosen for the following studies.

Next, 3D printed enclosures with the same design were used to package the dish-shaped aerosol printed LFP cathodes. The charging and discharging profiles and the cycling performance of the LFP cathodes in 3D printed enclosures tested with rate of 0.1 C were plotted in Figure 4d and e. The enclosure cell exhibited specific capacity of 161.0 and 126.2 mAh/g at 1st cycle and 30th cycle, with capacity retention of 78.4% after 30 cycles. Throughout the 30 cycles, Coulombic efficiency was kept near 100% (Figure 4e) and there was no symptom of side reactions observed in the charging and discharging profiles (Figure 4d). These results primarily proved that aerosol printing of electrodes and

FDM of packaging enclosures provided LIBs with acceptable electrochemical performances.

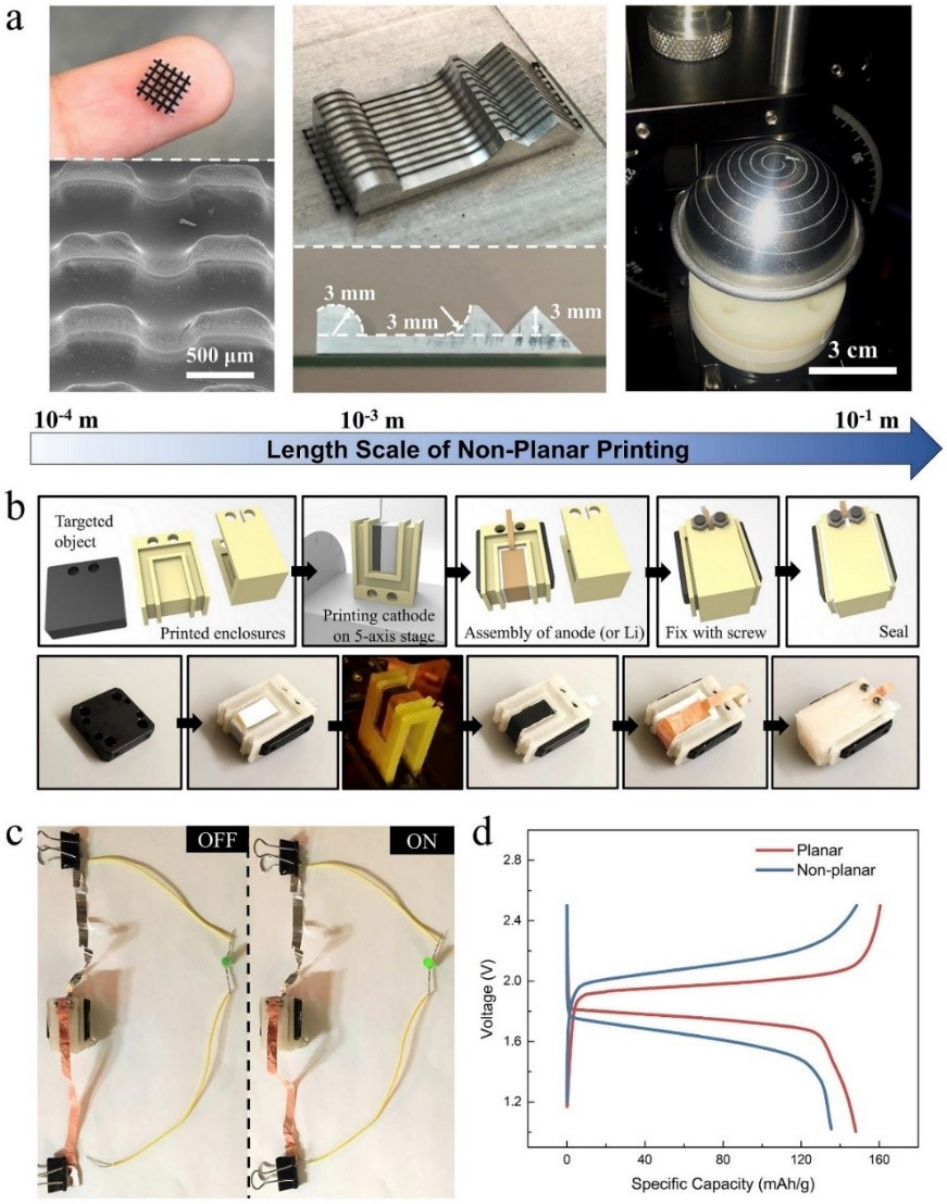

Figure 5. (a) Non-planar capabilities of aerosol printing in different length scale. (b) Schematics and photographs of the design and assembly processes of the customizable non-planar LIB. (c) Photographs of the non-planar enclosure half-cell lighting a green LED. (d) Charging and discharging profiles of the planar and nonplanar enclosure full-cells.

After the evaluation of aerosol printing of electrodes and FDM of packaging enclosures, these two AM techniques were utilized to fabricate customizable non-planar LIBs. Aerosol printing is suitable for the fabrication of electrodes on non-planar substrates due to its hierarchical non-planar capabilities. Figure 5a shows three examples of aerosol printing on 3D non-planar surfaces in different length scale. In the left-side photograph and SEM image, the printed LFP pattern on a fingertip-sized (5 mm) polymer piece with 3D-structured array of 300 μm deep and 500 μm wide squares is displayed. The central photographs show the printing on an aluminum piece with different surface topologies in depth of 3 mm. These two examples both demonstrate the non-planar capability from the flexible printing distance of aerosol printing without using the 5-axis stage. Furthermore, with the assist of 5-axis stage (Figure S7), aerosol can be used to print patterned structures on non-planar substrates in centimeter size such as the hemispherical piece in the right-side photograph in Figure 5a.

Here, the secondary non-planar capability of aerosol printing with 5-axis stage was utilized to fabricate the non-planar LIBs mounted on the edge of a block as the targeted object. The design and assembly processes of the non-planar LIBs was shown in Figure 5b. The assembly process was similar to that for the planar ones except that the cathode ink was printed with 5-axis stage into the non-planar electrodes. The photographs of the non-planar enclosure half-cell lighting up a green LED in Figure 5c preliminarily demonstrated the electrochemical functionality. The charging and discharging profiles of the planar and non-planar enclosure full-cells with aerosol printed LFP cathode and LTO anode were plotted in Figure 5d. As shown, the planar and non-planar enclosure full-cell exhibited specific capacity of 148 mAh/g and 135 mAh/g, respectively.

The decreased capacity could result from the non-uniform pressure in the non-planar enclosure full-cell, leading to the long transporting length of lithium ions and partially insufficient utilization of active materials. In addition, compared to planar enclosure full-cell, the non-planar cell had higher charging voltage and lower discharging voltage. Also, the charging and discharging plateaus were less flat. These two phenomena came from the high internal impedance due to the weak mechanical integrity among the constituents. In spite of this, the non-planar enclosure cell functioned well with only slight loss of capacity as compared to the planar one.

3. CONCLUSIONS

In conclusion, aerosol printing of electrodes and FDM of packaging enclosures have provided potential route to the fabrication of customizable non-planar LIBs. The aerosol printed LFP cathode and LTO anode exhibited high specific capacity with excellent cycling and rate performance. Thick electrodes were achievable by multi-layer aerosol printing with highest areal capacity of 7.1 mAh/cm^2. 3D printed PVDF enclosures were utilized for the conformal packaging strategy of the customizable non-planar electrodes. The aerosol printed LFP cathode packaged in the 3D printed enclosures showed capacity retention of 78.4% after 30 cycles. Lastly as a demonstrating device, the customizable non-planar LIB on the edge of a block was fabricated with specific capacity of 135 mAh/g.

This work demonstrated the feasibly of customizable non-planar LIBs by AM techniques. However, further improvement could be made in several aspects. (1) Macro-

scale porosity by patterning of structures or micro-scale porosity by assembly or organization of active materials need to be introduced into current aerosol printing method in order to shorten the diffusion length of lithium ions in the aerosol printed thick electrodes to realize higher energy density and power density. (2) Printable, hermetic, and mechanically durable packaging enclosure/encapsulation has to be realized for the long-term usage of customizable LIBs. The packaging enclosure/encapsulation majorly functions as the barrier to prevent diffusion of air/moisture. Besides, the high-quality enclosure/encapsulation and the good bonding between the encapsulation/enclosure and battery components (current collectors/electrodes) would help in the uniform distribution of strain so that the battery would be stronger under stress/deformation. To further improve the mechanical flexibility of the printed LIBs, some flexible materials [52,53] and designs in geometry [47,54] could be incorporated. (3) For fully-printed LIBs, printing of separators and electrolytes [55,56] need to be incorporated to realize a hybrid printing platform. For the fabrication of current collectors, printing and in-situ sintering [57-61] of metallic materials would be desired. All the printed components need to provide customizability as well as comparable electrochemical functionality to those components by conventional manufacturing methods in current LIB industry.

4. EXPERIMENTAL SECTION

Electrode ink preparation: Cathode ink was prepared by mixing LFP nanoparticles (Hydro-Québec), carbon black (Super C45, Timcal), and PVDF (MTI) in NMP (Sigma-Aldrich). PVDF was firstly dissolved in NMP before the addition of other solids. Then,

the dry powders were mixed together with the solution and additional solvent by high-speed mixer (FlackTek). The weight ratio of LFP/carbon black/PVDF was 75/20/5. Similarly, anode ink was made by mixing LTO nanoparticles (Sigma-Aldrich) with same additives in NMP with weight ratio of 90/5/5 (LTO/carbon black/PVDF). The total solid concentration in the ink was controlled at 15 wt%.

Aerosol printing of electrodes: After preparation of the electrode ink, it was loaded in the pneumatic nebulizer (CH technologies) and printed with gas flow rate of 0.4-0.5 LPM. In the nebulizer, aerosol mists containing the active materials and additives were generated and delivered to the printing head by the carrier gas. The receiving substrate can be mounted on motorized XY-axis stage or 5-axis stage depending on the targeted geometry. An in-situ 808 nm CW fiber laser (CNI laser) was optionally used at 1.3 W in the printing of thick electrodes to facilitate solidification. A bottom-view coaxial microscope (Thorlabs) was set up to observe the deposited materials. The whole printing process was performed in clean room. After printing, the electrodes were baked in vacuum oven at 80 °C for 8 hours to ensure the complete removal of solvent and to activate the binder.

FDM of packaging materials: PVDF filaments (Fluorinar Kynar, Nile Polymers) were used as the thermoplastic polymer in the FDM process (Monoprice Maker Select) as the packaging materials for customizable LIBs. The PVDF enclosures were printed by with speed of 20 mm/s, material feed rate of 100%, and infilling rate of 100%. The deposition temperature and substrate temperature were 250 °C and 105 °C respectively. Due to the high thermal expansion coefficient of PVDF, warping could occur in the FDM process. To prevent that, raft structures were printed as the bottom support. To print the

overhanging structures in the enclosures for non-planar LIBs, supporting structures were generated. After printing, raft structures and supporting structures were thoroughly removed and the enclosure pieces were cleaned with DI water, acetone and ethanol, then completely dried in vacuum oven before the assembly of LIBs.

Assembly of LIBs: The printed electrodes were firstly characterized in CR2032 coin cell with Celgard separator and liquid electrolyte 1 M $LiFP_6$ in EC:DMC 1:1 (Sigma-Aldrich). Li foil was used as the counter electrode for electrochemical testing of half-cells. To assembly the LIBs with printed packaging enclosures, two-part enclosures with designed trench were firstly mechanically fixed by screws and nuts. The trench was then filled by different sealing materials. After curing of sealing materials the enclosure cells were ready to use. All the assembly processes were conducted in an argon-filled glove box (Mbraun) with oxygen and moisture content of <0.5 ppm.

Characterizations: Morphology of the printed materials was examined by an optical digital microscope (Hirox KH-8700). Microstructures of the printed materials were observed by SEM (Hitachi S-4700). X-ray diffraction analysis was performed by a multi-purpose diffractometer (PANalytical XPert Pro). The galvanostatic charging/discharging testing of the enclosure cells was performed in ambient environment with Arbin BT2043 or IVIUMnSTAT battery testing station.

ACKNOWLEDGEMENT

X.Y. and Y.L. contributed equally to this work. The authors would like to thank Dr. Eric Bohannan and Dr. Clarissa Wisner for their help in material characterizations.

SUPPORTING INFORMATION

1. CUSTOMIZABLE GEOMETRY OF AEROSOL PRINTED ELECTRODES

By aerosol printing, the geometry of the electrodes for LIBs is customizable according to practical applications. Below are some electrodes as examples in common forms fabricated by aerosol printing. The current collectors interdigitated electrodes were fabricated by printing cathode and anode inks on top of aerosol printed gold current collectors. Fine printed lines can be obtained by printing at a high speed.

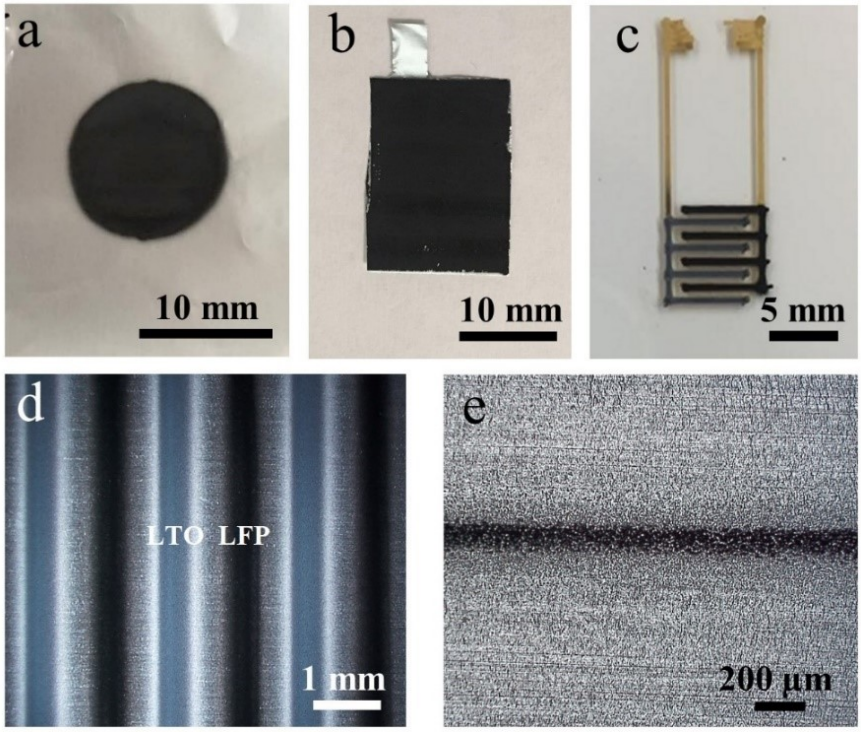

Figure S1: Electrodes in different forms by aerosol printing: (a) Dish-shaped electrode for coin cell, (b) square-shaped electrode for pouch cell, and (c) interdigitated electrodes with aerosol printed LFP cathode and LTO anode. (d) Optical microscopic image of aerosol printed LFP/LTO interdigitated structure. (e) Optical microscopic image of 120 µm wide LFP line printed with a speed of 5 mm/s.

2. WETTING OF CATHODE (LFP) AND ANODE (LTO) INKS

Figure S2 summarizes the results of contact angle measurements which reveal the wetting conditions of the inks on substrates. The droplet of pure NMP solvent on Al foil showed contact angle of 42˚which indicated good wetting condition. The loading of LFP did not seem to alter the wetting behavior on Al foil. However, NMP on the printed cathode showed much smaller contact angle. As for the droplet of cathode ink on printed cathode, the laden particles held the solvent molecules around, so the contact angle was increased.

Similar wetting conditions of anode (LTO) ink on Cu foil and printed anode compared to NMP solvent were observed. The wetting conditions of NMP and anode ink on Cu foil were almost the same. NMP on printed anode had much smaller contact angle, which could be attributed to the diffusion of NMP molecules inside the anode. LTO ink had increased contact angle, but the increase was not as significant as LFP ink on cathode. The less increased contact angle might be because the particle size of LTO is much smaller than LFP. The particles themselves would have a higher chance to fill inside the porosity so they could not hold the solvent molecules that well as the LFP particles.

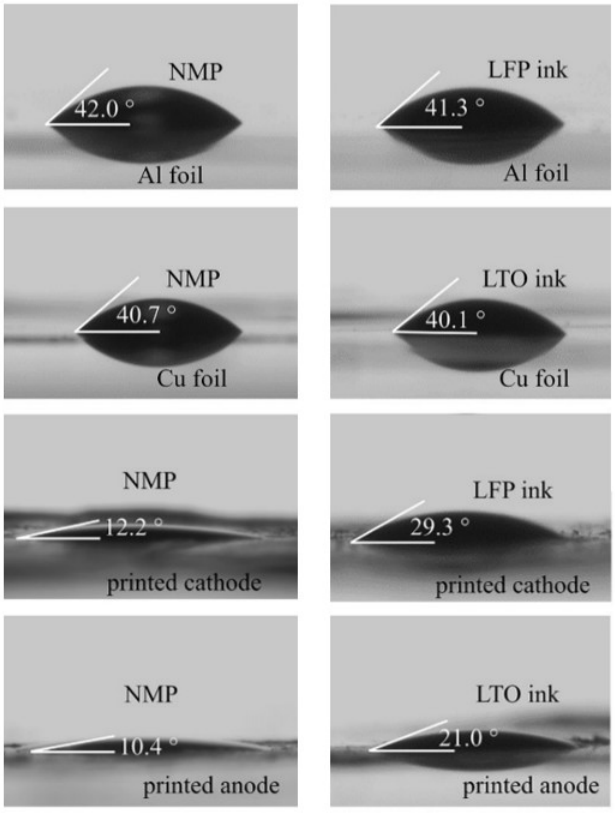

Figure S2: Images of droplet of NMP, LFP on Al foil and printed anode, and NMP, LTO ink on Cu foil and printed anode.

3. WORKING MECHANISM OF COLLISON NEBULIZER

The high-speed inlet gas flows through the small orifice of the nebulizer and produces the jet carrying the ink. The ink hits the jar and break into smaller droplets. Those relatively big liquid droplets flow back to the ink reservoir. Smaller microdroplets are carried by the gas in the aerosol mist and delivered to the deposition nozzle.

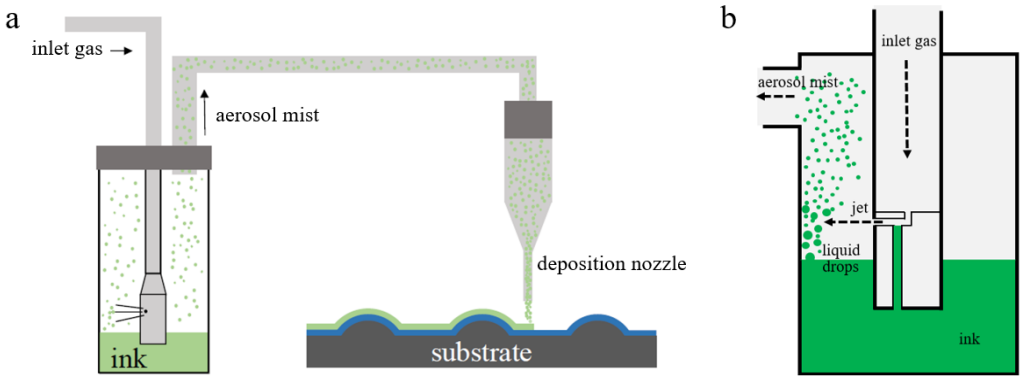

Figure S3: Schematics of working mechanism of Collison nebulizer: (a) The nebulization and deposition process. (b) Generation of aerosol mist inside the Collison nebulizer.

4. MEASUREMENT OF DRYING TIME OF AEROSOL MICRODROPLETS

The drying time of aerosol microdroplets was analyzed through videos taken by the bottom-view coaxial microscope in the printer. Here an example of the drying process of an aerosol microdroplet is given. The size of the microdroplet was gradually decreased with time going. When the size became stable the microdroplet was considered fully dried. The 6.9 μm microdroplet was dried in 2.1 s.

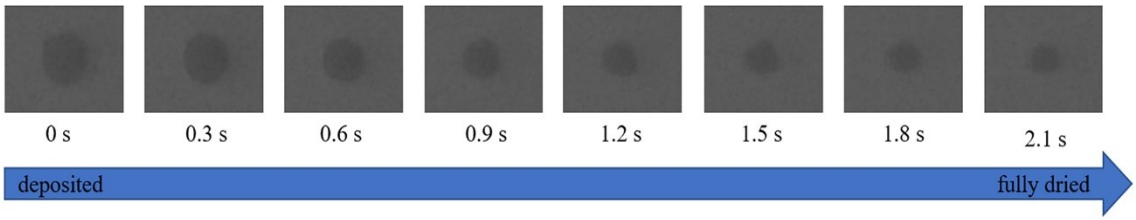

Figure S4: A series of images showing the drying process of an aerosol microdroplet with initial size of 6.9 μm.

5. ANALYTIAL MODEL OF THE DRYING OF AEROSOL MICRODROPLETS

To analytically verify the experimental results of the drying time of aerosol microdroplets, a kinetic mass transportation model [28,43] was used to estimate the drying time. In this model, the rate of mass loss of the microdroplets is given by

$$\frac{dm}{dt} = -4\pi RD\Delta c f(\theta) \tag{S1}$$

where m and t are mass and time. R is the radius of the microdroplet. D refers to the diffusion coefficient and $\Delta c = c_s - c_\infty$ is the difference between the vapor concentration at the surface of microdroplet and the ambient value (assumed to be 0). The surface vapor concentration c_s is calculated by

$$c_s = \frac{MP_v}{RT} \tag{S2}$$

where M, P_v, R and T refer to the molar mass, saturated vapor pressure, universal gas constant and temperature, respectively.

An additional function f(θ) to correct the effect of microdroplets on the substrate is introduced based on the contact angle θ. For $10° < \theta < 180°$,

$$f(\theta) = 0.00008957 + 0.6333\theta - 0.088780\theta^3 + 0.01033\theta^4 \tag{S3}$$

where θ is converted into radian.

Considering the solid particles loaded in the microdroplets, in the calculation, a mass loss of 80% is considered as fully dried.

6. ESTIMATION OF POROSITY FOR AEROSOL PRINTED ELECTRODES

Porosity ϕ of the aerosol printed electrodes was calculated by the following equation:

$$\phi = \frac{V_{bulk} - V_{particle}}{V_{bulk}} = \frac{\frac{1}{\rho_{bulk}} - \frac{1}{\rho_{particle}}}{\frac{1}{\rho_{bulk}}} = 1 - \frac{\rho_{bulk}}{\rho_{particle}} \quad \text{(S4)}$$

where V_{bulk} and $V_{particle}$ refer to the total volume of the bulk electrode and volume of all the three types of particles (active material, binder and carbon black).

Bulk density of the electrode ρ_{bulk} can be calculated from the thickness (T) and areal loading (L) of the electrode by

$$\rho_{bulk} = \frac{L}{T} \quad \text{(S5)}$$

Particle density $\rho_{particle}$ refers to the overall density of the electrode materials counting the weight percent of the three types of particles (active material, binder and carbon black) in the electrode. $\rho_{particle}$ can be calculated based on the true density (D) and weight percent (W) of each material. Subscripts a, b and c in the equation below refer to active materials, binder (PVDF) and carbon black.

$$\rho_{particle} = \frac{1}{\left(\frac{W_a}{D_a} + \frac{W_b}{D_b} + \frac{W_c}{D_c}\right)} \quad \text{(S6)}$$

The data and obtained results of the estimated porosity of aerosol printed electrodes obtained from the calculation above are summarized in Table S1.

Table S1. Data for porosity estimation.

	material	true density (g/cm^3)	weight percent (%)	particle density (g/cm^3)	layer #	thickness (μm)	areal loading (mg/cm^2)	bulk density (g/cm^3)	porosity
cathode	LFP	3.6	75	3.074	2-layer	43.39	9.43	2.173	29.3%
					4-layer	85.77	19.02	2.218	27.9%
	PVDF	1.78	5		8-layer	167.61	36.42	2.173	29.3%
	Carbon	2.25	20		12-layer	244.90	52.50	2.144	30.3%
anode	LTO	3.5	90	3.253	2-layer	60.06	10.52	1.752	46.1%
	PVDF	1.78	5						
	Carbon	2.25	5						

7. THICK ELECTRODES BY MULTI-LAYER PRINTING

In multi-layer printing process, the previous printed layer needs to be dried to certain extent so the subsequent printed materials can be supported. However, in some cases, when too many layers are printed (so the solvent amount get accumulated with fixed surface area of evaporation), or the printing area is too small (so the time period between each layer is too short to allow sufficient drying), extra heating source might be considered to facilitate the evaporation of solvent and solidification of printed materials. This can be usually done by heating up the substrate for regular materials. However, the active materials for LIBs are sensitive to heat under ambient environment that they might be oxidized, and the crystalline structures could be altered. Here we introduced an in-situ 808 nm CW laser as an option to locally heat up the deposition, so the heat is minimized and the damage from the introduced heat to the active materials can be avoided. For inks with different amount of solvent, the power of laser can be adjusted accordingly. Here we

found a laser power of 1.3 W was sufficient to evaporate the solvent during the aerosol printing of thick electrodes.

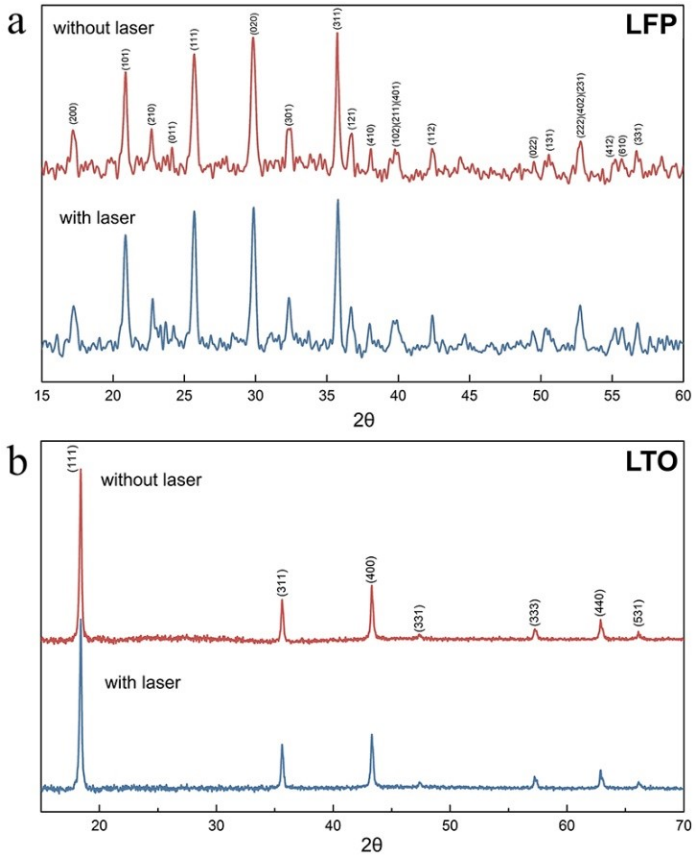

Figure S5: XRD patterns of the (a) cathode and (b) anode printed without and with in-situ laser.

In order to study the material properties of the LFP cathode and LTO anode printed with and without laser, XRD analysis was used to evaluate their crystalline structures. In Figure S5, the XRD patterns of LFP and LTO printed with and without in-situ laser (1.3 W) were compared. The results revealed that the crystalline structures were not affected by the introduction of laser.

8. MICROSTRUCTURES OF THE LFP CATHODES WITH PRINTING LAYERS

To compare the microstructures of the LFP cathodes with increased printed layer number, the 2-layer and 12-layer LFP cathodes were further examined by cross-section SEM with higher magnification. Below are the zoomed-in cross-section SEM images taken at the top side of the samples. From the images, there was no obvious change observed in the microstructures of the printed LFP cathodes with increased printed layer number.

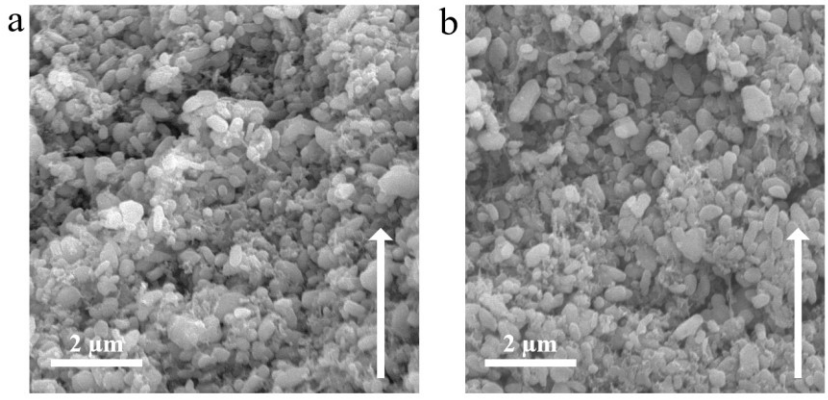

Figure S6: Zoomed-in cross-section SEM images of (a) 2-layer and (b) 12-layer LFP cathodes. The arrows present the vertical direction of thickness growing in the multi-layer printing process.

9. OPTIMIZED PROCESS PARAMETERS OF FDM

To make sure the enclosure pieces are densely printed, two key printing parameters in the FDM process, material feed rate and printing speed were investigated.

Figure S7a shows the results by varying material feed rate with the insets of the photographs of printed pieces at corresponding feed rate. In this study printing speed was fixed at 20 mm/s. When the feed rate was at 20% the printed piece was loose with poor integrity in geometry. When the feed rate reached 40% the density of the printed piece was near to the theoretical density. When the material feed rate reached 100%, the printed piece looked solid and of high quality. Despite the weight is a bit higher than the theoretical weight the geometry was in well accordance with the design.

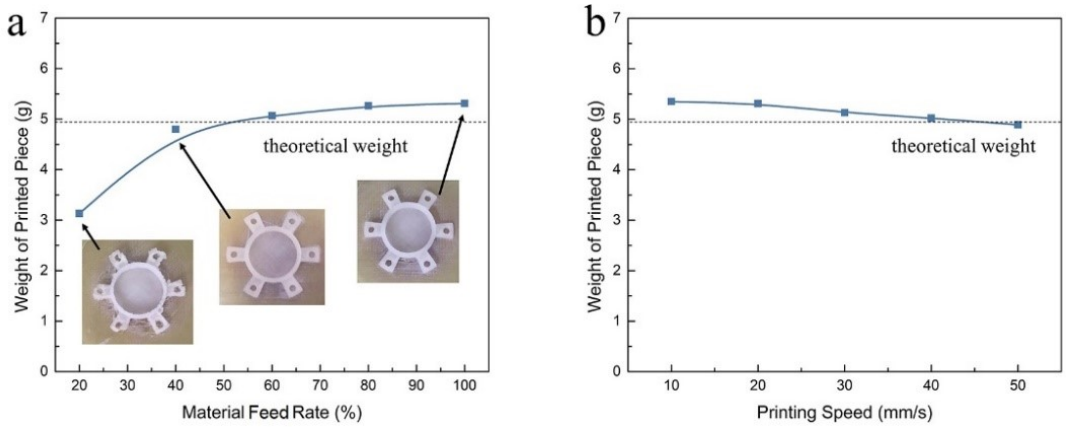

Figure S7: (a) Effect of material feed rate on the weight of printed piece. (b) Effect of printing speed on the weight of printed piece.

Figure S7b plots the results with varied printing speed and fixed feed rate at 100%. The higher printing speed leaded to lower weight but the influence was not as significant as the feed rate. Considering both quality of printed piece and the fabrication speed, material feed rate of 100% and printing speed of 20 mm/s were chosen as the optimized parameters in the FDM process of the PVDF enclosures.

10. ELECTROCHEMICAL COMPATIBILITY OF SEALING MATERIALS

The electrochemical compatibility of the packaging and sealing materials was firstly reviewed with relevant literatures. The powder-based PVDF is widely used in LIB industry as the binding material. However, the PVDF filaments could have printing-assistive additives that has unknown effect on the charging and discharging processes. In literatures, PVDF by FDM is mostly used in piezoelectric purposes, and is not found in the energy-related applications. PDMS is reported being used in stretchable LIBs [46-47], gel-polymer electrolyte [48] and packaging materials for flexible LIBs [49]. Various epoxy materials have been studied in terms of chemical compatibility with electrolyte but electrochemical compatibility is not found [50]. UV-curable epoxy is found as sealing materials for micro-battery [51].

Table S2. Data for porosity calculation.

Materials	First cycle symmetricity/efficiency (charge/discharge)
FDM-PVDF	94.0%
PDMS	98.5%
Epoxy	71.4%
UV-epoxy	90.5%

Furthermore, we experimentally studied the electrochemical compatibility. These materials were assembled into coin cells with standard LMO cathodes countering Li foils (Figure S8) to evaluate the symmetricity (efficiency) of first charging/discharging cycle. The results in Table S2 showed that overall the packaging and sealing materials did not severely affect the charging and discharging process. Among these materials, FDM-PVDF, PDMS and UV-curable epoxy showed relatively better first cycle symmetricity.

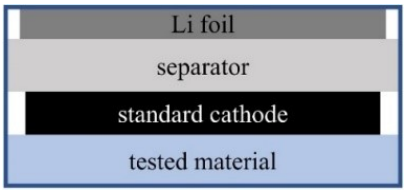

Figure S8: Schematic of the standard cell for electrochemical compatibility testing.

11. PHOTOGRAPH OF 5-AXIS STAGE

The 5-axis stage is capable of motion in x, y, z, x-rotation, and y-rotation.

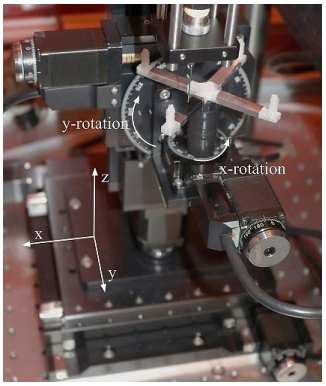

Figure S9: Photograph of 5-axis stage.

REFERENCES

[1] B. Diouf, R. Pode, *Renew. Energy* **2015**, *76*, 375.

[2] D. Larcher, J. Tarascon, *Nat. Chem.* **2014**, *7*, 19.

[3] L. J. Deiner, T. L. Reitz, *Adv. Eng. Mater.* **2017**, *19*, 1600878.

[4] Y. Hu, X. Sun, *J. Mater. Chem. A* **2014**, *2*, 10712.

[5] N. Nitta, F. Wu, J. Lee, G. Yushin, *Mater. Today* **2015**, *18*, 252.

[6] B. Ludwig, Z. Zheng, W. Shou, Y. Wang, H. Pan, *Sci. Rep.* **2016**, *6*, 23150.

[7] L.H. Saw, Y. Ye, A. A. O. Tay, *J. Cleaner Prod.* **2016**, *113*, 1032.

[8] Y. Wang, C. Chen, H. Xie, T. Gao, Y. Yao, G. Pastel, X. Han, Y. Li, J. Zhao, K. K. Fu, L. Hu, *Adv. Funct. Mater.* **2017**, *27*, 1703140.

[9] J. Kim, R. Kumar, A. J. Bandodkar, J. Wang, *Adv. Electron. Mater.* **2017**, *3*, 1600260.

[10] L. J. Deiner, T. Jenkins, A. Powell, T. Howell, M. Rottmayer, *Adv. Eng. Mater.* **2019**, *21*, 1801281.

[11] F. Zhang, M. Wei, V. V. Viswanathan, B. Swart, Y. Shao, G. Wu, C. Zhou, *Nano Energy* **2017**, *40*, 418.

[12] S. Zheng, Z. Wu, F. Zhou, X. Wang, J. Ma, C. Liu, Y. He, X. Bao, *Nano Energy* **2018**, *51*, 613.

[13] M. Wei, F. Zhang, W. Wang, P. Alexandridis, C. Zhou, G. Wu, *J. Power Sources* **2017**, *354*, 134.

[14] C. L. Cobb, C. C. Ho, *Electrochem. Soc. Interface* **2016**, *25*, 75.

[15] S. Ferrari, M. Loveridge, S. D. Beattie, M. Jahn, R. J. Dashwood, R. Bhagat, *J. Power Sources* **2015**, *286*, 25.

[16] P. Chang, H. Mei, S. Zhou, K. G. Dassios, L. Cheng, *J. Mater. Chem. A* **2019**, *7*, 4230.

[17] K. Fu, Y. Wang, C. Yan, Y. Yao, Y. Chen, J. Dai, S. Lacey, Y. Wang, J. Wan, T. Li, Z. Wang, Y. Xu, L. Hu, *Adv. Mater.* **2016**, *28*, 2587.

[18] S. D. Lacey, D. J. Kirsch, Y. Li, J. T. Morgenstern, B. C. Zarket, Y. Yao, J. Dai, L. Q. Garcia, B. Liu, T. Gao, S. Xu, S. R. Raghavan, J. W. Connell, Y. Lin, L. Hu, *Adv. Mater.* **2018**, *30*, 1705651.

[19] J. Li, X. Liang, F. Liou, J. Park, *Sci. Rep.* **2018**, *8*, 1846.

[20] J. Li, M. C. Leu, R. Panat, J. Park, *Mater. Des.* **2017**, *119*, 417.

[21] K. Sun, T. S. Wei, B. Y. Ahn, J. Y. Seo, S. J. Dillon, J. A. Lewis, *Adv. Mater.* **2013**, *25*, 4539.

[22] T. S. Wei, B. Y. Ahn, J. Grotto, J. A. Lewis, *Adv. Mater.* **2018**, *30*, 1703027.

[23] J. Wang, Q. Sun, X. Gao, C. Wang, W. Li, F. B. Holness, M. Zheng, R. Li, A. D. Price, X. Sun, T. K. Sham, X. Sun, *ACS Appl. Mater. Interfaces* **2018**, *10*, 39794.

[24] C. Liu, X. Cheng, B. Li, Z. Chen, S. Mi, C. Lao, *Materials* **2017**, *10*, 934.

[25] J. Huang, J. Yang, W. Li, W. Cai, Z. Jiang, *Thin Solid Films* **2008**, *516*, 3314.

[26] J. G. Tait, E. Witkowska, M. Hirade, T. Ke, P. E. Malinowski, S. Steudel, C. Adachi, P. Heremans, *Org. Electron.* **2015**, *22*, 40.

[27] K. Wang, Y. H. Chang, C. Zhang, B. Wang, *Carbon* **2016**, *98*, 397.

[28] A. Mahajan, C. D. Frisbie, L. F. Francis, *ACS Appl. Mater. Interfaces* **2013**, *5*, 4856.

[29] T. Seifert, E. Sowade, F. Roscher, M. Wiemer, T. Gessner, R. R. Baumann, *Ind. Eng. Chem. Res.* **2015**, *54*, 769.

[30] M. S. Saleh, C. Hu, R. Panat, *Sci. Adv.* **2017**, *3*, e1601986.

[31] C. S. Jones, X. Lu, M. Renn, M. Stroder, W. Shih, *Microelectron. Eng.* **2010**, *87*, 434.

[32] S. H. Kim, K. Hong, K. H. Lee, C. D. Frisbie, *ACS Appl. Mater. Interfaces* **2013**, *5*, 6580.

[33] D. Zhao, T. Liu, J. G. Park, M. Zhang, J. Chen, B. Wang, *Microelectron. Eng.* **2012**, *96*, 71.

[34] E. Jabari, E. Toyserkani, *Carbon* **2015**, *91*, 321.

[35] M. Smith, Y. S. Choi, C. Boughey, S. Kar-Narayan, *Flexible Printed Electron.* **2017**, *2*, 015004.

[36] S. Binder, M. Glatthaar, E. Rädlein, *Aerosol Sci. Technol.* **2014**, *48*, 924.

[37] S. H. Ko, *Semicond. Sci. Technol.* **2016**, *31*, 073003.

[38] T. Seifert, M. Baum, F. Roscher, M. Wiemer, T. Gessner, *Mater. Today: Proceedings* **2015**, *2*, 4262.

[39] G. Chen, Y. Gu, H. Tsang, D. R. Hines, S. Das, *Adv. Eng. Mater.* **2018**, *20*, 1701084.

[40] X. Yu, I. Chen, S. Sarkar, J. Park, H. Pan, Y. Liu, Y. Wang, W. Everhart, *Int. Symp. Microelectron.* **2017**, *2017*, 391.

[41] P. E. Delannoy, B. Riou, T. Brousse, J. Le Bideau, D. Guyomard, B. Lestriez, *J. Power Sources* **2015**, *287*, 261.

[42] H. Kim, R. C. Y. Auyeung, A. Piqué, *J. Power Sources* **2007**, *165*, 413.

[43] K. Choi, D. B. Ahn, S. Lee, *ACS Energy Lett.* **2018**, *3*, 220.

[44] O. A. Mohamed, S. H. Masood, J. L. Bhowmik, *Adv. Manuf.* **2015**, *3*, 42.

[45] G. McHale, S. Aqil, N. J. Shirtcliffe, M. I. Newton, H. Y. Erbil, *Langmuir* **2005**, *21*, 11053.

[46] W. Liu, Z. Chen, G. Zhou, Y. Sun, H. R. Lee, C. Liu, H. Yao, Z. Bao, Y. Cui, *Adv. Mater.* **2016**, *28*, 3578.

[47] W. Liu, J. Chen, Z. Chen, K. Liu, G. Zhou, Y. Sun, M. Song, Z. Bao, Y. Cui, *Adv. Energy Mater.* **2017**, *7*, 1701076.

[48] H. Li, Y. Chen, X. Ma, J. Shi, B. Zhu, L. Zhu, *J. Memb. Sci.* **2011**, *379*, 397.

[49] N. Li, Z. Chen, W. Ren, F. Li, H. Cheng, *Proc. Natl. Acad. Sci.* **2012**, *109*, 17360.

[50] J. Seo, A. K. Singh, Y. Zhang, J. Ma, C. E. Bakis, C. D. Rahn, M. A. Hickner, *J. Appl. Polym. Sci.* **2018**, *135*, 46059.

[51] W. Lai, C. K. Erdonmez, T. F. Marinis, C. K. Bjune, N. J. Dudney, F. Xu, R. Wartena, Y. M. Chiang, *Adv. Mater.* **2010**, *22*, E139.

[52] L. Hu, H. Wu, F. La Mantia, Y. Yang, Y. Cui, *ACS Nano* **2010**, *4*, 5843.

[53] J. Liu, K. Song, P. van Aken, J. Maier, Y. Yu, *Nano Letters* **2014**, *14*, 2597.

[54] S. Xu, Y. Zhang, J. Cho, J. Lee, X. Huang, L. Jia, J. Fan, Y. Su, J. Su, H. Zhang, H. Cheng, B. Lu, C. Yu, C. Chuang, T. Kim, T. Song, K. Shigeta, S. Kang, C. Dagdeviren, I. Petrov, P. Braun, Y. Huang, U. Paik, J. Rogers, *Nat. Commun.* **2013**, *4*, 1543.

[55] M. Cheng, Y. Jiang, W. Yao, Y. Yuan, R. Deivanayagam, T. Foroozan, Z. Huang, B. Song, R. Rojaee, T. Shokuhfar, Y. Pan, J. Lu, R. Shahbazian-Yassar, *Adv. Mater*. **2018**, *30*, 1800615.

[56] D. McOwen, S. Xu, Y. Gong, Y. Wen, G. Godbey, J. Gritton, T. Hamann, J. Dai, G. Hitz, L. Hu, E. Wachsman, *Adv. Mater*. **2018**, *30*, 1707132.

[57] S. Ko, H. Pan, D. Lee, C. Grigoropoulos, H. Park, *Jpn. J. Appl. Phys.* **2010**, *49*, 05EC03.

[58] J. Yeo, S. Hong, D. Lee, N. Hotz, M. Lee, C. Grigoropoulos, S. Ko, *PLoS One* **2012**, *7*, e42315.

[59] V. B. Nam, J. Shin, Y. Yoon, T. T. Giang, J. Kwon, Y. Suh, J. Yeo, S. Hong, S. H. Ko, D. Lee, *Advanced Functional Materials* **2019**, *8*, 1806895.

[60] M. Mizoshiri, S. Arakane, J. Sakurai, S. Hata, *Appl. Phys. Express* **2016**, *9*, 036701.

[61] H. Kim, S. R. Dhage, D. Shim, H. Hahn, *Appl. Phys. A* **2009**, *97*, 791.

IV. SOLVENT-FREE ADDITIVE MANUFACTURING OF ELECTRODES FOR LITHIUM-ION BATTERIES WITH TUNABLE POROSITY

ABSTRACT

Lithium-ion batteries (LIBs) have shown great promises as the energy storage systems for the recently growing electric vehicles (EVs) and plug-in hybrid electric vehicles (PHEVs). The current EV market share is still small with the battery technology considered as the key technical barrier. In this work, we aim to improve the LiNi0.6Co0.2Mn0.2O2 (NMC622) cathodes of LIBs from the perspective of manufacturing method. A solvent-free additive manufacturing method with advantages of (1) lower manufacturing cost, (2) processability of thick electrodes and (3) processability of electrodes with tunable porosity is introduced. The dry-printed electrodes are found to have better high-rate performance compared to the conventional slurry-casted electrodes with capacity retention of 61.7% at the charging rate of 3C. For dry-printed electrodes with varied porosity, both low porosity (26%) electrodes and high porosity (48%) electrodes are delivering lower capacity at the charging rate of 3C compared to those with medium level porosities. The drop in high-rate performance for electrodes with high porosity could be relevant to the drastically decreased electronic conductivity. Granular models are developed to simulate the interfacial-energy-driven dry powder mixing process. The percolating behavior of the conductive additives during the calendaring process is also studied with the granular models, which helps explain the change in electronic conductivity of electrodes with different porosity.

Key words: lithium-ion batteries, additive manufacturing, solvent-free, printed batteries.

1. INTRODUCTION

Lithium-ion batteries (LIBs) are one of the most popular energy storage devices due to their high power and energy densities, rechargeability and long service life.[1–3] They have been widely used in portable electronics such as smartphones and laptops since the invention at 1991.[4] They have also shown great promises as the energy storage systems for the recently growing electric vehicles (EVs) and plug-in hybrid electric vehicles (PHEVs).[4–8] Despite most automotive manufacturers have launched EV production, the EV market share is still small.[7] The battery technology is considered as the key technical barrier for high performance EVs.[5] LIBs have become the most promising energy storage option for EVs with the advantages in long cycle life and high energy density compared to other secondary batteries.[6] Nevertheless, several challenges in optimizing the performance of LIBs need be addressed in order to realize EVs with lower cost, longer driving range, shorter charge time, better safety and longevity. In this work, we are mainly focused on the challenges in manufacturing of electrodes for individual batteries.

The first challenge posted is the manufacturing and material cost. Currently in the industry of LIBs, slurry casting method[9,10] is the major electrode manufacturing method for a wide range of active materials. In this method, the solvent-based slurry is prepared by dispersing active materials, binder additives, and conductive additives in a solvent. Then, the slurry is casted onto the current collector by doctor blade, slot-die coater, or roll-to-roll coating system. The slurry casting method requires large amount usage of solvents. The most commonly used solvent is N-Methyl-2-pyrrolidone (NMP), which is

expensive, flammable, and non-ecofriendly.[11] To reduce environmental hazards, a solvent recovery system is usually required, which significantly increases the manufacturing cost.[12–15] Despite water-based slurry system has been brought up as a more eco-friendly option, it is reported that materials are more difficult to be dispersed due to the strong hydrogen bonding.[16] For both organic solvent-based and water-based slurries, a high temperature drying process is always necessary to ensure the removal of solvents. The drying process further increases the manufacturing cost due to the time and high energy input.[12–15]

The second challenge is to further improve the energy density of LIBs.[17–19] The total amount of energy provided by the battery directly determines the driving range of EVs. Due to the limited space and weight in EVs, LIBs with higher energy density are desired from both performance-wise and cost-wise considerations. Besides developing new active materials with higher capacity,[20,21] intensive research works have been done towards thick electrodes,[22–25] so the ratio of active layers to inactive layers (separator, current collector, etc.) is increased and the energy density of the final packaged full cell would be significantly improved. Nevertheless, the conventional slurry casting method has limited processability in thick electrodes with high areal loading due to the commonly observed delamination (poor bonding) and surface cracking issues in slurry-casted electrodes.[26,27]

The third challenge for LIBs in the EV application is the fast-charging capability.[28–30] With the current level 1 and level 2 charger, the recharge time of a typical EV is on the order of tens of hours.[5] This recharge time is acceptable for overnight charging at home or charging at workplace, but not desired for long-distance

travel which requires multiple times of charging. The U.S. Advanced Battery Consortium (USABC) has set the goal for fast-charging EV batteries by 2023 of 80% charge within 15 minutes.[5] Several issues have been reported and need to be addressed during the fast-charging process of LIBs, including the structural change in cathode materials,[31,32] Li plating in anode[8,28] and degradation of electrolyte[4]. Also, to realize the fast-charging capability, the energy density and battery life usually need to be compromised.[3,5] There have been several reports of fast-charging LIB electrodes with high energy density and long cycle life by introducing structured electrodes.[29,30] However, these methods all require complicated manufacturing methods and are unrealistic for large scale production.

In this work, we aimed to improve the cathodes of LIBs from the perspective of manufacturing method. A solvent-free additive manufacturing (dry printing) method was used for the fabrication of $LiNi_{0.6}Co_{0.2}Mn_{0.2}O_2$ (NMC622) cathodes. In this method, solvents are completely removed so drying and solvent recovery procedures are no longer required. This method significantly reduces the manufacturing cost and shortens the manufacturing timeline for the large-scale production of electrodes. Another advantage of this additive method is the processability of thick electrodes for the purpose of high energy density. The areal loading mass (positive linear relationship to thickness with fixed electrode porosity) can be controlled by the amount of dry powders deposited onto the current collector without introducing bonding-related issues. An interface-enhancing layer as an extra option to improve the bonding between the electrode and current collector is also available in this method.[13] The third benefit from this manufacturing method is the tunable porosity of electrodes in the calendaring process. The effect of

electrode porosity on the electrochemical performance of batteries has been reported in several studies.[33–35] For example, Heubner et al. reported that NMC622 electrodes with increased porosity showed better high-rate performance due to the significantly reduced electrolyte resistance.[34] However, these studies are all based on slurry-casted electrodes and the reported range of porosity is fairly limited. In the solvent-free method, before the calendaring process, the deposited dry powders on the current collector are loosely packed, so the upper limit of electrode porosity is much higher than those by slurry casting method. It is known that electrodes with higher porosity would have better Li-ion diffusivity in the electrolyte, which benefits the high-rate performance. With the solvent-free method, the porosity of electrodes can be made very high. It is necessary to find out whether there are other limiting factors for dry-printed electrodes with high porosity in the fast-charging capability. In this work, dry-printed electrodes with porosity ranging from 26% to 59% were demonstrated. Granular models were developed to help better understand the interfacial-energy-driven mixing behaviors of the dry powders. In electrochemical testing, the dry-printed electrodes exhibited much better high-rate performance compared to the conventional slurry-casted electrodes. The capacity retention at 2C and 3C were 68.5% and 20.3% for slurry-casted electrodes, and 79.4% and 61.7% for dry-printed electrodes. For dry-printed electrodes with varied porosity, it was found that at 3C, both low porosity (26%) electrodes and high porosity (48%) electrodes delivered lower capacity compared to the electrodes with porosities in medium level. The dry-printed electrodes with 33% porosity was found to provide the best performance balancing the energy density and the fast-charging capability. The drop in high-rate performance for electrodes with high porosity could be relevant to the

electronic conductivity of the dry-printed electrodes. Electronic conductivity of the dry-printed electrodes was found to be drastically decreased with increased porosity. The percolating behavior of the conductive additives during the calendaring process was also studied with the granular models, which helped explain the change in electronic conductivity of electrodes with different porosity.

2. EXPERIMENTAL SECTION

Mixing of dry powders for electrodes: NMC622 (BASF), conductive carbon C65 (Timcal Super C65) and polyvinylidene fluoride (PVDF, Kynar HSV900) were used as the active material, conductive additive and binder additive. The three dry powders were mixed in weight ratio of 90/5/5 with zirconia beads in a BeadBug Microtube Homogenizer (Benchmark Scientific).

Solvent-free additive manufacturing of dry electrodes: The mixed powders were loaded into the powder feeder. A carrier gas is used to fluidize the powders for deposition. The substrate (current collector) was mounted on a sample holder. A mask was used for the patterning of the printed powders. The powders deposited on the current collector were heated at 250 °C for 1 hour to melt and activate the binder additives. Then they were pressed into electrodes by a hydraulic press under different pressure for targeted porosity.

Porosity measurement: Porosity of the electrode (ϕ) was determined from the theoretical density of the mixed powders including active materials, binder additives, and conductive additives according to the following equation.

$$\phi = \left\{T - L\left[\left(\frac{W_a}{D_a}\right) + \left(\frac{W_b}{D_b}\right) + \left(\frac{W_c}{D_c}\right)\right]\right\}/T \quad (1)$$

where T is the thickness of electrode, L is the areal loading of the electrode, W is the weight percentage of each material and D is the true density of each material. The subscript a, b and c refer to active materials, binder additives and conductive additives, respectively.

Electronic conductivity measurement: Electronic conductivity was measured with electrodes on polyimide substrate by dry molding method[14]. The dry powders after mixing was directly loaded in a machined mold and uniformly spread. Then the powders were pressed into thick electrode with a hydraulic press and then heated for thermal activation of binder additives. Dielectric polyimide substrate was used to replace the current collector for this measurement. To prepare the contact points from the electrode, copper strips were connected to different locations on the electrode by 2-part silver epoxy. The measurement was carried out with a 4-point method. Current was applied at two neighboring points while voltage was measured at the other two points. Conductivity (σ) is calculated by following equation.

$$\sigma = \frac{2ln2}{\pi T(R_{12,34}+R_{23,14})} \quad (2)$$

where T is the thickness of the electrode, $R_{12,34}$ is obtained by dividing the voltage through points 3 and 4 by the current applied at points 1 and 2, and $R_{23,14}$ is obtained by dividing the voltage through points 1 and 4 by the current applied at points 2 and 3.

Electrochemical testing: The electrodes were assembled in CR2032 coin cell with Celgard separator and liquid electrolyte. Li foil was used as the anode for half-cell testing. Assembly process was conducted in argon-filled glove box with oxygen and

moisture content <0.5 ppm. Before testing starts, a rest time of 36 hours was set for stabilization of the cells. The charging and discharging process was conducted by constant current method.

3. RESULTS AND DISCUSSION

Manufacturing of dry electrodes started from the mixing of dry powders of NMC622 as the active materials, PVDF as the binder additives, and C65 as the conductive additives. The mixed powders were loaded into a powder feeder, and then fluidized by the carrier gas. An electrostatic spraying gun was used to charge the fluidized dry powders. After being charged, the dry powders were drawn to the grounded current collector and got printed. In this work, we aimed to investigate the relationship among the structure of electrodes, physical properties, and electrochemical performance. A small-scale manufacturing setup was used for the fabrication of disc-shape electrodes for coin-cells with a mask placed in front of the current collector for the purpose of patterning. Dry powders collected from the mask was recyclable. After the dry printing process, the electrodes were heated to melt and activate the binder additives. Then, a hydraulic press (only for small-scale electrodes) was used for calendaring the dry-printed electrodes into desired thickness with targeted porosity. The schematic showing the process of the small-scale manufacturing can be found in Figure 1a.

It is worth mentioning that this process is also scalable into large-scale roll-to-roll process, as shown in Figure S1. The dry powders are continuously printed onto the

current collector by the electrostatic sprayer. Subsequent hot rolling results in melting of the binder and formation of a strong bond between particles and current collector.

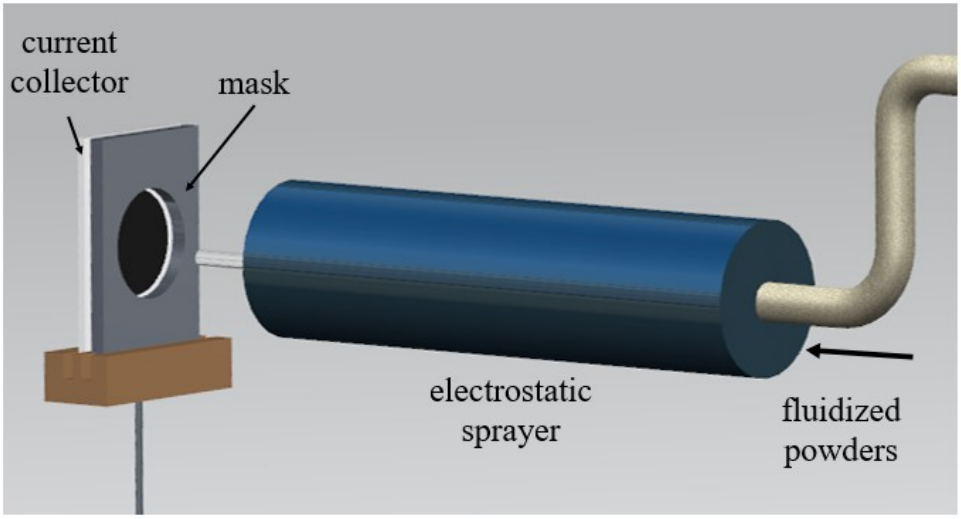

Figure 1. Schematic of the solvent-free additive manufacturing of electrodes for LIBs.

To ensure the functionality of the electrodes, both C65 and PVDF need to be distributed well in the structure of the electrodes. PVDF helps hold the NMC622 and C65 in place and helps attach the electrode to the current collector. A poor bonding of the materials in the electrode might cause extra contact resistance, and a poor bonding between electrode and current collector would result in a high interfacial resistance. The distribution of C65 determines how electrons are transported during the charging and discharging process. In the conventional slurry casting method, a solvent is used to help dissolve the PVDF and dispersive the C65 so they can be distributed well in the final electrodes. Whereas in the solvent-free process, the distribution of PVDF and C65 relied on the interfacial-energy-driven dry powder mixing.[15,36] In Figure 2a, the low-

magnification SEM image presents the overview of the mixed dry powders consisting of NMC622, C65 and PVDF. The SEM images showing the morphology of the three individual particles can be found in Figure S2. The particle sizes of PVDF and C65 are ~150 μm and ~50 μm respectively. Figure 2b presents the zoom-in SEM images on the surface of an NMC622 secondary particle. As seen from the images, after mixing, both PVDF particles and C65 particles got coated on the surface of NMC622.

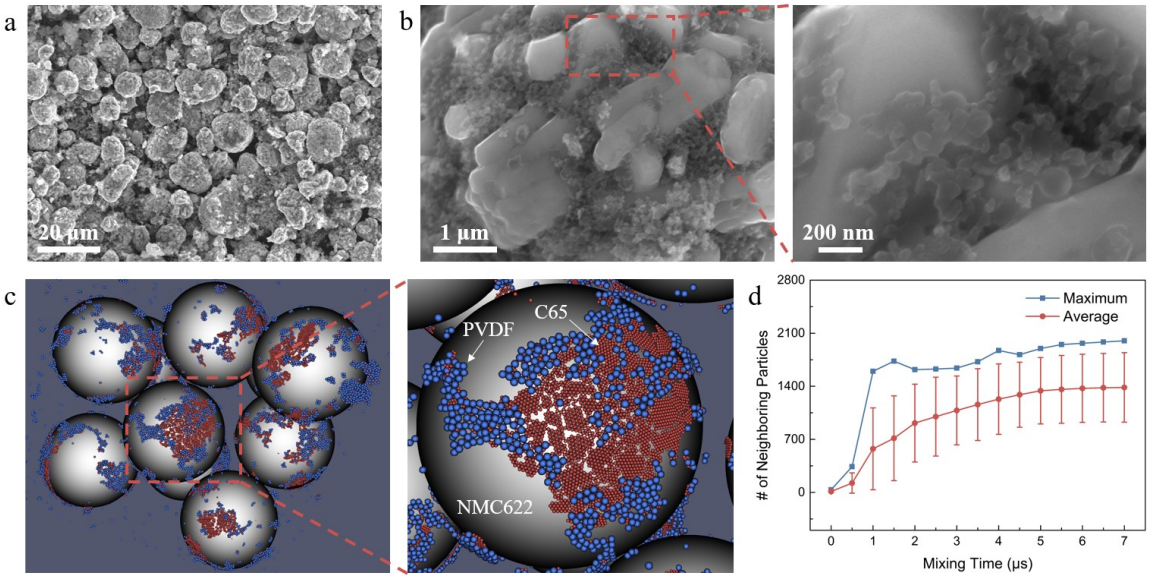

Figure 2. (a) Low-magnification and (b) zoom-in SEM images of the mixed dry powders with PVDF and C65 particles coated on the surface of NMC622 particles. (c) A snapshot from the granular model showing the coating of PVDF and C65 particles on the surface of NMC622 particles at the mixing of 7 μs (particles in grey, blue and red are NMC622, PVDF and C65 respectively). (d) The number of neighboring particles for NMC622 particles in the granular model as a function of the mixing time.

Granular models using granular package on LAMMPS were developed to further understand the interfacial-energy-driven dry powder mixing. In this model, NMC622,

PVDF and C65 particles were described as three types of adhesive spherical particles. Johnson-Kendall-Roberts (JKR) model[37] was used to determine the adhesive forces between two different particles. In this study, only the normal force between two particles was considered and the tangential force was not. The normal force is composed of an elastic term and a damping term.

$$\overrightarrow{F_n} = \overrightarrow{F_{ne}} + \overrightarrow{F_{nd}} \tag{3}$$

JKR model describes the elastic normal force in the following equation.

$$F_{ne} = \left(\frac{4Ea^3}{3R} - 2\pi a^2\sqrt{\frac{4\gamma E}{\pi a}}\right)\vec{n} \tag{4}$$

where E, R and γ are effective particle Young's modulus, effect particle radius and the effective surface energy respectively.

$$\frac{1}{E} = \frac{1-v_i^2}{E_i} + \frac{1-v_j^2}{E_j} \tag{5}$$

$$\frac{1}{R} = \frac{1}{R_i} + \frac{1}{R_j} \tag{6}$$

$$\gamma = \left(\gamma_i^d \gamma_j^d\right)^{0.5} + \left(\gamma_i^p \gamma_j^p\right)^{0.5} \tag{7}$$

where two particles are considered with radii R_i and R_j, Young's moduli E_i and E_j, Poisson's ratio ν_i and ν_j, dispersive surface energy γ_i^d and γ_j^d, and polar surface energy γ_i^p and γ_j^p.

The radius of the contact zone (a) is calculated by solving the equation of the overlap (δ) between particle i and particle j.

$$\delta = \frac{a^2}{R} - 2\sqrt{\frac{\pi a\gamma}{E}} = R_i + R_j - D \tag{8}$$

where D refers to the distance between the center of the two particles.

The damping normal force is calculated based on Tsuji model[37].

$$\overrightarrow{F_{nd}} = -\eta_N \overrightarrow{v_r} \cdot \vec{n} \tag{9}$$

where η_N is the normal dissipation coefficient and $\overrightarrow{v_r}$ is the relative particle velocity. The normal dissipation coefficient is given by the following equation.

$$\eta_N = \alpha (m k_n)^{1/2} \tag{10}$$

where α is a function of the restitution coefficient e (e was chosen to be 1 in this study) and k_n is the normal stiffness coefficient and is estimated by the following equation.

$$\alpha = 1.2728 - 4.2783e + 11.087e^2 - 22.348e^3 + 27.467e^4 - 18.022e^5 + 4.8218e^6 \tag{11}$$

$$k_n = \frac{4Ea}{3} \tag{12}$$

Table 1. Material input parameters for granular model of dry powder mixing.

Material	Diameter (μm)	Density (g/cm^3)	Young's Modulus (GPa)	Poisson's Ratio	Dispersive Surface Energy (mN/m)	Polar Surface Energy (mN/m)
Active Material[36,38]	7	4.9	38	0.18	23.86	16.7
Binder Additive[12,36]	0.15	1.78	4.3	0.34	24.33	6.18
Conductive Additive[12,36]	0.07	2.2	5.0	0.23	50	2

The parameters used in the granular model for each material can be found in Table 1. In the granular model for dry powder mixing, the three types of particles were pre-mixed individually for 3 μs to allow the possible formation of self-agglomerations.

Granular walls were defined to separate the mixing box into three to prevent the interaction of different types of particles. Then, the walls were removed to allow the mixing of the three types of particles. Mixing process was done by introducing wiggles to the boundary of the mixing box. During the dry powder mixing process, the particles of PVDF and C65 gradually got coated on the surface of NMC622 particles, which was consistent to what was observed in the SEM images. Figure 2c displays the snapshot of the granular model after mixing for 7 μs. The number of neighboring particles refers to the numbers of PVDF and C65 particles coated on an individual NMC622 particle. In this model, the number of neighboring particles of each NMC622 particle was counted after certain time steps. The average and maximum number of neighboring particles with the mixing time were summarized and the results are presented in Figure 2d. As seen from the results, the number of neighboring particles increased drastically within the mixing time of 1 μs. The maximum number of neighboring particles at 1 μs was already near to that at 7 μs while the average number was continuously increasing after 1 μs. After mixing for 5 μs, the average number of neighboring particles gradually became stable. However, the variation among different NMC622 particles still existed. This indicated that the nonuniformity in coating condition for each NMC622 particle would happen no matter how long the dry powder mixing took. Also, according to the modeling results (Figure S3a), the partially coated NMC622 particles observed experimentally (Figure S3b) was determined by the ratio of the surface area of each type of particles instead of coming from a poor mixing. In addition, the ratio of inserted particles (calculated from the weight ratio of each materials in dry powder mixing experiment and the physical properties of each type of particles) of (PVDF+C65)/NMC622 was around 1570 in this

granular model while the average number of neighboring particles in the end of the mixing at 7 μs was 1384. The slightly lower number of coated particles was resulting from the formation of some small PVDF/CB agglomerations (Figure S3c). Such agglomerations were also observed experimentally as seen from the SEM image in Figure S3d. Despite this, it was concluded from both experiment and the granular model that most of the additive particles were coated on the surface of NMC622 particles. This was the essential condition to ensure the functionality of the dry-printed NMC622 electrodes.

After dry powder mixing, the powders were additively deposited to the current collectors with the electrostatic sprayer. In the following calendaring process, they were pressed into electrodes with certain thickness for targeted porosity. Figure 3a plots the relationship between the applied pressure during the calendaring process to the final porosity of the dry-printed electrodes. The obtained porosity of the electrodes basically decreased with the increased pressure applied. Electrodes with the highest porosity were obtained by pressing at an extremely low pressure with a lab-scale force meter. Hydraulic press was used for all electrodes except for the ones with highest porosity due to the limited precision in the pressure gauge. Electrodes with lowest porosity were obtained by multi-time pressing with the hydraulic press with heating introduced in between of each press. The cross-section SEM images of the dry-printed electrodes with low (~26%), medium (~43%) and high (~59%) levels of porosity are shown in Figure 3b-d. As seen from the images, for low porosity electrode, the materials were densely packed with almost no visible pores. For electrode with medium porosity, small pores were observed in multiple locations in between of the secondary particles of NMC622 (circled in Figure 3c). Whereas for electrode with high porosity, the materials looked to be very loosely

packed without solid contacts with other particles. Large pores and void spaces were observable all over the structure of the electrode.

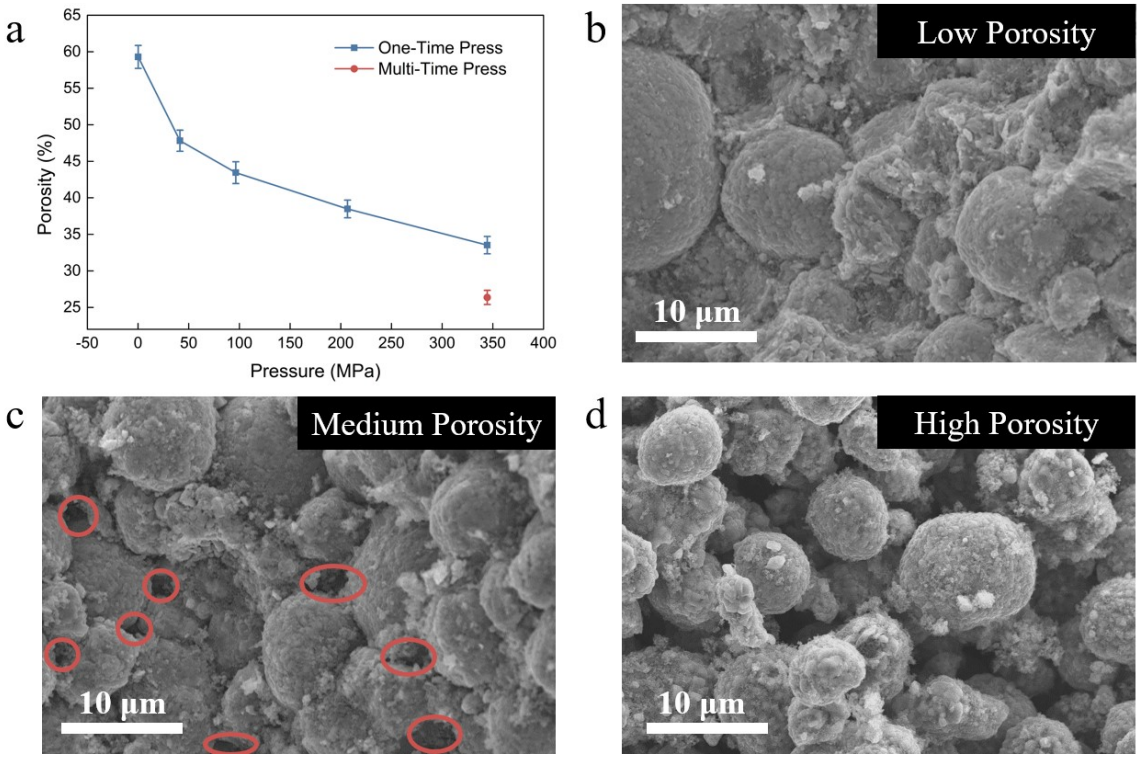

Figure 3. (a) Relationship between the applied pressure during the calendaring process to the final porosity of the dry-printed electrodes. (b) Cross-section SEM images of dry-printed electrodes with low, (c) medium and (d) high levels of porosity.

To investigate the effect of porosity on the electrochemical performance, especially the fast-charging capability of the dry-printed NMC622 electrodes, they were electrochemically tested countering Li foils as half-cells at different charging rate ranging from 0.1C to 3C and fixed discharging rate at 0.5C. Figure 4a shows a typical charging/discharging profile for dry-printed NMC622 electrodes with both charging and

discharging rate at 0.1C under the voltage window of 4.3 V to 2.8 V. In order to compare the rate capability of the dry-printed electrodes to the conventional slurry-casted electrodes, dry-printed electrodes with porosity of 38.3 ± 1.5% and slurry-casted electrodes with porosity of 38.8 ± 2.4% were tested at different charging rate, as seen in Figure 4b.

Table 2. Physical properties of dry-printed electrodes for rate-performance testing.

Porosity Group	NMC622/PVDF/C65 Weight Ratio	Porosity (%)	Thickness (μm)	Areal Loading (mg/cm^2)
26%	90/5/5	26.4 ± 1.0	63.5 ± 2.6	19.27 ± 0.63
33%	90/5/5	33.5 ± 1.2	69.0 ± 1.4	18.9 ± 0.56
38%	90/5/5	38.3 ± 1.5	74.1 ± 1.6	18.8 ± 0.56
43%	90/5/5	43.5 ± 1.5	79.3 ± 1.9	18.5 ± 0.30
48%	90/5/5	47.1 ± 1.4	87.0 ± 4.1	18.9 ± 0.60

The specific capacity of the dry-printed electrodes was slightly higher than those of the slurry-casted electrodes at low C-rate. However, at higher C-rate, the dry-printed electrodes showed significantly higher specific capacity than the slurry-casted electrodes. The capacity retention at 2C and 3C were 68.5% and 20.3% for slurry-casted electrodes, and 79.4% and 61.7% for dry-printed electrodes. The specific capacity of dry-printed electrodes at 3C was more than 2 times higher than that of the slurry-casted electrodes. In the next step, the dry-printed electrodes with different porosity were tested with the same method. The physical properties of the dry-printed electrodes in this porosity study can be found in Table 2. From Figure 4c, the specific capacity of the dry-printed electrodes with low C-rate was not significantly varied with porosity. At 2C, electrodes with 26%

porosity showed slightly worse performance. Whereas at 3C, both low porosity (26%) electrodes and high porosity (48%) electrodes delivered lower specific capacity compared to the electrodes with porosity in medium level (33%, 38% and 43%). The capacity retention at 3C for dry-printed electrodes with porosity of 26%, 33%, 38%, 43% and 48% were 46.8%, 59.4%, 61.7%, 59.5% and 51.3% respectively.

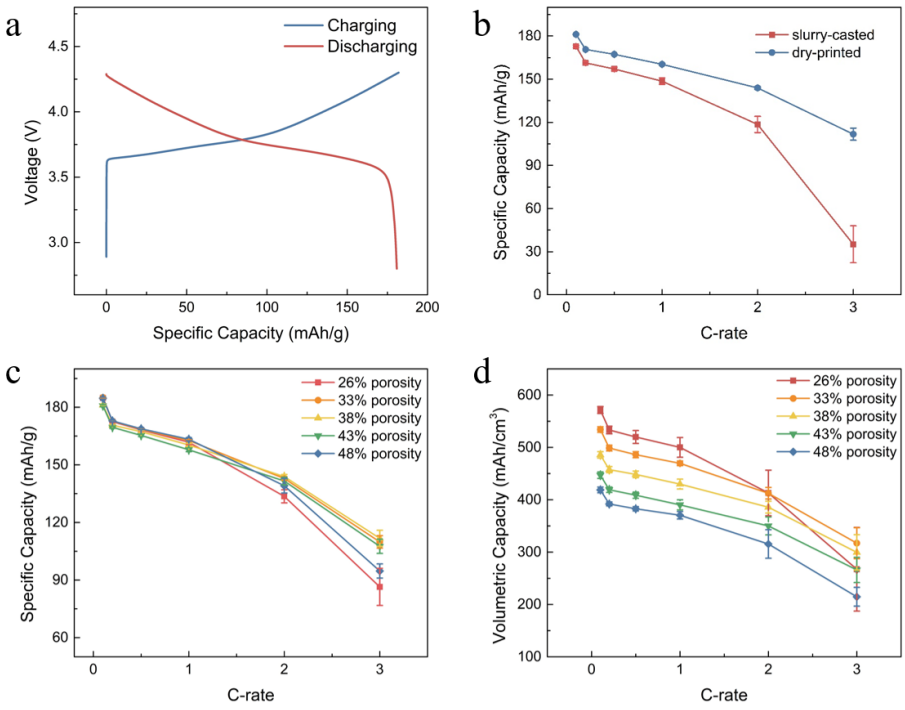

Figure 4. (a) Charging/discharging profile of NMC622 electrodes. (b) Rate performance of dry-printed and slurry-casted electrodes in comparable level of porosity. (c) Rate performance of dry-printed electrodes with varied porosity. (d) Volumetric capacity of the dry-printed electrodes with varied porosity under different C-rate.

When using these electrodes in the battery pack for EVs, the energy density would become an important factor to evaluate the performance. Here, the specific capacity of the dry-printed electrodes was converted into volumetric capacity (only the

thickness of the electrode was considered), as shown in Figure 4d. At low C-rate (<= 1C), the dry-printed electrodes with lower porosity would exhibit higher volumetric capacity, thus had higher energy density because of the smaller thickness of the electrode. However, at 2C, electrodes with 26% porosity showed similar volumetric capacity to those with 33% porosity. The advantage from the lowest porosity (smallest thickness) was cancelled because of the reduced gravimetric capacity at high C-rate. At 3C, the volumetric capacity of the electrodes with 26% porosity was significantly dropped. The results revealed that a trade-off between the energy density and power density did exist in the dry-printed electrodes with varied porosity. The parameter design on the electrode porosity should be deliberately considered based on specific applications. The dry-printed electrodes with 33% porosity was found to provide the best performance balancing the energy density and the fast-charging capability.

From the results of slurry-casted NMC622 electrodes with varied porosity, the electrodes with high porosity (45%) exhibited higher capacity at 1C compared to electrodes with 34% and 36% porosities. Heubner et al. explained that electrodes with increased porosity exhibited higher contact resistance, but lower specific ohmic and charge transfer resistance and increased effective Li-ion diffusivity in the electrolyte. Whereas at high C-rate, Li-ion diffusion in the electrolyte became the limiting factor.[34] Nevertheless, in this study, for dry-printed NMC622 electrodes, when the porosity became even higher (48%), a drop in the high-rate performance was observed. Here an assumption was made that the contact resistance was too high, so it had started to cause insufficient electron transportation thus to limit the performance of electrodes. To verify this assumption, the electronic conductivity of dry-printed electrodes with varied porosity

was measured. Figure 5a shows the schematic of the 4-point method for electronic conductivity measurement and Figure 5b is a photograph of a dry electrode with polyimide as substrate. The conductive points were prepared with copper stripes and silver epoxy. The results of electronic conductivity of dry electrodes with varied porosity is given in Figure 5c. As seen from the results, the electronic conductivity of the electrodes with high porosity was dropped by nearly two orders of magnitude compared to the electrodes with low porosity. The drastic drop in electronic conductivity for electrodes with high porosity could be one of the factors accounting for the decreased capacity at high C-rate.

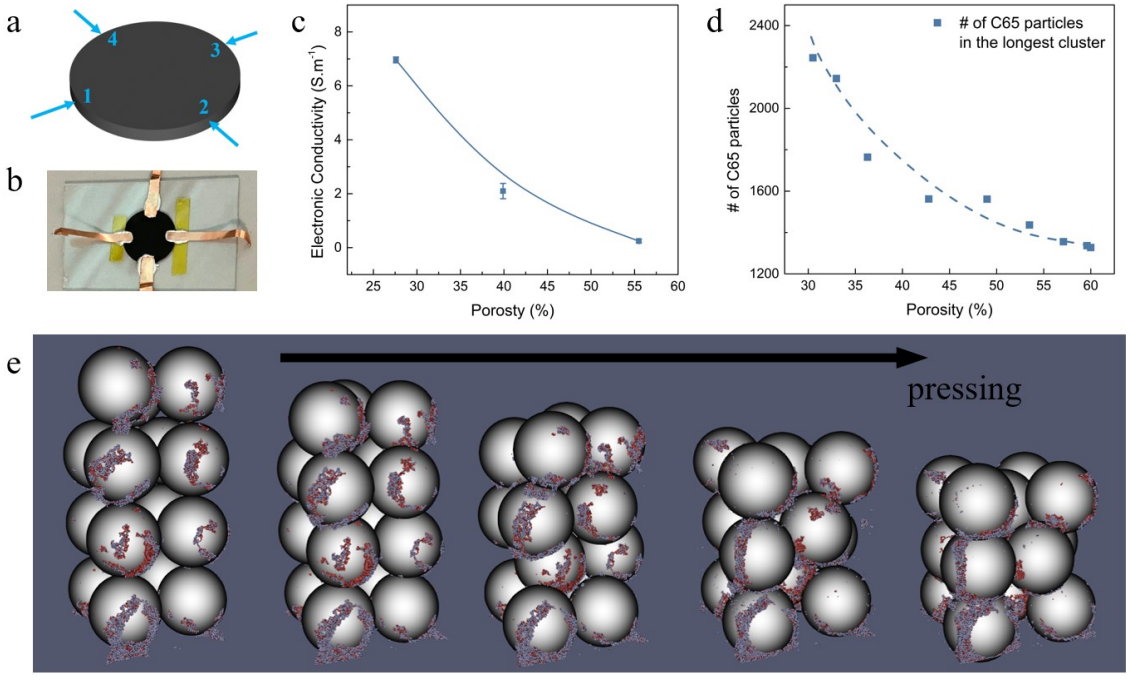

Figure 5. (a) Schematic of the 4-point method for electronic conductivity measurement. (b) Photograph of a dry electrode for electronic conductivity measurement. (c) Electronic conductivity of the dry electrodes with varied porosity. (d) The number of particles in the longest cluster in the granular model as a function of porosity. (e) Snapshots from the granular model showing the pressing process of the mixed particles.

To understand the change in electronic conductivity, the formation of C65 clusters in the granular model during the pressing process was evaluated. The material input parameters used here were the same as those in the model for dry powder mixing. In this model, the mixed dry particles were loaded in a box with high aspect ratio and were pressed by gradually lowering down the granular wall at the topside. The C65 cluster was defined as a set of C65 particles, each of which was within the cutoff distance from one or more other particles in the cluster. The number of particles in the longest cluster was counted after certain time step. It was plotted as a function of porosity as shown in Figure 3d. The porosity value for each time step was calculated by considering the total volume of the particles to the volume of the box. It was found that the number of particles in longest cluster exhibited an exponential growth with decreased porosity. The snapshots from granular model showing the pressing process is presented in Figure 5e. Comparing the particle distribution before and after pressing, most of the C65 particles coated on one NMC622 particle were not contacted with C65 particles coated on another neighboring NMC622 particle at the beginning of the pressing process. During the pressing process, the C65 particles coated on two neighboring NMC622 particles were gradually connected into one cluster. At certain porosity, the C65 particles started to show the percolating behavior (C65 particles on almost all NMC622 merged into one cluster and thus the exponential growth in the number of C65 particles in the longest cluster was observed). The formation of C65 clusters in the granular model explained the huge difference in the measured electronic conductivity values for electrodes with high and low porosities.

4. CONCLUSIONS AND OUTLOOK

In summary, this work demonstrated the solvent-free additive manufacturing of electrodes for LIBs. This method was capable of processing electrodes with a wider range of porosity than the conventional slurry casting method. The distribution of conductive additives and binder additives were verified experimentally and also by granular models. Electrodes with porosity ranging from 26% to 59% were demonstrated with different pressing parameters in the calendaring process. The dry-printed electrodes exhibited much better high-rate performance compared to the conventional slurry-casted electrodes with capacity retention at 61.7% at a charging rate of 3C. For dry-printed electrodes with varied porosity, both low porosity (26%) electrodes and high porosity (48%) electrodes delivered lower specific capacity compared to the electrodes with porosities in medium level at 3C. The dry-printed electrodes with 33% porosity was found to provide the best performance balancing the energy density and the fast-charging capability. Electronic conductivity of the dry-printed electrodes could be relevant to the drastically decreased with increased porosity, which was explained by the formation of C65 clusters in the granular model. It is known that electrodes with higher porosity would have better Li-ion diffusivity in the electrolyte, which benefits the high-rate performance. If the electronic conductivity has become a limiting factor, further improvement could be made to enhance the electronic conductivity of the dry-printed electrode by introducing conductive additives with lower percolation threshold, such as carbon nanotubes. It is possible that the fast-charging capability can be further improved with dry-printed high porosity electrodes without sacrificing the electronic conductivity.

SUPPORTING INFORMATION

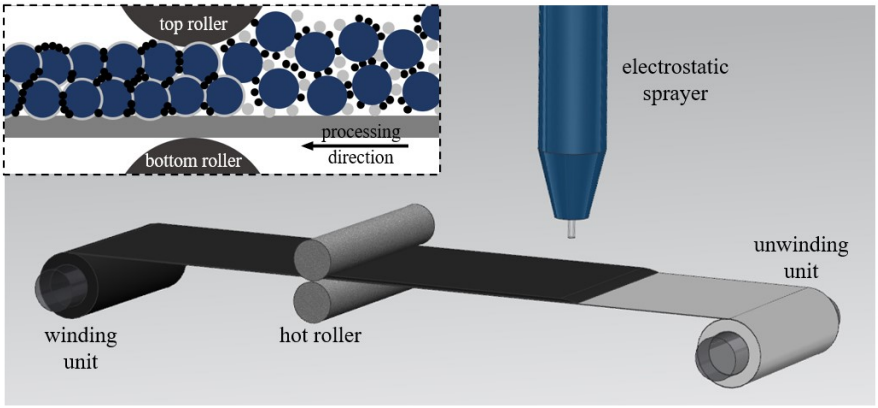

Figure S1. The schematic of large-scale roll-to-roll solvent-free additive manufacturing of electrodes for LIBs.

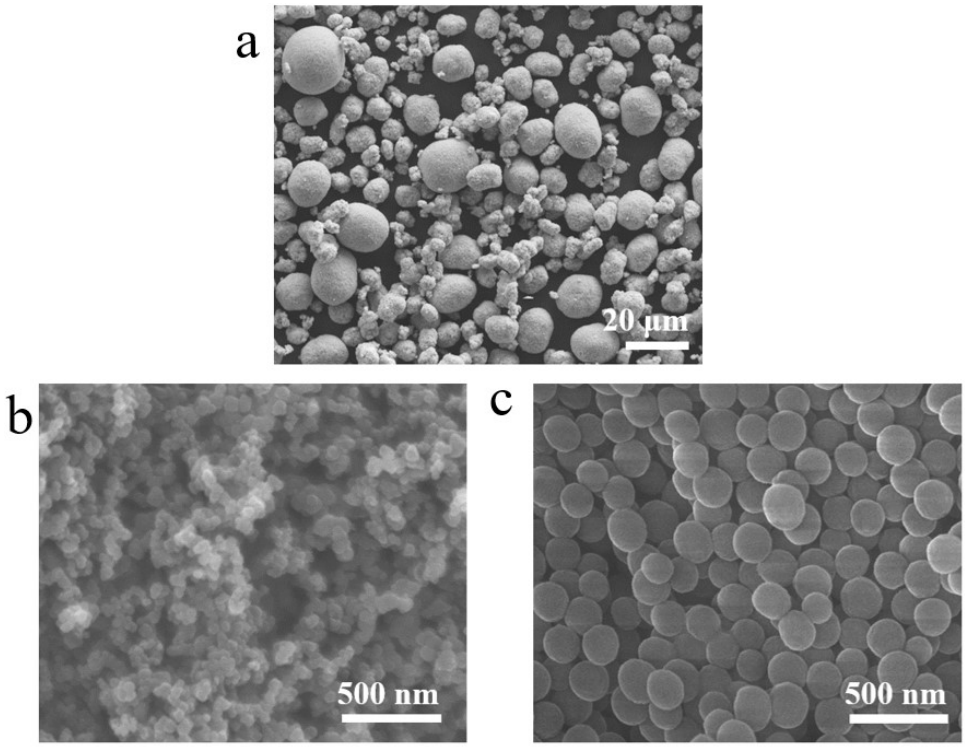

Figure S2. SEM images of dry powders of (a) NMC622, (b) C65 and (c) PVDF.

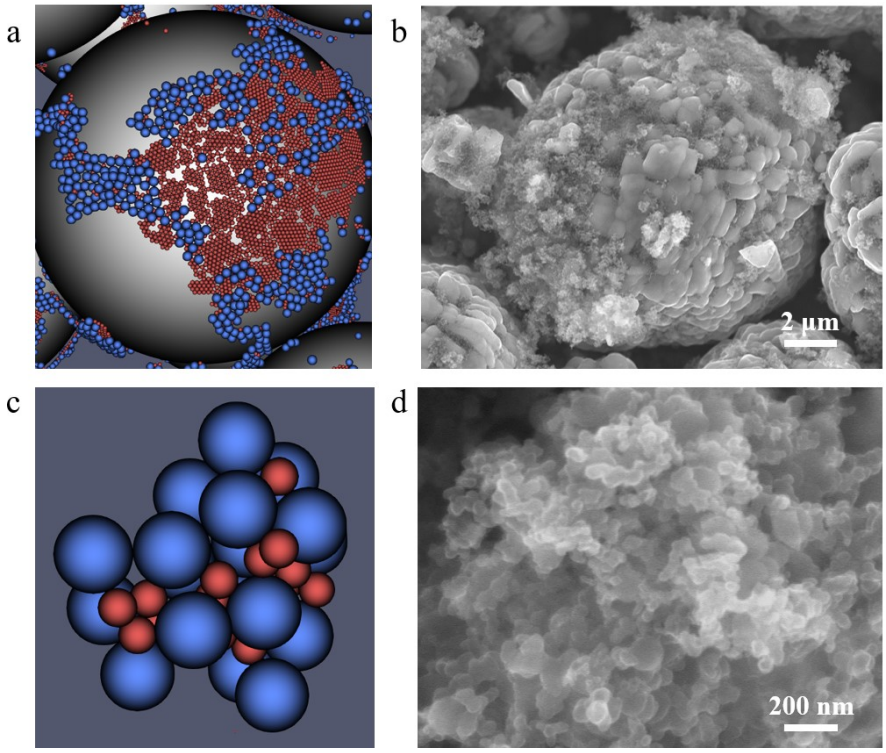

Figure S3. (a) Snapshot from the granular model and (b) SEM image from dry powder mixing experiment of the NMC622 particle partially coated with C65 and PVDF particles. (c) Snapshot from the granular model and (d) SEM image from dry powder mixing experiment of the small agglomeration of C65 and PVDF particles.

REFERENCES

[1] J. M. Tarascon, M. Armand, *Nature* **2001**, *414*, 359.

[2] N. Nitta, F. Wu, J. T. Lee, G. Yushin, *Biochem. Pharmacol.* **2015**, *18*, 252.

[3] J. Liu, Z. Bao, Y. Cui, E. J. Dufek, J. B. Goodenough, P. Khalifah, Q. Li, B. Y. Liaw, P. Liu, A. Manthiram, Y. S. Meng, V. R. Subramanian, M. F. Toney, V. V. Viswanathan, M. S. Whittingham, J. Xiao, W. Xu, J. Yang, X. Q. Yang, J. G. Zhang, *Nat. Energy* **2019**, *4*, 180.

[4] J. Duan, X. Tang, H. Dai, Y. Yang, W. Wu, X. Wei, Y. Huang, *Electrochem. Energy Rev.* **2020**, *3*, 1.

[5] Y. Liu, Y. Zhu, Y. Cui, *Nat. Energy* **2019**, *4*, 540.

[6] K. LIU, K. LI, Q. PENG, C. ZHANG, *Front. Mech. Eng.* **2019**, *14*, 47.

[7] J. Deng, C. Bae, A. Denlinger, T. Miller, *Joule* **2020**, *4*, 1.

[8] N. Takami, K. Ise, Y. Harada, T. Iwasaki, T. Kishi, K. Hoshina, *J. Power Sources* **2018**, *396*, 429.

[9] A. Kraytsberg, Y. Ein-Eli, *Adv. Energy Mater.* **2016**, *6*, 1600655.

[10] V. Wenzel, H. Nirschl, D. Nötzel, *Energy Technol.* **2015**, *3*, 692.

[11] L. Qiu, Z. Shao, M. Yang, W. Wang, F. Wang, J. Wan, J. Wang, Y. Bi, H. Duan, *Cellulose* **2014**, *21*, 615.

[12] B. Ludwig, Z. Zheng, W. Shou, Y. Wang, H. Pan, *Sci. Rep.* **2016**, *6*, 23150.

[13] J. Liu, B. Ludwig, Y. Liu, H. Pan, Y. Wang, *ACS Appl. Mater. Interfaces* **2019**, *11*, 25081.

[14] J. Liu, B. Ludwig, Y. Liu, Z. Zheng, F. Wang, M. Tang, J. Wang, J. Wang, H. Pan, Y. Wang, *Adv. Mater. Technol.* **2017**, *2*, 1700106.

[15] B. Ludwig, J. Liu, I. M. Chen, Y. Liu, W. Shou, Y. Wang, H. Pan, *Adv. Mater. Interfaces* **2017**, *4*, 1700570.

[16] J. Li, B. L. Armstrong, J. Kiggans, C. Daniel, D. L. Wood, *Langmuir* **2012**, *28*, 3783.

[17] W. Lai, C. K. Erdonmez, T. F. Marinis, C. K. Bjune, N. J. Dudney, F. Xu, R. Wartena, Y. M. Chiang, *Adv. Mater.* **2010**, *22*, 139.

[18] J. Wang, Q. Sun, X. Gao, C. Wang, W. Li, F. B. Holness, M. Zheng, R. Li, A. D. Price, X. Sun, T. K. Sham, X. Sun, *ACS Appl. Mater. Interfaces* **2018**, *10*, 39794.

[19] Q. Cheng, Z. Song, T. Ma, B. B. Smith, R. Tang, H. Yu, H. Jiang, C. K. Chan, *Nano Lett.* **2013**, *13*, 4969.

[20] I. H. Son, J. H. Park, S. Kwon, S. Park, M. H. Rümmeli, A. Bachmatiuk, H. J. Song, J. Ku, J. W. Choi, J. M. Choi, S. G. Doo, H. Chang, *Nat. Commun.* **2015**, *6*, 7393.

[21] X. Shen, H. Liu, X. B. Cheng, C. Yan, J. Q. Huang, *Energy Storage Mater.* **2018**, *12*, 161.

[22] H. Kim, R. C. Y. Auyeung, A. Piqué, *J. Power Sources* **2007**, *165*, 413.

[23] J. S. Wang, P. Liu, E. Sherman, M. Verbrugge, H. Tataria, *J. Power Sources* **2011**, *196*, 8714.

[24] T. S. Wei, B. Y. Ahn, J. Grotto, J. A. Lewis, *Adv. Mater.* **2018**, *30*, 1703027.

[25] R. Elango, A. Demortière, V. De Andrade, M. Morcrette, V. Seznec, *Adv. Energy Mater.* **2018**, *8*, 173031.

[26] K. C. Klavetter, J. L. Snider, J. P. De Souza, H. Tu, T. H. Cell, J. H. Cho, C. J. Ellison, A. Heller, C. B. Mullins, *J. Mater. Chem. A* **2014**, *2*, 14459.

[27] Z. Du, K. M. Rollag, J. Li, S. J. An, M. Wood, Y. Sheng, P. P. Mukherjee, C. Daniel, D. L. Wood, *J. Power Sources* **2017**, *354*, 200.

[28] T. R. Tanim, J. E. Soc, T. R. Tanim, E. J. Dufek, M. Evans, C. Dickerson, A. N. Jansen, B. J. Polzin, A. R. Dunlop, S. E. Trask, R. Jackman, I. Bloom, Z. Yang, E. Lee, *J. Electrochem. Soc.* **2019**, *166*, A1926.

[29] K. Chen, M. Ji, V. Goel, C. Yang, S. Kazemiabnavi, S. M. Mortuza, E. Kazyak, J. Mazumder, K. Thornton, J. Sakamoto, P. Dasgupta, *J. Power Sources* **2020**, *471*, 228475.

[30] J. Daigle, Y. Asakawa, M. Beaupré, V. Gariépy, R. Vieillette, D. Laul, M. Trudeau, K. Zaghib, *Sci. Rep.* **2019**, *9*, 16871.

[31] E. Hu, X. Wang, X. Yu, X. Q. Yang, *Acc. Chem. Res.* **2018**, *51*, 290.

[32] T. Li, X.-Z. Yuan, L. Zhang, D. Song, K. Shi, C. Bock, *Electrochem. Energy Rev.* **2020**, *3*, 43.

[33] M. Singh, J. Kaiser, H. Hahn, *Batteries* **2016**, *2*, 35.

[34] C. Heubner, A. Nickol, J. Seeba, S. Reuber, N. Junker, M. Wolter, M. Schneider, A. Michaelis, *J. Power Sources* **2019**, *419*, 119.

[35] N. Ogihara, Y. Itou, T. Sasaki, Y. Takeuchi, *J. Phys. Chem. C* **2015**, *119*, 4612.

[36] B. Ludwig, J. Liu, Y. Liu, Z. Zheng, Y. Wang, H. Pan, *J. Micro Nano-Manufacturing* **2017**, *5*, 40902.

[37] J. K. Langstreth, K. Kevin, R. A. D., *Proc. R. Soc. Lond. A* **1971**, *324*, 301.

[38] A. Davoodabadi, J. Li, Y. Liang, R. Wang, H. Zhou, D. L. Wood, T. J. Singler, C. Jin, *J. Electrochem. Soc.* **2018**, *165*, A2493.

SECTION

2. CONCLUSION

In conclusion, two AM methods, one solvent-based (wet) and one solvent-free (dry) are developed for the fabrication of LIB electrodes for the purpose of extending the applications, improving the performance and lowering the manufacturing cost of LIBs.

In the first two papers, aerosol printing of materials including current collectors and active materials of the electrodes for LIBs are demonstrated. The printed and annealed Au and Cu are of high conductivity and are qualified for the current collectors of LIBs. Two commonly used pairs of active materials for cathode and anode are aerosol printed, including LMO/graphite and LFP/LTO. Aerosol printing of composite inks containing active materials, conductive additives and binder additives are successfully carried out with uniform distribution of active materials and additives. The galvanostatic cyclic testing results show that the four active materials by AJP all exhibit satisfactory capacity and cyclic performance.

In the third paper, aerosol printing is utilized for the fabrication of customizable LIBs with arbitrary geometry on 3D structures due to its unique advantage of non-planar printing capability. LFP cathodes and LTO anodes are aerosol printed and assembled into LIBs. By the printing method, electrodes with arbitrary geometry, tailorable thickness and on non-planar substrates can be realized. The highest areal capacity achieved by aerosol printed electrodes is ~7.1 mAh/cm2, which is at least twice of those conventional electrodes. Customizable LIBs on targeted objects with arbitrary geometry is further

realized with the as-fabricated 3D non-planar electrodes combining 3D packaging technique by fused deposition modeling.

In the fourth paper, a solvent-free additive manufacturing method with advantages of lower manufacturing cost, processability of thick electrodes and processability of electrodes with tunable porosity is introduced. The dry-printed electrodes are found to have better high-rate performance compared to the conventional slurry-casted electrodes with capacity retention of 61.7% at the charging rate of 3C. For dry-printed electrodes with varied porosity, both low porosity (26%) electrodes and high porosity (48%) electrodes are delivering lower capacity at the charging rate of 3C compared to those with medium level porosities. The drop in high-rate performance for electrodes with high porosity could be relevant to the drastically decreased electronic conductivity. Granular models are developed to simulate the interfacial-energy-driven dry powder mixing process. The percolating behavior of the conductive additives during the calendaring process is also studied with the granular models.

BIBLIOGRAPHY

[1] B. Diouf, R. Pode, *Renew. Energy* **2015**, *76*, 375.

[2] D. Larcher, J. Tarascon, *Nat. Chem.* **2014**, *7*, 19.

[3] L. J. Deiner, T. L. Reitz, *Adv. Eng. Mater.* **2017**, *19*, 1600878.

[4] Y. Hu, X. Sun, *J. Mater. Chem. A* **2014**, *2*, 10712.

[5] N. Nitta, F. Wu, J. Lee, G. Yushin, *Mater. Today* **2015**, *18*, 252.

[6] B. Ludwig, Z. Zheng, W. Shou, Y. Wang, H. Pan, *Sci. Rep.* **2016**, *6*, 23150.

[7] Y. Wang, C. Chen, H. Xie, T. Gao, Y. Yao, G. Pastel, X. Han, Y. Li, J. Zhao, K. K. Fu, L. Hu, *Adv. Funct. Mater.* **2017**, *27*, 1703140.

[8] L. H. Saw, Y. Ye, A. A. Tay, *J. Cleaner Prod.* **2016**, 113, 1032.

[9] V. Wenzel, H. Nirschl, D. Nötzel, *Energy Technol.* **2015**, *3*, 692.

[10] A. Kraytsberg, Y. Ein-Eli, *Adv. Energy Mater.* **2016**, 6, 1600655.

[11] L. Qiu, Z. Shao, M. Yang, W. Wang, F. Wang, J. Wan, J. Wang, Y. Bi, H. Duan, *Cellulose* **2013**, *21*, 615.

[12] R. Elango, A. Demortière, V. D. Andrade, M. Morcrette, V. Seznec, *Adv. Energy Mater.* **2018**, *8*, 1703031.

[13] T.-S. Wei, B. Y. Ahn, J. Grotto, J. A. Lewis, *Adv. Mater.* **2018**, *30*, 1703027.

[14] H. Kim, R. C. Auyeung, A. Piqué, *J. Power Sources* **2007**, *165*, 413.

[15] J. Liu, Z. Bao, Y. Cui, E. J. Dufek, J. B. Goodenough, P. Khalifah, Q. Li, B. Y. Liaw, P. Liu, A. Manthiram, Y. S. Meng, V. R. Subramanian, M. F. Toney, V. V. Viswanathan, M. S. Whittingham, J. Xiao, W. Xu, J. Yang, X.-Q. Yang, J.-G. Zhang, *Nat. Energy* **2019**, 4, 180.

[16] L.H. Saw, Y. Ye, A. A. O. Tay, *J. Cleaner Prod.* **2016**, *113*, 1032.

[17] J. Kim, R. Kumar, A. J. Bandodkar, J. Wang, *Adv. Electron. Mater.* **2017**, *3*, 1600260.

[18] L. J. Deiner, T. Jenkins, A. Powell, T. Howell, M. Rottmayer, *Adv. Eng. Mater.* **2019**, 21, 1801281.

[19] F. Zhang, M. Wei, V. V. Viswanathan, B. Swart, Y. Shao, G. Wu, C. Zhou, *Nano Energy* **2017**, 40, 418.

[20] S. Zheng, Z. Wu, F. Zhou, X. Wang, J. Ma, C. Liu, Y. He, X. Bao, *Nano Energy* **2018**, 51, 613.

[21] M. Wei, F. Zhang, W. Wang, P. Alexandridis, C. Zhou, G. Wu, *J. Power Sources* **2017**, 354, 134.

[22] C. L. Cobb, C. C. Ho, *Electrochem. Soc. Interface* **2016**, 25, 75.

[23] S. Ferrari, M. Loveridge, S. D. Beattie, M. Jahn, R. J. Dashwood, R. Bhagat, *J. Power Sources* **2015**, 286, 25.

[24] P. Chang, H. Mei, S. Zhou, K. G. Dassios, L. Cheng, *J. Mater. Chem. A* **2019**, 7, 4230.

[25] S. H. Ko, *Semicond. Sci. Technol.* **2016**, 31, 073003.

[26] J. G. Tait, E. Witkowska, M. Hirade, T. Ke, P. E. Malinowski, S. Steudel, C. Adachi, P. Heremans, *Org. Electron.* **2015**, 22, 40.

[27] K. Wang, Y. H. Chang, C. Zhang, B. Wang, *Carbon* **2016**, 98, 397.

[28] A. Mahajan, C. D. Frisbie, L. F. Francis, *ACS Appl. Mater. Interfaces* **2013**, 5, 4856.

[29] T. Seifert, E. Sowade, F. Roscher, M. Wiemer, T. Gessner, R. R. Baumann, *Ind. Eng. Chem. Res.* **2015**, 54, 769.

[30] M. S. Saleh, C. Hu, R. Panat, *Sci. Adv.* **2017**, 3, e1601986.

[31] C. S. Jones, X. Lu, M. Renn, M. Stroder, W. Shih, *Microelectron. Eng.* **2010**, 87, 434.

[32] S. H. Kim, K. Hong, K. H. Lee, C. D. Frisbie, *ACS Appl. Mater. Interfaces* **2013**, 5,

[33] D. Zhao, T. Liu, J. G. Park, M. Zhang, J. Chen, B. Wang, *Microelectron. Eng.* **2012**, 96, 71.

[34] E. Jabari, E. Toyserkani, *Carbon* **2015**, 91, 321.

[35] M. Smith, Y. S. Choi, C. Boughey, S. Kar-Narayan, *Flexible Printed Electron.* **2017**, 2, 015004.

[36] S. Binder, M. Glatthaar, E. Rädlein, *Aerosol Sci. Technol.* **2014**, 48, 924.

[37] T. Seifert, M. Baum, F. Roscher, M. Wiemer, T. Gessner, *Mater. Today: Proceedings* **2015**, 2, 4262.

[38] G. Chen, Y. Gu, H. Tsang, D. R. Hines, S. Das, *Adv. Eng. Mater.* **2018**, 20, 1701084.

[39] M. Cheng, Y. Jiang, W. Yao, Y. Yuan, R. Deivanayagam, T. Foroozan, Z. Huang, B. Song, R. Rojaee, T. Shokuhfar, Y. Pan, J. Lu, R. Shahbazian-Yassar, *Adv. Mater*. **2018**, *30*, 1800615.

[40] D. McOwen, S. Xu, Y. Gong, Y. Wen, G. Godbey, J. Gritton, T. Hamann, J. Dai, G. Hitz, L. Hu, E. Wachsman, *Adv. Mater.* **2018**, *30*, 1707132.

[41] B. Ludwig, J. Liu, I.-M. Chen, Y. Liu, W. Shou, Y. Wang, H. Pan, *Adv. Mater. Interfaces* **2017**, *4*, 1700570.

[42] J. Liu, B. Ludwig, Y. Liu, H. Pan, Y. Wang, *ACS Appl. Mater. Interfaces* **2019**, *11*, 25081.

[42] J. Liu, B. Ludwig, Y. Liu, Z. Zheng, F. Wang, M. Tang, J. Wang, J. Wang, H. Pan, Y. Wang, *Adv. Mater. Technol.* **2017**, *2*, 1700106.

[43] I. Doberdo, N. Loffler, N. Laszczynski, D. Cericola, N. Penazzi, S. Bodoardo, G.-T. Kim, S. Passerini, *J. Power Sources* **2014**, 248, 1000.

[44] B. Bitsch, J. Dittmann, M. Schmitt, P. Scharfer, W. Schabel, N. Willenbacher, *J. Power Sources* **2014**, 265, 81.

[45] J. Li, B. L. Armstrong, J. Kiggans, C. Daniel, D. L. Wood, *Langmuir* **2012**, 28, 3783.

VITA

Xiaowei Yu was born in Ningbo City, Zhejiang Provice, China. She received her bachelor's degree in Polymer Materials and Engineering from Donghua University and her minor bachelor's degree in Applied Psychology from East China Normal University in 2015. Xiaowei started her Ph.D. in Mechanical Engineering at Missouri S&T in Fall 2015 in Dr. Xian Huang's group, where she worked on stretchable electronics and transient electronics. She joined Dr. Heng Pan's group in Spring 2016, where she continued her previous works and started her research on additive manufacturing of Li-ion batteries. Xiaowei received her Ph.D. in Mechanical Engineering from the Missouri University of Science and Technology in December 2020. She authored and co-authored seven journal papers and two conference papers during her Ph.D. study.